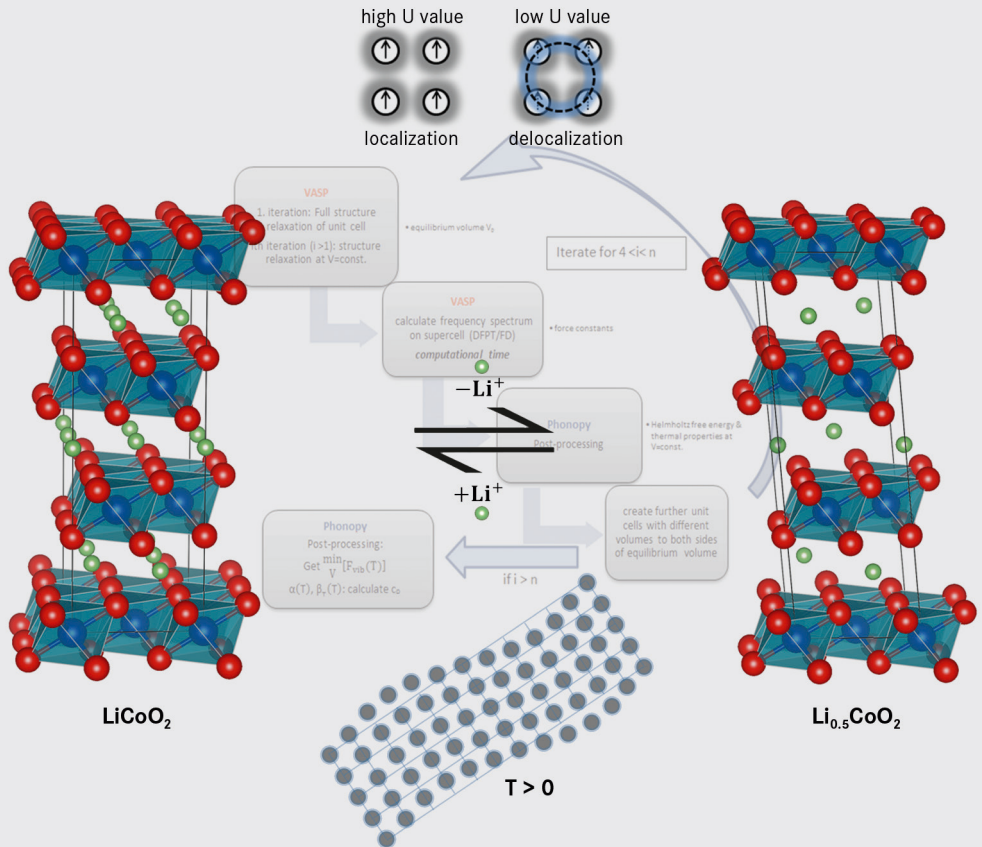


# Modelling Thermodynamic Properties of Intercalation Compounds for Lithium Ion Batteries

Siaufung Oliver Dang







Forschungszentrum Jülich GmbH  
Institute of Energy and Climate Research (IEK)  
Microstructure and Properties of Materials (IEK-2)

# Modelling Thermodynamic Properties of Intercalation Compounds for Lithium Ion Batteries

Siaufung Oliver Dang

Schriften des Forschungszentrums Jülich  
Reihe Energie & Umwelt / Energy & Environment

Band / Volume 319

---

ISSN 1866-1793

ISBN 978-3-95806-141-5

Bibliographic information published by the Deutsche Nationalbibliothek.  
The Deutsche Nationalbibliothek lists this publication in the Deutsche  
Nationalbibliografie; detailed bibliographic data are available in the  
Internet at <http://dnb.d-nb.de>.

Publisher and  
Distributor: Forschungszentrum Jülich GmbH  
Zentralbibliothek  
52425 Jülich  
Tel: +49 2461 61-5368  
Fax: +49 2461 61-6103  
Email: [zb-publikation@fz-juelich.de](mailto:zb-publikation@fz-juelich.de)  
[www.fz-juelich.de/zb](http://www.fz-juelich.de/zb)

Cover Design: Grafische Medien, Forschungszentrum Jülich GmbH

Printer: Grafische Medien, Forschungszentrum Jülich GmbH

Copyright: Forschungszentrum Jülich 2015

Schriften des Forschungszentrums Jülich  
Reihe Energie & Umwelt / Energy & Environment, Band / Volume 319

D 82 (Diss. RWTH Aachen University, 2015)

ISSN 1866-1793  
ISBN 978-3-95806-141-5

The complete volume is freely available on the Internet on the Jülicher Open Access Server (JuSER)  
at [www.fz-juelich.de/zb/openaccess](http://www.fz-juelich.de/zb/openaccess).



This is an Open Access publication distributed under the terms of the [Creative Commons Attribution License 4.0](https://creativecommons.org/licenses/by/4.0/),  
which permits unrestricted use, distribution, and reproduction in any medium, provided the original work is properly cited.

# List of Abbreviations

- ATAT** alloy theoretic automated toolkit. ix, 90, 95, 119, 127, 129, 133
- BZ** Brillouin zone. 51
- CALPHAD** calculation of phase diagrams. 84, 95
- CASTEP** Cambridge serial total energy package. 40
- CFD** computational fluid dynamics. 84, 89, 95
- DEC** diethyl carbonate. 7
- DFT** density functional theory. 1, 19, 21, 28, 39, 40, 42, 43, 46, 48, 51, 52, 67, 75, 76, 95, 127, 128
- DMC** dimethyl carbonate. 7
- DOS** density of states. 15, 17, 67, 70, 75, 78, 80, 81, 82, 95, 115, 117, 118, 123, 125, 126
- EC** ethylene carbonate. 7
- EMC** ethyl methyl carbonate. 7
- EOS** equation of state. 26, 27, 28, 81, 82, 118, 119, 131
- GGA** general gradient approximation. 44, 45, 46, 63, 65, 76, 78, 80, 82, 117

- GIC** graphite intercalation compound. 9
- HOMO** highest occupied molecular orbital. 21
- LDA** local density approximation. 44, 45, 46
- LIB** lithium-ion battery. 1, 5, 6, 7, 9, 10, 18, 19, 21, 84, 90, 95, 115, 116
- LUMO** lowest unoccupied molecular orbital. 21
- MIT** metal-to-insulator transition. 15, 17
- PAW** projector-augmented wave. 48, 123
- PC** propylene carbonate. 7
- QHA** quasi-harmonic approximation. 56, 57, 76, 89, 119, 123, 130
- SCF** self-consistent field. 40, 42
- SEI** solid electrolyte interface. 7, 18, 115
- VASP** Vienna ab-initio simulation package. 40, 48, 95, 121, 127
- XRD** x-ray diffraction. 12, 15

# Abstract

DFT calculations were employed to model thermodynamic properties on intercalation compounds for lithium ion batteries. Two compounds were investigated: the commercially available  $\text{Li}_x\text{CoO}_2$  and the silicon based  $\text{Li}_x\text{Mg}_2\text{Si}$ . The  $\text{LiCoO}_2$  compound was modelled under two aspects. Firstly, total energy calculations were carried out on the two-phase region between the delithiated, metallic phase and the lithiated, semiconducting phase in the attempt to model the two-phase equilibrium. It was possible to observe that the metallic state is energetically more stable at low lithium contents agreeing with experimental evidence. It was, however, not possible to map the two-phase region properly, most likely due to deficiencies in the applied approach using a single Hubbard U parameter on the cobalt d-orbitals. The computed average intercalation voltage was derived for a series of compositional segments between  $\text{LiCoO}_2$  and  $\text{Li}_{0.5}\text{CoO}_2$  and demonstrate a good agreement to prior DFT calculations. Secondly, isobaric heat capacities were calculated within the quasi-harmonic approximation for three stoichiometries of  $\text{Li}_x\text{CoO}_2$  ranging from  $\text{LiCoO}_2$  to  $\text{Li}_{0.5}\text{CoO}_2$ . The results indicate a good agreement with available experimental data when accounting for the phase impurities of the sample. Calculations on a boron doped compound  $\text{LiCo}_{11/12}\text{B}_{1/12}\text{O}_2$  were also done and yielded results which fall into the expected range.

In case of  $\text{Li}_x\text{Mg}_2\text{Si}$  a more elaborate approach was employed to explore the configurational space of the solid solution in terms of the vacancy arrangements by using the cluster expansion method (employed software: ATAT).

Prior investigations by other researchers had led to the estimation of the solubility limit to be around  $x=0.91$ . In this respect, the computed results indicate a continuously increasing destabilization of the host lattice, which begins to distort significantly when the lithium content exceeds  $x=0.5$ . To derive the solubility limit from the DFT calculations two other phases ( $\text{Mg}_x\text{Li}_{1-x}$  and  $\text{Li}_2\text{MgSi}$ ) would still need to be calculated as well since they form a three phase field with  $\text{Li}_x\text{Mg}_2\text{Si}$ . The derivation of the average intercalation voltage yielded on average a shift of 0.5 V lower compared to the experimental profile.

# Zusammenfassung

DFT Rechnungen wurden zur Modellierung thermodynamischer Eigenschaften von Interkalationsverbindungen für Lithium-Ionen Batterien eingesetzt. Dazu wurden zwei Verbindungen untersucht: das kommerziell erhältliche  $\text{Li}_x\text{CoO}_2$  und das siliziumbasierte  $\text{Li}_x\text{Mg}_2\text{Si}$ . Das  $\text{Li}_x\text{CoO}_2$  wurde unter zwei Aspekten modelliert. Auf der einen Seite wurden Berechnungen zur Energie im Bereich des zwei-Phasen Gebietes zwischen der delithiierten, metallischen Phase und der lithiierten, halbleitenden Phase durchgeführt. Anhand der Modell-Ergebnisse konnte beobachtet werden, dass die metallische Phase in Übereinstimmung mit experimentellen Bestimmungen bei niedrigen Lithium-Gehalten energetisch stabiler ist. Allerdings war es nicht möglich das zwei-Phasen Gebiet adequat abzubilden, was wahrscheinlich auf Unzulänglichkeiten des verwendeten Ansatzes mit nur einem Hubbard U Parameter auf den Kobalt d-Orbitalen zurückzuführen ist. Über die Energien wurden die mittleren Interkalationsspannungen für eine Reihe von Segmenten zwischen  $\text{LiCoO}_2$  und  $\text{Li}_{0.5}\text{CoO}_2$  abgeleitet, welche eine gute Übereinstimmung mit vorhergegangenen DFT Rechnungen aufweisen. Auf der anderen Seite wurden isobare Wärmekapazitäten im Temperaturintervall 0 bis 600 K mittels der quasiharmonischen Näherung für drei Stöchiometrien der  $\text{Li}_x\text{CoO}_2$ -Verbindung berechnet. Die Ergebnisse zeigen eine gute Übereinstimmung mit vorhandenen experimentellen Daten unter Berücksichtigung von Phasenunreinheiten der Proben. Die Berechnungen wurden auch auf die Bor-dotierte Verbindung  $\text{LiCo}_{11/12}\text{B}_{1/12}\text{O}_2$  ausgeweitet, dessen Ergebnisse im erwarteten

Bereich liegen.

Im Fall von  $\text{Li}_x\text{Mg}_2\text{Si}$  wurde ein umfangreicherer Ansatz eingesetzt, um den Konfigurationsraum der Mischkristallverbindung bezüglich der Leerstellen-Anordnungen abzudecken. Dies erfolgte mittels der Cluster Expansion Methode (verwendete Software: ATAT). Vorangegangene Untersuchungen hatten zu einer Schätzung der Löslichkeitsgrenze auf etwa  $x=0,91$  geführt. In dieser Hinsicht deuten die Ergebnisse der Rechnung auf eine kontinuierlich zunehmende Destabilisierung des Wirtsgitters hin, welches bei einem Überschreiten des Lithiumgehaltes von  $x=0,5$  anfängt sich signifikant zu verzerrern. Um die Löslichkeitsgrenze abzuleiten müssten zwei andere Phasen ( $\text{Mg}_x\text{Li}_{1-x}$  and  $\text{Li}_2\text{MgSi}$ ) ebenfalls noch modelliert werden, da diese zusammen mit  $\text{Li}_x\text{Mg}_2\text{Si}$  im Phasengleichgewicht stehen. Die Ableitung der mittleren Interkalationsspannung weist eine durchschnittliche Abweichung von 0,5 V nach unten im Vergleich zum experimentellen Spannungsprofil auf.

# Contents

<b>Abstract</b>	<b>iii</b>
<b>Zusammenfassung</b>	<b>v</b>
<b>1 Introduction</b>	<b>1</b>
1.1 The framework of this thesis . . . . .	1
1.2 Concept of electrochemical energy storage . . . . .	4
1.3 Lithium Ion batteries . . . . .	6
1.4 The solid electrolyte interface . . . . .	8
1.5 The Graphite anode . . . . .	10
1.6 Layered oxides as intercalation cathode materials . . . . .	10
1.7 Properties of $\text{LiCoO}_2$ . . . . .	12
1.7.1 Structural stability . . . . .	12
1.7.2 The metal-to-insulator transition of $\text{LiCoO}_2$ . . . . .	17
1.7.3 Behaviour at elevated temperatures . . . . .	18
1.8 Mg-Si-alloys as alloying anode material . . . . .	19
1.9 The voltage window . . . . .	22
<b>2 Theory</b>	<b>25</b>
2.1 Thermodynamic potentials . . . . .	25
2.2 Equation of states . . . . .	27
2.3 Electron wave functions . . . . .	28
2.3.1 Electrons in a periodic solid . . . . .	28

---

2.4	Concepts of solid state physics . . . . .	30
2.4.1	The harmonic oscillator . . . . .	30
2.4.2	The origin of thermal expansion . . . . .	31
2.4.3	Lattice dynamics . . . . .	33
<b>3</b>	<b>Ab initio computation</b>	<b>39</b>
3.1	The basics about Density Functional Theory . . . . .	40
3.2	Spin in DFT . . . . .	43
3.3	The exchange functional . . . . .	44
3.4	Treating strongly correlated systems within DFT . . . . .	46
3.5	The pseudopotential and PAW method . . . . .	48
3.6	Brillouin zone integration . . . . .	51
3.7	Phonon calculations . . . . .	52
3.7.1	Finite difference method . . . . .	53
3.7.2	Linear response method . . . . .	54
3.7.3	Harmonic phonon calculations . . . . .	55
3.7.4	The quasi-harmonic approximation . . . . .	56
3.8	Cluster expansion . . . . .	58
3.8.1	The correlation function . . . . .	60
3.8.2	The Collony-Williams inversion . . . . .	60
3.8.3	The quality of a cluster expansion . . . . .	62
<b>4</b>	<b>Modelling</b>	<b>63</b>
4.1	Computational details . . . . .	63
4.1.1	The Metal-to-insulator transition . . . . .	63
4.1.2	Calculating heat capacities for $\text{Li}_x\text{CoO}_2$ . . . . .	65
4.1.3	Cluster expansions on $\text{Li}_x\text{Mg}_2\text{Si}$ . . . . .	66
4.2	Results & discussion . . . . .	67
4.2.1	Mapping the metal-to-insulator two-phase region . . . . .	67
4.2.2	Heat capacities within the QHA . . . . .	76
4.2.3	Cluster expansion of $\text{Li}_x\text{Mg}_2\text{Si}$ . . . . .	90

---

<b>5 Summary and outlook</b>	<b>95</b>
<b>Bibliography</b>	<b>111</b>
<b>Thank you</b>	<b>121</b>
<b>Appendices</b>	<b>123</b>
A A short guide to running the codes . . . . .	123
A1 The VASP input files . . . . .	123
A2 The Phonopy code . . . . .	124
A3 alloy theoretic automated toolkit (ATAT) . . . . .	127
B Supplementary data . . . . .	130
B1 Heat capacities within the QHA . . . . .	130
B2 The cluster expansion of $\text{Li}_x\text{Mg}_2\text{Si}$ . . . . .	133



# Chapter 1

## Introduction

### 1.1 The framework of this thesis

In our industrialized world the need for a stable and secure energy supply continuous to grow, with the rapid modernization of countries like China and India pushing resources to their limit. In the last 200 years mankind has been drawing energy mainly from the combustion of fossil fuels to power vehicles, private households and industry. In the second half of the century fission reactors were introduced as an alternative technology and reduced the dependence on coal as a resource. Over the course of the late twentieth century the common understanding formed that the anthropogenic emission of CO<sub>2</sub> is partly responsible for global warming. This had resulted in the change of policy in Germany during the 80s and 90s. During this time the term "Energiewende" emerged which was seized on again as a guiding principle within Germany's recent political agenda. The target is to reduce CO<sub>2</sub> emissions successively over a specified time-scale with pre-defined goals to achieve. This is accompanied by profound changes, e.g. the phasing out of coal power plants by successively cutting down on the number of active power plants. With the core melt accident in Fukushima in year 2011 the situation culminated in the decision to discontinue any use of nuclear fission to meet

the energy needs of the country. Given the fact that coal power plants were not considered a suitable technology any more this suggested the necessity of replacing nuclear fission reactors and coal power plants by increasingly more "green" technology such as solar, wind and water power. However, wind and solar power cannot guarantee a constant power output due to the intermittent availability of wind and sunlight. To accommodate fluctuations in the power output the capacity to store energy at times of high power output and its respective release at times of low power output has to be provided (load levelling) in a cost effective way. In this respect, hydroelectric dams and large scale batteries are the most feasible solutions.

Unfortunately, Germany does not have the geographical setting to rely on hydroelectric dams. Hence, batteries are needed for the purpose of energy storage. Currently, lithium ion batteries (LIBs) are the most advanced technology, providing high energy density (storable energy per mass) and cyclability (amount of charge and discharge cycles battery can tolerate before reaching end of life). The performance of lithium-ion batteries (LIBs) is shown

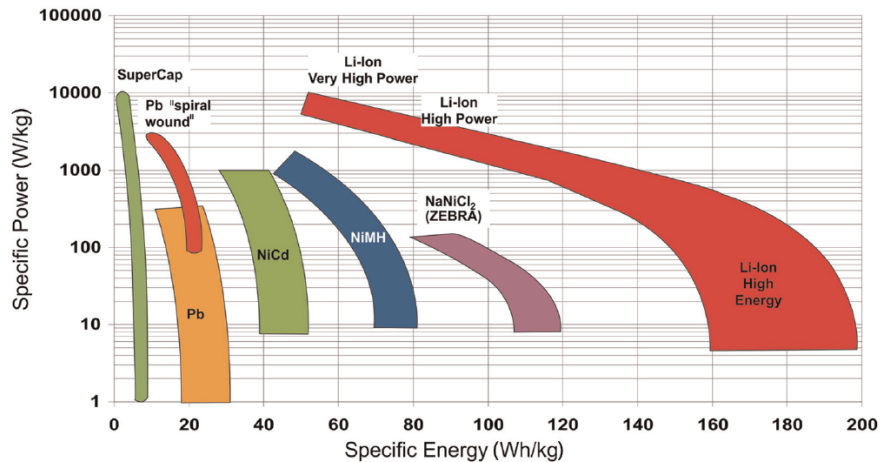


Figure 1.1: Ragone plot of different battery chemistries comparing specific power and specific energy [1]

in the Ragone plot in relation to other battery chemistries in figure 1.1. As can be seen, LIBs can outperform all of the fully developed chemistries and research continues to push this chemistry to reach its full potential. Furthermore, there are also new battery concepts under investigation such as the metal-metaloxide batteries which in theory can deliver a much higher specific energy than the current LIBs. Within the institute this direction is condensed in the project MEMO. However, the focus of this thesis as part of the project MEET-HiEnD and the Helmholtz-Portfolio is on LIBs.

In the framework of this thesis the target is to establish the methodological approach of calculating equilibrium properties of intercalation compounds for LIBs within the institute by means of atomistic modelling using density functional theory (DFT) calculations. The equilibrium properties provide key data (such as voltage and phase stabilities) essential to the design of reliable battery cells. In particular, we investigate the thermodynamic properties of  $\text{LiCoO}_2$  and  $\text{LiMg}_2\text{Si}_2$ . For the  $\text{LiCoO}_2$  system we modelled the metal-to-insulator two phase region in an effort to understand changes to the voltage profile. This was carried out by calculating the enthalpy of formation for the metallic and the semiconducting state over a series of stoichiometries. Furthermore, we investigated heat capacities in dependence of stoichiometry. Along with the thermal conductivity coefficients this thermodynamic property is of high relevance for proper thermal design of LIBs with  $\text{LiCoO}_2$  as cathode material due to thermal safety hazards during abuse operation (see subsection 1.7.3). The intention is to exploit the capabilities of DFT calculations due to deficiencies of an experimental approach. In particular when investigating delithiated compounds in this system the measurement of heat capacities are difficult because the material decomposes and can not be obtained easily as a pure phase sample. Hence, in this thesis the results between calculated and experimental data is being compared to elucidate the accuracy of the calculated data. Moreover, the effect of doping with boron is investigated. Lastly, a silicon based anode material,  $\text{Li}_x\text{Mg}_2\text{Si}$ , was inves-

tigated which could be a candidate for the next-generation anodes in LIBs. In this respect, the investigations were carried out by means of the cluster expansion method to more thoroughly explore the configurational space in dependence of lithium concentration in order to derive the average intercalation voltage.

## 1.2 Concept of electrochemical energy storage

The idea behind electrochemical energy storage is to convert chemical energy into electrical energy when needed to power an electrical device and vice versa when electrical energy is available to store it as chemical energy. The exothermic reaction of a compound A and B resulting in compound C and D provides electrical work which can then be used to power electric devices.



A might be an oxidant and B the reductant or vice versa with electrons flowing from B to A or from A to B respectively. The driving force for the reaction is the chemical potential difference of the transferred, specific chemical species between the educts whereas it's transfer proceeds from the higher to the lower chemical potential.

In an electrochemical cell the oxidant and the reductant are separated by an ionic conducting compound (electrolyte) so that the electron charges can flow separately from B (the anode) to A (the cathode). The electrode reactions can be defined as follows:



In the discharge mode the batteries operate like Galvanic cells, in which the electrochemical reaction takes place due to the electrochemical potential difference between the cathode and the anode. There are many electrochemical reactions. However, since certain criteria such as inherent safety, price, toxicity, energy density and rate of reaction have to be met, only few are suitable for battery applications.

Battery systems can be distinguished in a variety of ways, for instance: [2]

1. Primary (single use) versus secondary (rechargeable, multi-use) systems
2. Stationary systems (electrodes do not move) versus flow systems (redox moieties are in solution phases). Examples of important flow batteries are  $\text{ZnBr}_2$  and  $\text{V}^{2+} / \text{V}^{3+} - \text{V}^{4+} / \text{V}^{5+}$ .
3. LIBs using Li-metal as the anode material versus LIBs which contain no Li-metal and are usually rechargeable. Most of the practical LIBs utilize intercalation reactions at their cathodes:  
 $\text{Li}^+\text{MX}_y \longrightarrow \text{LiMX}_y$  where the intercalation materials are usually transition-metal oxides or sulfides ( $\text{M}=\text{Ni}, \text{Mn}, \text{Co}$ , etc. and/or their mixture:  $\text{X}=\text{oxygen}$  or sulfur). There are also cathode materials where  $\text{X}$  is  $\text{F}^-$ ,  $\text{SO}_4^{2-}$  or  $\text{PO}_4^{3-}$ . In LIBs the Li anode is replaced by intercalation compounds, alloys or even by transition-metal compounds where the transition-metal is in a low oxidation state. There are three main anodic reactions in Li ion batteries: intercalation [3], alloying [4], and conversion [5].
4. Aqueous versus non-aqueous batteries which have to use polar-aprotic electrolyte solutions due to reactivity considerations.
5. Metal-air batteries

In this type of battery the anode is a pure metal and the anode is the ambient air. Among metal-air batteries the primary (non-rechargeable)

zinc-air battery has already been in use for decades in low-current, long lifetime applications, e.g. hearing aids, isolated signal light, and electronic devices requiring operation over long periods of time in remote places. This battery type has received renewed attention for its potential use as large-scale energy storage system. However, metal-air batteries still suffer from reversibility issues and are therefore not considered as short-term secondary battery solutions. [6]

### 1.3 Lithium Ion batteries

Non-rechargeable LIBs developed in the 70s [7] employed metallic lithium as anode. Due to irreversible lithium loss during operation by its dendritic growth on the lithium anode these batteries could not be recharged. The first rechargeable LIBs with a graphite anode and  $\text{LiCoO}_2$  as cathode were introduced in 1991 by Sony. This led to the expansion of the market for mobile devices ever since. Rechargeable batteries used before the introduction of LIBs were for instance nickel-cadmium or lead-acid batteries. In comparison to these systems LIBs possess superior properties. Among those properties are the higher specific capacity and the high reversible cyclability. What is more, LIBs do not suffer from the memory-effect. Nowadays LIBs can be found literally in all mobile devices like laptops, tablets, camcorders, cameras and smartphones which provide people with an unprecedented mobility. Since then LIBs have gone through phases of development and optimization enhancing its performance. In a typical LIB at present the cathode material is comprised of a lithium-transition-metal-oxide as the cathode and graphite as the anode with a liquid organic electrolyte as shown in figure 1.2. The open-circuit voltage is determined by the difference in the chemical potential  $\mu_{\text{Li}}$  of lithium between the anode and the cathode [8]:

$$V(x) = -\frac{\mu_{\text{Li}}^{\text{cathode}}(x) - \mu_{\text{Li}}^{\text{anode}}}{zF} = -\frac{\mu_{\text{Li}}^{\text{cathode}}(x) - \mu_{\text{Li}}^{\text{anode}}}{F}, \quad (1.1)$$

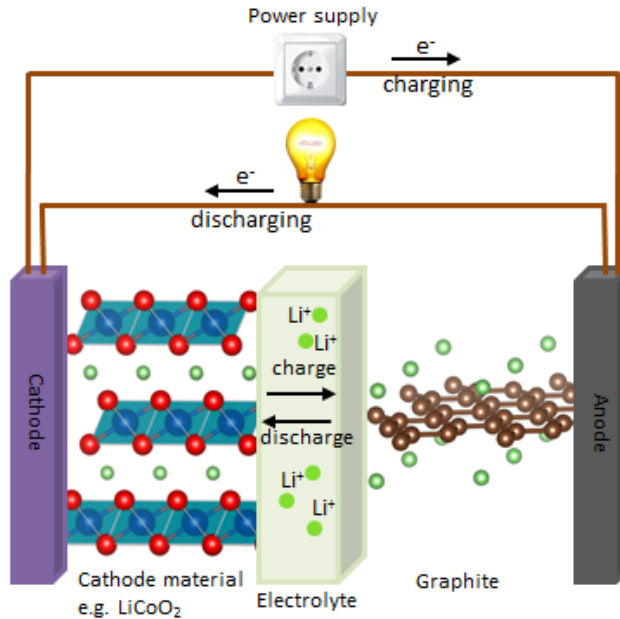


Figure 1.2: Schematics of a typical LIB with intercalation hosts as anode and cathode

where  $F$  is the Faraday constant and the charge  $z$  is equal to 1 in case of a LIB. In such a set-up as depicted in figure 1.2 the cathode is the capacity limiting component of the LIBs. Therefore, over the past decade reinforced research has been invested into the cathode development in order to extend the limitations imposed by the state-of-the art battery chemistries (figure 1.1). Nevertheless, research is carried out on the electrolyte and the anode as well since on the one hand all components have to be optimized with respect to each other (see section 1.9). On the other hand there is a search for entirely new materials with much higher specific capacities.

## 1.4 The solid electrolyte interface

The main electrolyte components of a LIB are lithium hexafluorophosphate ( $\text{LiPF}_6$ ) and organic carbonate solvents. [9] During the first charging cycle these carbonates (e.g. ethylene carbonate (EC), propylene carbonate (PC), diethyl carbonate (DEC), dimethyl carbonate (DMC), ethyl methyl carbonate (EMC)) decompose due to the low potential at the graphite electrode. The decomposition products react with lithium-ions which diffuse from the host electrode to graphite thus forming a reacted layer on top of the graphite electrode. Therefore, a fraction of lithium ions is irreversibly lost to the formation of this layer during the first cycle. This layer is called the solid electrolyte interface (SEI). However, the growth of the SEI stops after a certain amount of time since electrons are not able to pass it, thereby inhibiting the continued reduction of the electrolyte components. The detailed mechanism is as follows:

In the organic electrolyte solution the lithium-ions exist as solvated ions in the form of Li-ion-solvent-adducts. These continue to diffuse to the graphite electrode and penetrate to intercalate in between the graphite layers. However, due to the reducing conditions the solvents soon get decomposed forming a hardly soluble reaction product. In general, these are lithium-Alkyl-carbonates  $\text{Li}[\text{OC}(\text{O})\text{OR}]$  and  $\text{Li}_2[\text{OC}(\text{O})\text{O}-(\text{CHR})_n-\text{O}(\text{O})\text{CO}]$ . Other reaction products are possible depending on the exact chemistry of the electrolyte [10]. Since the reaction product is electrically insulating, a continued reductive decomposition of the electrolyte components is inhibited. Moreover, when further lithium-ion-solvent-adducts pass the SEI, the lithium-ion strips off the solvating molecules and continues to move into the graphite electrode as the bare ion (figure 1.3). Apart from inhibiting a continued loss of lithium-ions and active electrolyte components the SEI also protects the graphite from too extreme volume changes induced by repetitive intercalation and deintercalation of the lithium-ion-solvent-adducts which would otherwise lead to a fast deterioration of the electrode integrity and rapid fail-

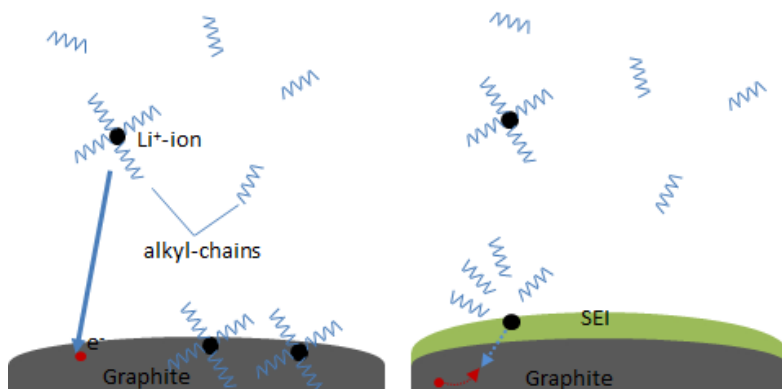


Figure 1.3: The process of SEI formation: lithium-alkyl carbonates form the SEI, eventually the formed SEI layer prevents further growth.

ure of the battery. No matter what carbonates are employed charging always leads to the SEI formation. Nevertheless the chemistry has been optimized over the last 20 years and it has been found that the quality of carbonates decreases in the order of EC » DMC » EMC » DEC » PC in terms of their respective reduction potential. The structure and properties of the SEI can be significantly influenced by using additives which are basically designed to react instead of the carbonates. This is exploited systematically by choosing additives which decompose earlier in the charging process.

In the past recent years SEI formation has also been studied on the high potential electrode when it became conceivable that the electrolyte components would not be stable against oxidation at higher electrode potentials aimed for with the 5-V electrodes. Examples are the high-voltage spinels and  $\text{LiCoPO}_4$ . The strategy has been analogous to the graphite electrode so far by means of developing additives which are more prone to being oxidized than the active electrolyte components. [11]

## 1.5 The Graphite anode

Depending on the morphology of the carbonaceous material the specific capacity can vary significantly. Hard carbon was employed in the 2nd generation of LIBs whereas graphite was eventually used in the 3rd generation [7] owing to the good reversibility of the lithium intercalation. Its low electrochemical potential of 0 to 0.25 V vs lithium is one of its most favourable properties. Lithium can intercalate up to a stoichiometry of  $\text{LiC}_6$  which equals a specific capacity of 372 mAh/g. The intercalation takes place in a sequence of steps during which different stoichiometric compounds can be observed, also termed graphite intercalation compound (GIC). These are for instance  $\text{LiC}_{12}$ ,  $\text{LiC}_{18}$  and  $\text{LiC}_{25-30}$ . At low charging rates the theoretical specific capacity of 372 mAh/g can indeed be achieved. However, the material suffers from drawbacks such as poor cyclability and volume changes which lead to significant deformation of the material. [11]

## 1.6 Layered oxides as intercalation cathode materials

Conceptionally, layered structures provide two-dimensional pathways for the lithium-ions to diffuse as is the case for graphite. That is the essential condition for sufficient mobility of the lithium-ions. Among the chemistries of layered transition-metal-oxides the chemistry of  $\text{LiCoO}_2$  was the first to enter the commercial market.

The general structure is a stacking arrangement of alternating planes of lithium, oxygen and transition metal ions. The crystal system is hexagonal but can be described in a lower symmetry setting as well (rhombohedral centered). Since the lithium ions are too small, close packing is not achieved. The oxygen and cobalt ions form octahedrals connected to form sheets. The layered oxides can exist in various polytypes of which the so-

called O3-LiCoO<sub>2</sub> is the structure commonly found in commercial LIBs. The other polytypes are: O2-, O4- and O6-LiCoO<sub>2</sub>. The different polytypes are displayed in figure 1.4. Among these the metastable O2-LiCoO<sub>2</sub> was first synthesized by Mendiboure et al. by Na<sup>+</sup>/Li<sup>+</sup> exchange from the P4-Na<sub>0.70</sub>CoO<sub>2</sub> [12]. O4-LiCoO<sub>2</sub> was termed metastable by Berthelot et al. since

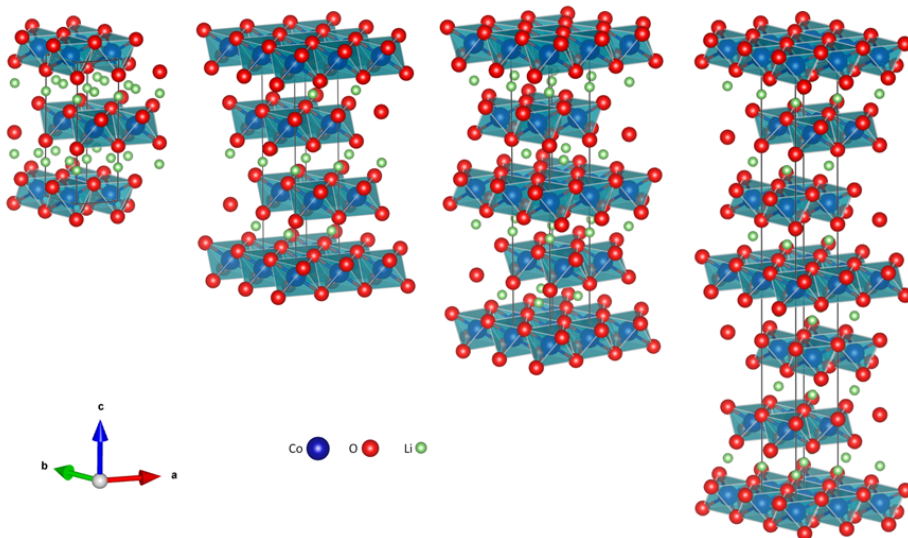


Figure 1.4: The different layered polytypes of LiCoO<sub>2</sub>: starting from the left O2-, O3-, O4- and O6-LiCoO<sub>2</sub>

it transforms to the O3-LiCoO<sub>2</sub> at temperatures between 350 and 400 °C [13]. The nomenclature is defined by the letter 'O', an abbreviation for the octahedral sites in which the lithium ions reside, followed by a number. The numbers define the number of sheets after which the translational symmetry is achieved again. So in O2-LiCoO<sub>2</sub> there are two, in O3-LiCoO<sub>2</sub> three and O6-LiCoO<sub>2</sub> six layers of stacked lithium, oxygen and cobalt ions in the rhombohedral centred setting of the unit cell.

Investigations on the modifications  $\text{LiNiO}_2$  and  $\text{LiMnO}_2$  have also been carried out and are still subject to research as possible materials with lower toxicity and costs.  $\text{LiNiO}_2$  by itself is unsuitable since there has been difficulties in synthesizing the compound in the right stoichiometry. This is due to the fact that the nickel-ions partially reside within the lithium-layer. Consequently, the theoretic capacity is being impaired. Moreover, during delithiation  $\text{LiNiO}_2$  tends to release oxygen which can cause exothermic reactions with the organic components of the electrolyte (see subsection 1.7.3), a severe safety concern.  $\text{LiMnO}_2$  on the other hand transforms into the spinel-type structure during delithiation which also leads to a decrease in the available capacity. In order to keep the basic electrochemical properties of  $\text{LiCoO}_2$  with the advantage of lower costs and toxicity much effort has been spent in the investigation of partial substitution of cobalt with nickel and manganese [14] leading to the development of lithium-nickel-manganese-cobalt oxides (Li-NMC cathodes). These chemistries offer slightly superior safety. [15]

## 1.7 Properties of $\text{LiCoO}_2$

### 1.7.1 Structural stability

Extensive studies have been carried out on the layered O3- $\text{LiCoO}_2$  in the last 20 years including electrochemical testing [16–20], structural analysis with TEM [19,21], XRD [22,23] and SEM [24–27], analysis of the electronic [28,29] and magnetic properties [30,31], examination of phase stabilities [21,32–34], synthesis [35–38] and morphological investigations [19,26,27,39–42]. This material has shown to possess a complex behaviour in terms of phase stability and phase transformations upon lithium intercalation and removal. The phase transformations are of both electronic and crystallographic nature [43,44]. With respect to crystallographic phase transformations the O3- $\text{LiCoO}_2$  solid solution shows different vacancy ordering phenomena during successive

lithium removal. Reimers et al. [45] were the first to observe the in-plane vacancy ordering at a lithium content of  $x=0.5$  which can be described by every other lithium lattice site in either a or b direction being occupied by a vacancy. This is illustrated in figure 1.5. A consequence of this ordering is a

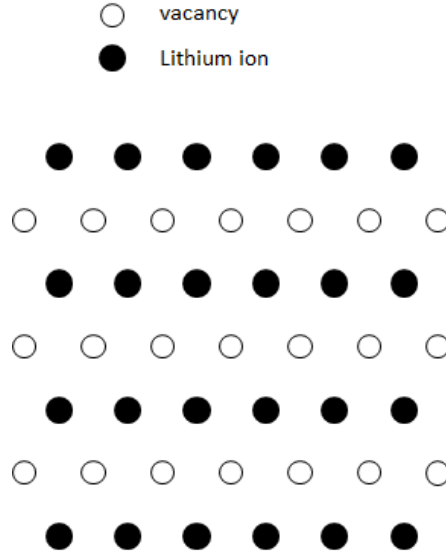


Figure 1.5: In-plane vacancy ordering at a lithium-concentration of  $x=0.5$

slight monoclinic distortion of the whole structure and is hence detected via x-ray diffraction (XRD) (see figure 1.6). Upon further lithium removal another ordered arrangement becomes thermodynamically favourable in which the planes shift with respect to each other, ultimately forming a stacking of the type 'AABCAABC', which was therefore termed H1-3- $\text{LiCoO}_2$ . It is remarkable that this stacking arrangement was first suggested from results of first-principles calculations by Van der Ven et al. before there was any experimental evidence [32]. The designation accounts for the stacking, which resembles a hybrid between the O1- and the O3- $\text{LiCoO}_2$  in an alternating fashion. Complete removal of the lithium-ions results in the O1- $\text{CoO}_2$ . These

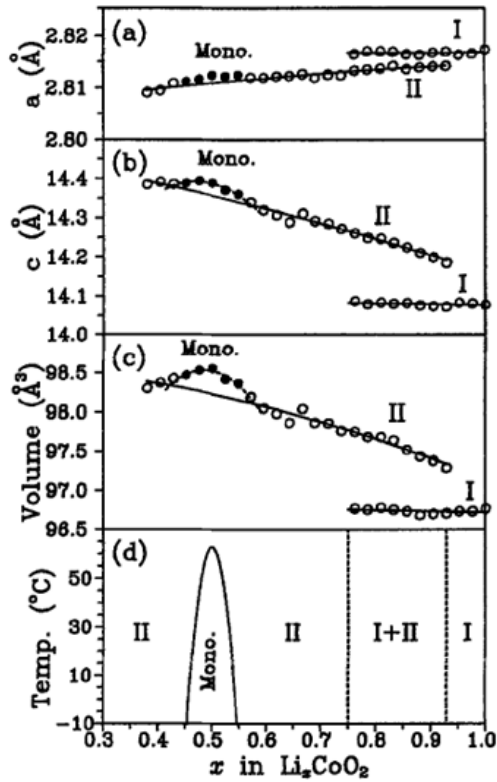


Figure 1.6: Lattice parameters in dependence of lithium content at room temperature (a),(b) and (c) as well as phase diagram by Reimer et al. in dependence of lithium content in the O3- $\text{LiCoO}_2$  (d)

phase relations were assessed by Chang et al. [44] and the results can be seen in figure 1.7. Moreover, there is both experimental and theoretical evidence that the O3- $\text{LiCoO}_2$  gets less stable compared to the spinel-type  $\text{LiCo}_2\text{O}_4$  when lithium is removed [46].

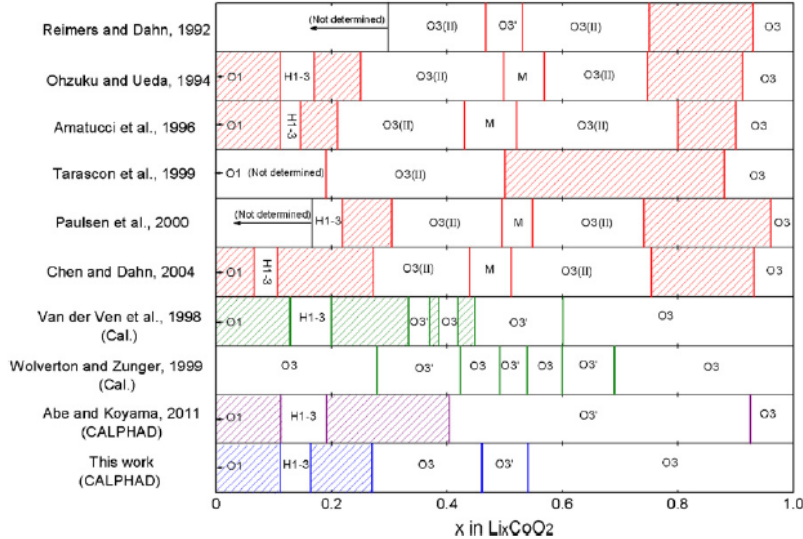


Figure 1.7: The phase diagram of  $\text{LiCoO}_2$  at 298 K in different thermodynamic assessments as compiled in [44]

Experimental studies on operated  $\text{LiCoO}_2$  indeed confirmed the formation of H1-3- $\text{LiCoO}_2$  and spinel-type  $\text{Li}_{1+y}\text{Co}_2\text{O}_4$  in heavily cycled O3- $\text{LiCoO}_2$  and that capacity loss is amongst other causes ascribed to these irreversible transformation products due to their lower capacity to intercalate lithium [21]. Another contribution to the capacity fade of  $\text{LiCoO}_2$  is possibly made by the contraction and expansion of the interslab distance upon lithium removal and reinsertion, which may be causing damage to the structural integrity of the material. Consequently, some research effort has been devoted to mitigate the extent of the contractions. Doping with Mg-ions have shown to improve the capacity retention due to the migration of the Mg-ions to the interslab layers providing a pillaring effect and therefore preventing a significant contraction of the interslab distance [47, 48].

The electronic phase transformation for  $x \in [0.75; 0.94]$  was first detected by Reimer et al. [49] by XRD although at that time the authors were not aware

of the electronic nature of this transformation. The XRD solely revealed

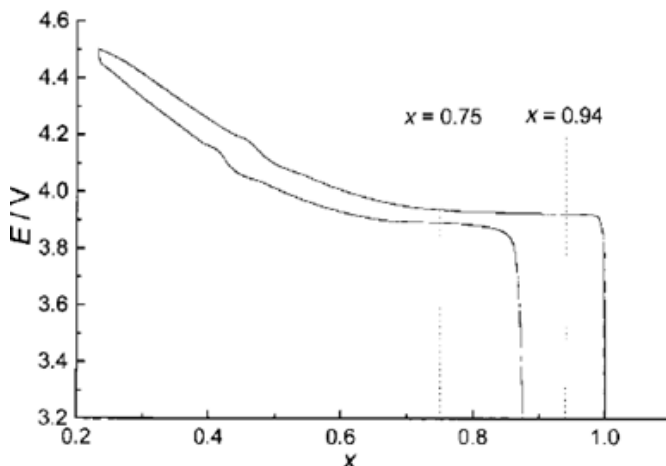


Figure 1.8: The voltage profile of  $\text{O3-Li}_x\text{CoO}_2$  vs lithium with the plateau in the metal-to-insulator 2-phase region: the charging starts from  $x=1$  until reaching a voltage of 4.5 V, subsequently the discharge curve is displayed up to  $x=0.88$

that a two-phase region existed with two different sets of lattice parameters within the same space group  $R\bar{3}m$  (166) (see figure 1.6). Ménétrier et al. [50] reinvestigated this issue by means of Li NMR and XRD and were able to attribute the phase transformation to a metal-to-insulator transition (MIT) as suggested by theoretical calculations of Van der Ven et al. [32] a year before. It is because of this two-phase region that the typical voltage profile of  $\text{LiCoO}_2$  versus lithium exhibits a plateau in this lithium concentration range [50] as can be seen in figure 1.8.

Another process affecting the structural stability of the  $\text{O3-Li}_x\text{CoO}_2$  occurs at deep lithium extraction close to  $x=0.5$  at which point oxygen loss limits the practical capacity. This oxygen loss is due to the hybridization of the oxygen 2p orbitals with the cobalt 3d orbitals leading to an orbital overlap as seen in figure 1.9 as evidenced by the investigations of Venkatraman and Manthiram

[51]. Their findings are supported by the results of ab initio calculations of Van der Ven et al. [32] and spectroscopic observations of Montoro et al. [52]. In the process of lithium extraction, first,  $\text{Co}^{3+}$  gets oxidized by the removal of 3d electrons. At later stages of this oxidation process  $\text{O}^{2-}$  starts to get oxidized when reaching the energy levels of the oxygen p orbitals, ultimately leading to the formation and release of molecular oxygen.

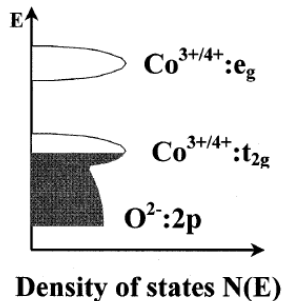


Figure 1.9: The electronic DOS of  $\text{Li}_x\text{CoO}_2$  taken from Venkatraman and Manthiram [51]: overlap of the O-2p and the Co-3d orbitals leads to the oxidation of oxygen at deep lithium extraction close to  $x=0.5$  prompting the formation of oxygen. This imposes a limit to the reversible capacity of  $\text{Li}_x\text{CoO}_2$ .

### 1.7.2 The metal-to-insulator transition of $\text{LiCoO}_2$

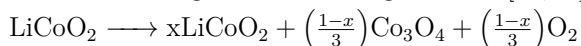
The MIT can be explained within the framework of an impurity model. [53, 54] It is used to describe the effects of high doping concentrations ( $n_I = 10^{18} \text{ cm}^{-3}$  in case of doped silicon [55]) on the band structure of semiconductors. In a semiconductor, just like  $\text{LiCoO}_2$ , the valence band is separated from the conduction band by a band gap which leads to conduction only at sufficiently high temperatures to excite electrons from the valence band to the conduction band. In the specific case of  $\text{LiCoO}_2$  the band gap is 2.7 eV. Delithiation of  $\text{LiCoO}_2$  leads to a lack of positive charge in the struc-

ture which is compensated by the oxidation of cobalt ions from  $\text{Co}^{3+}$  to  $\text{Co}^{4+}$ . This increased positive formal charge essentially means that an electron from the cobalt d-orbitals is removed leaving an electronic hole behind. At very low lithium deficiencies (close to  $x=1$ ) the concentration of these electronic holes is therefore analogously low, too, and assuming a random distribution, these holes are separated by rather large distances on average. An increasing delithiation lowers the average distances whereas local accumulations of electronic holes lead to the overlap of the wave functions of the hole states causing the formation of new bands (impurity bands) which are well separated from the valence and conduction band. Even further delithiation leads to the broadening of the impurity bands due to the increasing overlap, causing a merging of the impurity bands with the valence and conduction band, respectively. At this stage, this is observable as tails in the electronic DOS [56] as has been observed by Marianetti et al. [53]. Developing further thoughts a continuous increase of those impurities ( $\text{Co}^{4+}$ /holes for the case at hand) ultimately leads to the complete vanishing of the band gap in the course of the broadening of the tails. It thus explains the transition from a semiconducting to a metallic behaviour in  $\text{LiCoO}_2$ .

### 1.7.3 Behaviour at elevated temperatures

The material class of lithium-transition metal oxides including  $\text{LiCoO}_2$  are sensitive to temperature increase. In general, storing batteries with these cathode materials at slightly elevated temperatures leads to an increase in self-discharge. Commercial  $\text{LiCoO}_2$ -based batteries by Sanyo have been reported to show a capacity retention of 93, 89 and 75 % after storage at 0, 25 and 60 °C, respectively, for 6 months [57]. Thermal runaway is an issue in LIBs with lithium transition metal oxides as cathode material. This undesirable cascade reaction can be triggered during abuse operation of the battery by over-charging in combination with elevated environmental temperatures. The induced cascade reaction itself generates additional heat so that the ul-

timate consequences can be severe. The series of processes of the cascade reaction include the decomposition of the SEI which normally protects the negative electrode from reactions with the electrolyte, the vaporization of the organic electrolytes typically used, the exothermic reaction of the hence unprotected negative electrode releasing oxygen which in turn reacts with the electrolyte components in a highly exothermic process. Oxygen release occurs according to the following reaction [58, 59]:



The temperature increase can ultimately lead to the melting of the separator and consequently to a short circuit causing additional heating. This poses a significant fire and explosion hazard. The onset temperature of thermal runaway varies depending on the exact chemistry of the battery components. It has been proposed to be 85°C obtained from thermal modelling by Spotniz and Franklin [60]. Experimentally the onset temperature for Sony US18650 cells has been determined to be 144 °C at 2.8 V, 109 °C at 3 V and 104 °C at 4.06 V by Al Hallaj et al. [61].

## 1.8 Mg-Si-alloys as alloying anode material

Alloying reactions of different metals with lithium have received attention from the battery community due to the potentially higher theoretical capacity. This is related to the nature of the reaction mechanism to form intermetallic alloys in such cases opposed to intercalation compounds in presently available, commercial electrode materials. This analysis has to be taken with care since the theoretical capacity in these cases (4200 mAhg<sup>-1</sup> and 2400 mAhcm<sup>-3</sup> for silicon) are simply derived from the maximum ratio of lithium to metal atoms in existent intermetallic compounds. While the commercially used graphite-anode can host 6 intercalated lithium ions per carbon atom LiC<sub>6</sub> metals like germanium, tin, silicon and lead can form compounds with more than 4 Li atoms per metal alloying atom to form Li<sub>22</sub>M<sub>5</sub>. [62]

Silicon-based alloys containing other metals than silicon itself have been investigated as well due to their more favorable voltage profile and reversible capacity [63].

The Mg-Si system has been under reinforced investigation as a potential material system to be used in anodes of LIBs. Within the ternary Li-Mg-Si system many of the thermodynamically stable phases have been identified and provide a solid basis for directed investigations [64]. Among the multitude of compounds within the Li-Mg-Si system the  $\text{Mg}_2\text{Si}$  compound has been investigated both experimentally and theoretically by means of DFT modelling [3, 65–67].

Studies were performed on the  $\text{Mg}_2\text{Si}$  compound with respect to its potential as an anode material. In this context, it was found that  $\text{Mg}_2\text{Si}$  is in fact an "end member" of the solid solution phase  $\text{Li}_x\text{Mg}_2\text{Si}$  as highlighted in figure 1.10 with an estimated solubility of  $x \in [0; 0.91 \pm 0.05]$  [64].

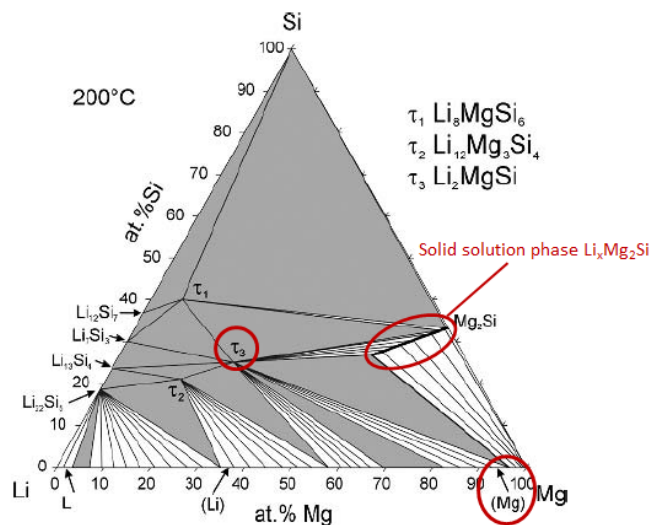


Figure 1.10: The Li-Mg-Si phase diagram at 200°C with the solid solution phase  $\text{Li}_x\text{Mg}_2\text{Si}$ , (Mg) and  $\tau_2$  constituting the 3 phase field, adapted from [64].

Consequently, using  $\text{Mg}_2\text{Si}$  as a starting composition for lithiation will inevitably first lead to the formation of the solid solution phase  $\text{Li}_x\text{Mg}_2\text{Si}$ , which is essentially an intercalation reaction. This compound is displayed in figure 1.11. As can be seen the geometry shows a fundamental difference to the layered transition metal oxides shown in figure 1.4. The  $\text{Li}_x\text{Mg}_2\text{Si}$  compound is a non-layered structure similar to olivine-, spinel- and tavorite-type intercalation compounds [68].

Exceeding the solubility limit leads to the precipitation of two phases in a three phase field as can be seen in figure 1.10:  $\text{Li}_2\text{MgSi}$ , designated  $\tau_2$ , and  $\text{Mg}_x\text{Si}_{1-x}$ , designated (Mg). For  $\text{Li}_2\text{MgSi}$  a new structure was predicted to be more stable by DFT calculations. The latest thermodynamic assesment by Kevorkov et al. was carried out before this discovery. Hence, a remodelling of the three-phase field may be necessary.

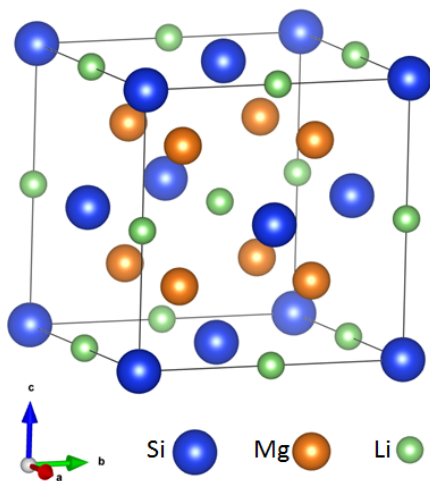


Figure 1.11: The crystal structure of  $\text{Li}_x\text{Mg}_2\text{Si}$ : this compound has a cubic unit cell and crystallizes in space group F-3m (225). The crystal structure data is taken from Imai et al. [67]

## 1.9 The voltage window

The voltage of a LIB is defined by the difference in chemical potential of lithium between the cathode and the anode. During operation this difference may change continuously due to the variation of lithium content in both electrodes. It is imperative to know the boundaries of the voltage window suitable for the battery chemistry at hand. In general, the properties of the three main cell components (anode, electrolyte and cathode) put a constraint on the voltage window. On the one hand it is restricted by the amount of reversibly extractable lithium ions from the cathode host. But on the other hand the employed electrolyte imposes a constraint as well as already mentioned in section 1.4. The window imposed by the electrolyte is determined by the lowest unoccupied molecular orbital (LUMO) and the highest occupied molecular orbital (HOMO) in case of a liquid electrolyte or by the bottom of the conduction band and the top of the valence band in case of a solid electrolyte. If the electrochemical potential moves beyond these limits then the electrolyte gets either oxidized or reduced. This is conceptionally illustrated in an energy diagram (figure 1.12) displaying the electron energies in the cathode, electrolyte and anode. Starting condition is the charging of

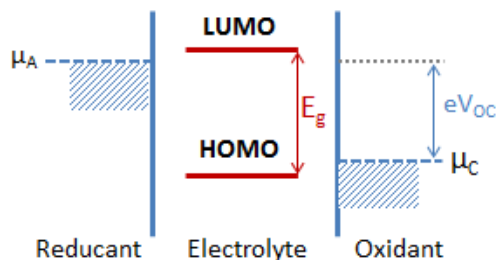


Figure 1.12: Illustration of the operational voltage window of a LIB in an energy diagram [69].

the LIB with a layered lithium transition metal compound which represents

the anode in this setting since during the extraction process oxidation takes place ( $\text{Co}^{3+}/\text{Co}^{4+}$ ). We term the electrochemical potential of the anode  $\mu_A$ . The electrochemical potential of the cathode (graphite) will be  $\mu_C$ . If  $\mu_A$  lies above the LUMO or the bottom of the conduction band, then electrons get transferred to the electrolyte. This means that the electrolyte is being reduced. If  $\mu_C$  lies below the HOMO or the top of the valence band then electrons from the electrolyte HOMO get transferred to the cathode and the electrolyte is oxidized in this process. Both the uncontrolled oxidation and reduction of the electrolyte have adverse effects on the capacity and cycle life of the battery. Uncontrolled reduction at the anode and oxidation at the cathode leads to the irreversible loss of electrolyte components and salts and, depending on the electrolyte composition, to the formation of by-products on the electrode surfaces, which can give rise to a layer of increased ohmic resistance. Consequently, the impedance of the LIB would be unfavourably affected [70, 71].

To sum up, the development of batteries has to be carried out as a whole system. Modifying the cathode requires the evaluation of its impact on possible undesired reactions with the other components which might compromise the batteries performance. The same applies to the anode and the electrolyte respectively.



# Chapter 2

## Theory

### 2.1 Thermodynamic potentials

Thermodynamic potentials are state functions which describe the equilibrium behaviour of systems with a set of variables, called 'natural variables', through its maximization or minimization with respect to one particular variable keeping all other variables constant. Therefore, if the state functions can be determined as a function of these respective variables all other thermodynamic properties can be obtained by calculating its partial derivatives. All state functions can be related to the fundamental equations of thermodynamics by so-called Legendre transformations.

The scenario, from which the fundamental equations of thermodynamics are derived, resembles an isolated system meaning that no heat  $Q$  and no particle  $N$  can be exchanged with the surroundings as well as no volume ( $V$ ) work can be exerted (system cannot expand) due to imposed constraints. The equilibrium properties are derived by maximizing the system's entropy at constant  $U, V, N$ . However, in general, these conditions are difficult to maintain for any experiment. For experiments the most convenient constraints are usually constant temperature and pressure, which are put into practice by means of ovens or cooling systems and an unsealed vessel allowing the

system to expand to maintain the surrounding's pressure. In this case a new thermodynamic potential is necessary to derive the equilibrium properties which is the Gibbs free energy. This thermodynamic potential is yielded by applying the Legendre transformation. Using Legendre transformation the thermodynamic potential  $U$  can be transformed to obtain the Gibbs free energy ( $G$ , also termed free enthalpy), enthalpy ( $H$ ) and Helmholtz free energy (commonly termed  $F$ ,  $H$  or  $A$ ).

The Helmholtz free energy is a thermodynamic potential which is used when temperature, volume and the number of particles are the independent properties of the system since they are the natural variables of the Helmholtz free energy. It is defined as  $F = F(T, V, N) = U - TS$ . As is described in chapter 3.7 the Helmholtz free energy is a particularly convenient thermodynamic potential to chose when deriving thermodynamic properties from first-principles based calculations. The fundamental thermodynamic equations for  $F$  by taking the partial derivatives are:

$$S = -\left(\frac{\partial F}{\partial T}\right)_{V,N}$$

$$U = F - T\left(\frac{\partial F}{\partial T}\right)_V = -T^2\left(\frac{\partial}{\partial T}\frac{F}{T}\right)_V$$

$$C_V = \left(\frac{\partial U}{\partial T}\right)_V = T\left(\frac{\partial S}{\partial T}\right)_V = -T\left(\frac{\partial^2 F}{\partial T^2}\right)_V$$

$$p = -\left(\frac{\partial F}{\partial V}\right)_T$$

$$B_T = V\left(\frac{\partial^2 F}{\partial V^2}\right)_T = -V\left(\frac{\partial p}{\partial V}\right)_T$$

$$\left(\frac{\partial p}{\partial T}\right)_V = \alpha B_T = -\frac{\partial}{\partial V}\left[\left(\frac{\partial F}{\partial T}\right)_V\right]_T = -\left(\frac{\partial S}{\partial V}\right)_T$$

$C_V$  is the specific heat at constant volume,  $B_T$  is the isothermal bulk modulus and  $\alpha$  is the volume coefficient of thermal expansion. [72]

## 2.2 Equation of states

Since in the context of phonon calculations thermal properties are obtained from a fitting procedure to an equation of state (EOS) (see section 3.7), this section serves as a quick introduction into this topic. An EOS relates thermodynamic state variables to each other. Such state variables are pressure  $p$ , volume  $V$  and temperature  $T$ . The most prominent and simple one is the ideal gas law, which is adequate to describe the state of a gas in the limit of low pressure and high temperature. EOS are all empirical or semi-empirical in the sense that they contain coefficients which are fitted in a minimization procedure. In Materials Science these coefficients are most commonly the bulk modulus and the thermal expansion coefficient. The EOS is either given in the form of  $P(V)$  or  $E(V)$ . However, in the context of ab initio calculations the EOS are used in the integrated form, i.e.  $E(V)$ . In this manner the function of the integrated EOS is then fitted to the ab initio total energies obtained for different volumes according to the general relation [73]:

$$dE = -pdV \quad (2.1)$$

Some of the most common EOS used to describe the behaviour of solids under compression or expansion are:

- Vinet EOS:

$$P(V) = 3B_0 \left(\frac{V}{V_0}\right)^{-\frac{2}{3}} \left[1 - \left(\frac{V}{V_0}\right)^{\frac{1}{3}}\right] \exp \left[ -\frac{3}{2}(B'_0 - 1) \left[ \left(\frac{V}{V_0}\right)^{\frac{1}{3}} - 1 \right] \right] \quad (2.2)$$

$$E(V) = E_0 + \frac{2B_0V_0}{(B'_0 - 1)^2} \left[ 2 - \left[ 5 + 3 \left(\frac{V}{V_0}\right)^{\frac{1}{3}} (B'_0 - 1) - 3B'_0 \right] \right] \\ \cdot \exp \left[ -\frac{3}{2}(B'_0 - 1) \left[ \left(\frac{V}{V_0}\right)^{\frac{1}{3}} - 1 \right] \right] \quad (2.3)$$

- Murnaghan EOS:

$$P(V) = \frac{B_0}{B'_0} \left[ \left( \frac{V}{V_0} \right)^{B'_0} - 1 \right] \quad (2.4)$$

$$E(V) = E_0 + \frac{B_0 V}{B'_0} \left[ \left( \frac{V_0}{V} \right)^{B'_0} \frac{1}{B'_0 - 1} + 1 \right] - \frac{B_0 V_0}{B'_0 - 1} \quad (2.5)$$

- Third-order Birch-Murnaghan EOS:

$$P = \frac{3B_0}{2} \left[ \left( \frac{V}{V_0} \right)^{7/3} - \left( \frac{V}{V_0} \right)^{5/3} \right] \left[ 1 + \frac{3}{4} (B'_0 - 4) \left[ \left( \frac{V}{V_0} \right)^{2/3} - 1 \right] \right] \quad (2.6)$$

$$E(V) = E_0 + \frac{9V_0 B_0}{16} \left[ \left[ \left( \frac{V_0}{V} \right)^{\frac{2}{3}} - 1 \right]^3 B'_0 + \left[ \left( \frac{V_0}{V} \right)^{\frac{2}{3}} - 1 \right]^2 \left[ 6 - 4 \left( \frac{V_0}{V} \right)^{\frac{2}{3}} \right] \right] \quad (2.7)$$

$B_0$  denotes the bulk modulus,  $B'_0 = \frac{dB}{dV}$ ,  $V$  the volume,  $p$  the pressure and the index 0 denoting the state at equilibrium.

## 2.3 Electron wave functions

As will be described in chapter 3 DFT calculations rely on the quantum-mechanical treatment of electrons in the atomic potential. There is a big difference in treating electrons in a crystalline structure, which obey translational symmetry in opposition to treating electrons in isolated molecules. That is also the reason why DFT codes designed for treating molecules are fundamentally different from DFT codes designed for treating solid state.

### 2.3.1 Electrons in a periodic solid

Conceptionally, in a periodic solid the valence electrons can be assumed to be affected only by a weak Coulomb potential of the atomic core. This is re-

lated to the fact that the electrons close to the core partially screen the core potential of  $Z_\alpha e$  (with  $Z$  the atomic number and  $e$  the elemental charge). Consequently, the valence electrons see only a reduced effective potential. To simplify the model the valence electrons can be treated independently in a first approximation. The wave function of these independent electrons moving in a crystalline solid have to fulfil certain conditions. The atom nuclei impose a periodic potential  $U(\vec{r})$  acting upon the electron wave functions. Due to the periodicity of the potential the Hamilton operator of the Schrödinger equation for a single independent electron would take on the following form:

$$H\Psi = \left( -\frac{\hbar^2}{2m}\nabla^2 + U(\vec{r}) \right) \Psi = \epsilon\Psi \quad (2.8)$$

The Schrödinger equation of a free electron is a special case of equation 2.8, in which the periodic potential is simply zero. Assuming electrons to be independent in a periodic potential is the basis for the so-called Bloch's theorem, in which the eigenstates  $\Psi$  of the Hamiltonian in equation 2.8 with  $U(\vec{r} + \vec{R}) = U(\vec{r})$  are described by equation 2.9:

$$\Psi_{n\vec{k}}(\vec{r}) = e^{i\vec{k}\cdot\vec{r}} u_{n\vec{k}}(\vec{r}) \quad (2.9)$$

Essentially it is the product of a plane wave  $e^{i\vec{k}\cdot\vec{r}}$  and a periodic function  $u_{n\vec{k}}(\vec{r})$ .  $\vec{k}$  denotes a wave vector in reciprocal space. This function, called the Bloch-wave, is a periodic plane-wave with the translational symmetry of the lattice. In equation 2.9 the plane wave is written in its exponential representation, but it can be decomposed into cosinus and sinus functions according to:

$$e^{ix} = \cos x + i \sin x \quad (2.10)$$

## 2.4 Some concepts of solid state physics

Solid state physics form the theoretical foundation for the employed calculation methods to a great extent. To understand the principles behind these methods some concepts and theories are recalled in this section to serve as a linking element to chapter 3.

### 2.4.1 The harmonic oscillator

The harmonic oscillator is an ubiquitous concept in both science and engineering to describe and explain analogous phenomena as for instance a pendulum, acoustic and electromagnetic waves. Therefore it is not limited to the field of Solid state physics. Although simplifying it often provides a conceptual apt view on matters which are related to vibrations and wave propagation. The harmonic oscillator is most intuitively accessible in the context of a mechanical harmonic oscillator like a mass attached to a spring. Displacing the mass to stretch the spring induces a restoring force acting in the opposite direction of the displacement. In the context of a harmonic oscillator the restoring force is linearly proportional to the displacement:

$$F = -kx \quad (2.11)$$

To study the equation of motion it is necessary to look at the general relation between force and momentum.

$$F = \frac{dp}{dt} = \frac{d(mv)}{dt} = m \frac{dv}{dt} = m \frac{d^2x}{dt^2} \quad (2.12)$$

Combining equations 2.11 and 2.12 shows that the product of mass  $m$  and the second derivative of  $x$  with respect to the time  $t$  is supposed to yield the product of  $x$  and a constant:

$$m \frac{d^2x}{dt^2} = -kx \Rightarrow \frac{d^2x}{dt^2} = -\frac{k}{m}x \quad (2.13)$$

A function  $x(t)$  meeting this requirement in equation 2.13 is the sine or cosine function. Therefore this suggests equation 2.14 to be the potential solution:

$$x(t) = A \cos(\omega t) + b \sin(\omega t) \quad (2.14)$$

Substituting this solution into equation 2.13 yields:

$$-\omega^2 A \cos(\omega t) - \omega^2 b \sin(\omega t) = -\frac{k}{m} [A \cos(\omega t) + b \sin(\omega t)] \quad (2.15)$$

At this point it can be deduced that the assumed solution is a solution only then if:

$$\omega^2 = \frac{k}{m} \Leftrightarrow f = \frac{1}{2\pi} \sqrt{\frac{k}{m}} \quad (2.16)$$

Equation 2.16 essentially states that the eigenfrequency of a harmonic oscillator is determined by the force constant of the spring and the mass of the oscillator and is used to determine the frequencies of phonons as described later on in section 3.7.

### 2.4.2 The origin of thermal expansion

Along the lines of a harmonic potential well between the atoms in a solid, thermal expansion cannot be explained. Only the equilibrium atomic distance is defined in the minimum at  $r = r_0$ . An increase of temperature induces oscillations along the tie line connecting two atoms. Due to the har-

monic potential, which is symmetric, the amplitudes are equal to both sides of  $r_0$ . In consequence, even upon temperature rise the probability density distribution of the atoms location remains symmetric and hence the atomic distance stays constant. A more realistic empirical model of the atomic potential, which is also able to explain thermal expansion, is an anharmonic potential as is for instance the general Lennard-Jones potential.

$$V(r) = \frac{\lambda_n}{r^n} - \frac{\lambda_m}{r^m} \quad (2.17)$$

The most commonly used form is the Lennard-Jones (6-12) potential with  $n=12$  and  $m=6$ . However, for an ionic solid a more fundamentally based model would be the potential as given by equation 2.18,

$$V = V_{\text{att}} + V_{\text{rep}} = -\frac{\alpha e^2}{4\pi\epsilon_0 r} + \lambda e^{-r/\rho}. \quad (2.18)$$

The attractive potential is the Coulomb interaction whereas the repulsive potential is maintained by the Pauli exclusion principle based on the overlap of the electronic wave functions. For a general anharmonic potential  $V$  rises more slowly for  $r > r_0$ . In effect the atomic oscillations induced by temperature will lead to a shift of the average position (probability density of the atom location) of the atoms to larger  $r$ , hence the thermal expansion is described qualitatively. This effect is shown in figure 2.1. However, this model cannot explain the phenomenon of negative thermal expansion which is known to exist in a number of compounds. For that purpose one has to look at the transversal oscillations, in which the atoms move perpendicular to the tie line. This gives rise to a mechanism pulling the atoms towards each other thereby decreasing the distance between the atoms. [74]

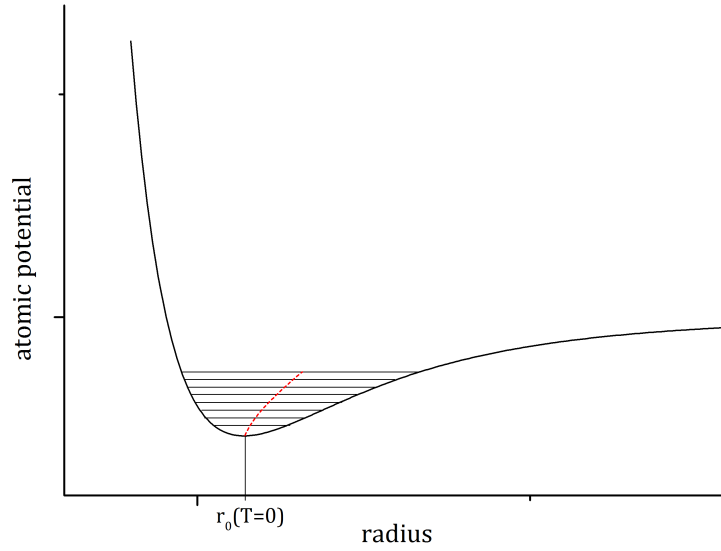


Figure 2.1: An anharmonic potential is shown with the tie lines representing energy levels corresponding to excitations due to elevated temperatures. The red dotted line indicates the shift of the average position of the atom in dependence of the successively increasing excitation and provides a conceptual description of thermal expansion.

### 2.4.3 Lattice dynamics

Lattice dynamics are a fundamental part of solid state physics and describes the temperature effects on the atomic motion in the periodic lattice of a crystalline compound. In general, when temperature increases, the solid compound absorbs the energy, leading to an increase of its internal energy  $U$ . A major fraction of this energy is consumed by atomic excitations in the form of motion (phonons). The other fractions are of electronic and

magnetic nature. The formula according to equation 2.19 describes the different fractions with  $E_{\text{static}}$  being the energy of the static lattice,  $E_{\text{elec}}$  the electronic energy,  $E_{\text{mag}}$  the magnetic energy and  $E_{\text{phon}}$  the phonon energy.

$$U = E_{\text{static}} + E_{\text{elec}} + E_{\text{mag}} + E_{\text{phon}} \quad (2.19)$$

Focussing on the lattice vibrations, called phonons, with increasing temperature, more and more phonons are excited and increase in amplitude. In essence, the heat work done on the compound is mainly transformed into kinetic energy of the atoms or ions. It has been observed for simple solids that at high temperatures the heat capacities reach the limit of  $3R$  ( $R$ : gas constant), which is called the Dulong-Petit limit. It is derived from the equipartition theorem, which basically states that the energy is distributed evenly among all atoms and all degrees of freedom. The degrees of freedom are translations in x, y and z direction as well as vibrations along the x, y and z axis. For each degree of freedom an energy of  $kT/2$  has to be accounted for, which ultimately adds up to a total of  $3kT$  per atom or  $3kTN_A$  per mole. By using the definition in equation 2.20 one obtains  $3kN_A=24.96 \text{ Jmole}^{-1}\text{K}^{-1}$  as the Dulong-Petit limit for the heat capacity,

$$C_V = \frac{\partial U}{\partial T}. \quad (2.20)$$

Experimentalists usually refer to the heat capacity at constant pressure  $C_P$  which is simply owed to the conditions under which the measurements are carried out. Technically, it is much more convenient to do heat capacity measurements at constant pressure allowing the sample to expand or contract upon temperature change instead of constraining the sample to maintain its volume. The thermal expansion is a direct consequence of the anharmonicity of the atomic potentials as described in chapter 2.4.2. Therefore, in a

perfectly harmonic solid, the heat capacity at constant pressure would be identical to the heat capacity at constant volume due to the absence of thermal expansion.

The Dulong-Petit law is not able to explain the temperature-dependence of the heat capacity. More sophisticated models are presented in the next sections. Basically, regarding the atoms in a solid as a lattice of interconnected oscillators illustrates the principle well. Thermal energy can excite the lattice to perform vibrations along certain directions of the structure and in different modes. Firstly, one distinguishes between longitudinal and transversal modes. In longitudinal mode the atoms oscillate parallel to the propagation direction of the wave whereas in transversal mode they oscillate perpendicular to the propagation direction. Secondly, there are acoustic modes and optical modes. Acoustic modes possess the characteristics of sound waves propagation through a medium whereas optical modes have neighbouring atoms moving in anti-phase to each other. They are called optical modes since they can be excited by electromagnetic waves. There are always 2 transversal modes and 1 longitudinal mode. The remaining ones are all optical. The total number of possible modes in a solid containing  $N$  atoms is  $3N$  since each atom can oscillate in 3 directions of the Cartesian coordinate system. Consequently, the total number of optical modes is  $3N-3$ . At 0 K all modes are frozen except for the zero-point vibrations. Successively increasing temperature leads to the excitation of one mode after the other.

### **The Bose-Einstein distribution**

The Bose-Einstein distribution is the energy distribution function of bosons, i.e. quasi-particles without angular momentum like photons and phonons as opposed to electrons. The Bose-Einstein distribution differs from the Fermi-Dirac distribution for electrons due to the fact that electrons obey the Pauli exclusion principle by which the same quantum state can never be occupied by more than one electron at once. Bosons do not obey this rule meaning

that an arbitrary number of bosons can occupy the same quantum state. For the Bose-Einstein distribution one assumes the energy states to be described by a harmonic oscillator with  $E_n = \hbar\omega(n + \frac{1}{2})$ . The probability of having a particle of energy  $E_n$  is given by the equation 2.21.

$$P_n = \frac{1}{Z} e^{-\frac{E_n}{k_B T}} = \frac{1}{Z} e^{-\frac{1}{k_B T} \hbar\omega(n + \frac{1}{2})}. \quad (2.21)$$

$Z$  is the normalisation factor and has the following form:

$$Z = \sum_{n=0}^{\infty} e^{-\frac{E_n}{k_B T}} = \sum_{n=0}^{\infty} e^{-\frac{1}{k_B T} \hbar\omega(n + \frac{1}{2})}.$$

The average occupation number for a boson  $\langle n \rangle$  is given by

$$\langle n \rangle = \sum_{n=0}^{\infty} n \cdot P_n = \frac{1}{Z} \sum_{n=0}^{\infty} n e^{-\frac{1}{k_B T} \hbar\omega(n + \frac{1}{2})}.$$

This can be transformed to:

$$\langle n \rangle = \frac{e^{-\frac{\hbar\omega}{2k_B T}}}{Z} \sum_{n=0}^{\infty} n \cdot e^{-\frac{\hbar\omega n}{k_B T}} = \frac{e^{\frac{x}{2}}}{Z} \frac{d}{dx} \sum_{n=0}^{\infty} e^{xn},$$

with  $x = -\frac{\hbar\omega}{k_B T}$ .

The expression in the sum is an infinite geometric series and can be expressed as  $\sum_{n=0}^{\infty} e^{xn} = \frac{1}{1-e^x}$ . With  $|e^{-\frac{\hbar\omega}{k_B T}}| < 1$  the expression can be transformed to:

$$\langle n \rangle = \frac{1}{e^{-\frac{\hbar\omega}{k_B T}} - 1}, \quad (2.22)$$

which is the Bose-Einstein-distribution.

### The Debye Model

The Debye model is a common model to describe the heat capacity of a solid compound. It is accurate for the high-temperature limit, where it recovers the Dulong-Petit limit, and describes the low temperature range qualitatively correctly. Its foundation is the derivation of the Debye frequency or Debye temperature in the reciprocal space. For that purpose a crystal consisting of  $N$  atoms is considered with equal dimensions in  $x$ ,  $y$  and  $z$  direction. Furthermore it is assumed that each  $q$ -vector occupies the same volume in reciprocal space of  $(2\pi/L)^3 = 8\pi^3/V$ .

Since the vibrational frequencies are limited by the distance between the atoms there is an upper cutoff-frequency, which is termed Debye frequency  $\omega_D$  with the relation:

$$q_D = \omega_D/v_s, \quad (2.23)$$

where  $q_D$  is the wave number and  $v_s$  the velocity of wave propagation at the Debye frequency.

With the further assumption that all wave vectors are excited up to the Debye frequency the total number of phonon modes can be expressed as follow:

$$N = \left(\frac{4}{3}\pi q_D^3\right) / \left(\frac{8\pi^3}{V}\right).$$

Then the Debye frequency can be written as  $\omega_D = v_s(6\pi^2 \frac{N}{V})^{1/3}$  and the Debye temperature is derived as:

$$T_D = \frac{\hbar\omega_D}{k_B} = \frac{\hbar v_s}{k_B} (6\pi^2 \frac{N}{V})^{1/3}.$$

The specific heat within the Debye model (equation 2.24) is obtained by integrating the product of density of states, Bose-Einstein distribution-function

(equation 2.22) over the frequency with the Debye frequency as the upper limit to yield the internal energy and deriving the function with respect to temperature:

$$U = \int d\omega D(\omega)n(\omega)\hbar\omega = \int_0^{\omega_D} d\omega \frac{V\omega^2}{2\pi^2v_s^3} \frac{\hbar\omega}{e^{\hbar\omega/k_B T} - 1},$$

$$C_V = \frac{\partial U}{\partial T} \Rightarrow C_V = 9Nk_B \left(\frac{T}{T_D}\right)^3 \int_0^{x_D} dx \frac{x^4 e^x}{(e^x - 1)^2}, \quad (2.24)$$

with  $x = \hbar\omega/k_B T$  and  $x_D = T_D/T$ .

# Chapter 3

## Ab initio computation

Ab initio computation is founded on the principles of quantum-mechanics. As such a method the classical description of electrons as a particle is replaced by the quantum-mechanical treatment, in which the electrons are described by a wave function. Their energy is determined by the wave length whereas the location cannot be given exactly any more but instead in terms of a probability density distribution. In ab initio computation the main equation to solve is the Schrödinger equation.

Ab initio methods can be divided into two classes: the wave function methods and the density functional methods. In wave function methods the target quantity is the electron wave function whereas for DFT methods it is the electron density. Solving the Schrödinger equation in terms of the wave function is computationally much more expensive than solving it for a given electron density distribution. Given a system with  $n$  electrons the wave function to solve would depend on  $3n$  spatial coordinates whereas if choosing the density as the target property the solution would solely have to be found in dependence of the 3 spatial coordinates. In any case, as will be described in the following section, it was proven that obtaining ground state properties does not necessitate the knowledge of the exact wave function but only the electron density. Consequently, the DFT has become the dominant method

in ab initio computation.

### 3.1 The basics about Density Functional Theory

DFT provides the conceptual framework on which all available codes are based on. The methods developed in the first part of the 20th century were incorporated into powerful computational programs such as the Vienna ab-initio simulation package (VASP), the Cambridge serial total energy package (CASTEP) and Quantum Espresso, with which nowadays it is possible to calculate molecular and condensed matter properties derived from the calculated ground states. The versatility of this method lies in the fact that, in principal, no experimental input is needed except for information on the crystal structure. Once this information is known a wide range of properties like thermodynamic, mechanical, electrical and magnetic properties can be calculated. Nevertheless it still requires careful and elaborate considerations in the process of setting up the calculations in order to acquire sensible information, which provides adequate physical results.

The first part of the theory is the so-called Hohenberg-Kohn theorem, which states that the energy of an  $n$ -electron system is determined uniquely by its electron density distribution.

In other words, knowing the ground state electron density distribution makes it possible to determine the corresponding ground state wave function and therefore to derive the ground state properties.

$$\rho_0(x) = |\Psi_0|^2 \tag{3.1}$$

However, the Hohenberg-Kohn theorem is only an existence theorem, which signifies that it does not provide the means to map the electron density onto

the electron wave function. It only states that this mapping exists. The second part of the theory states that minimizing the energy as a function of the electron density will converge to the ground state energy and thereby to the ground state electron density distribution as well. Due to equation 3.1 the wave function itself is also part of the calculation procedure when running DFT calculations. The general algorithm is called self-consistent field (SCF) method and will be explained in more detail later.

As outlined in section 2.3 the Schrödinger equation is only solvable for a one-electron system. When going to n-electron systems solving the Schrödinger equation becomes computationally intractable due to the n electrons all interacting with each other. Therefore, before DFT methods could actually become useful in practice, a way of treating n-electron systems had to be devised beforehand. This way was provided by the Kohn-Sham ansatz, which treats the system of n interacting electrons in a static external potential as a system of n non-interacting electrons in an effective potential. In other words, the density functional of an n-electron system is written as a fictitious density functional with a set of one-electron systems.

$$E_{\text{eff}}[\rho] = \langle \Psi_{\text{eff}}[\rho] | T_{\text{eff}} + V_{\text{eff}} | \Psi_{\text{eff}}[\rho] \rangle \quad (3.2)$$

In equation 3.2  $T_{\text{eff}}$  denotes the noninteracting electrons' kinetic energy and  $V_{\text{eff}}$  is an external effective potential in which the electrons are moving. It is assumed that the fictitious model system has the same energy as the real system. The effective potential is written as the sum of the potential of the interacting electron system, the so-called Hartree term (electron-electron Coulomb repulsion) and the exchange-correlation potential  $V_{XC}$  (equation 3.3) which includes all the many-electron interactions.

$$V_{\text{eff}} = V + \int \frac{\rho_{\text{eff}}(r')}{|r - r'|} d^3r' + V_{XC}[\rho_{\text{eff}}(r)] \quad (3.3)$$

Since this term can not be calculated and is hence unknown, equation 3.3 is only exact as a formalism. But certain approximations exist allowing the calculation of real systems (section 3.3).

The resulting effective Hamiltonian is given by the following equation:

$$H_{\text{eff}} = \sum_{i=1}^N \left[ -\frac{1}{2} \Delta_i + V_{\text{eff}}(r_i) \right] = \sum_{i=1}^N h_{\text{eff}}(r_i) \quad (3.4)$$

The above equation basically yields the orbitals  $\rho_i(r)$  that reproduce the density  $\rho(r)$  of the original many electron system. For each single-particle orbital the equation 3.5 has to be solved:

$$h_{\text{eff}} \rho_i = \epsilon \rho_i \quad (3.5)$$

The above equations are the Kohn-Sham equations in which both the Hartree term and the exchange-correlation potential depend on  $\rho(r)$ , which in turn depends on the densities of the individual orbitals  $\rho_i$ . These depend on  $V_{\text{eff}}$  again so that the Kohn-Sham equations are only solvable through an iterative self-consistent way. Normally the procedure starts with an initial guess for the electron density, then the effective potential is calculated. Then the Kohn-Sham equations are solved (equation 3.2) yielding the energy eigenvalue of the system and a new set of electron densities. The whole procedure is iterated until convergence is reached, i.e. the difference between the energies of two subsequent iterations drops below a specified threshold. Figure 3.1 displays the workflow of a typical DFT code. To calculate the equilibrium crystal structure the ionic positions are shifted after each SCF loop whereas the new coordinates are derived according to a specified algorithm. During each SCF loop the positions of the atomic nuclei are considered stationary. This decoupled treatment of the electrons and the atomic cores is essential for the algorithm and only possible since the atoms have a much higher mass than the electrons. Due to the much smaller mass of the electrons

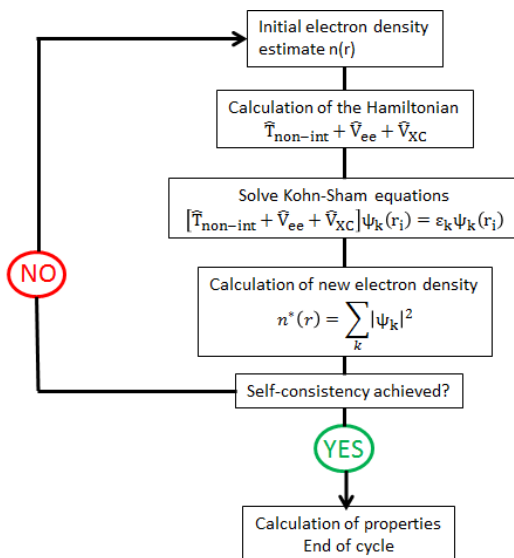


Figure 3.1: The Self-consistent-field method

the time-scale of their motion is orders of magnitude lower and relax almost instantaneously to their ground-state configuration in response to a change in position of the atomic nuclei (Born-Oppenheimer approximation). All DFT codes come with a huge library consisting of atomic potentials for each chemical element of the periodic system, which supply information about the number of electrons and the electron configuration, i.e. how the electrons are distributed among the orbitals.

## 3.2 Spin in DFT

In the classical form of DFT electronic spin is not taken into account since the energy and the potential are only a functional of the electron density. So to account for the electronic spin the electron density has to be explicitly

written as the sum of two different spin densities,  $n_{\uparrow}(r)$  and  $n_{\downarrow}(r)$ , that the electrons can take on.

$$n(r) = n_{\uparrow}(r) + n_{\downarrow}(r) = \sum_s n_s(r) \quad (3.6)$$

Then the exchange-correlation functional is also a functional of  $n_{\uparrow}(r)$  and  $n_{\downarrow}(r)$ :

$$E_{\text{XC}} = E_{\text{XC}}[n_{\uparrow}, n_{\downarrow}] \quad (3.7)$$

The Kohn-Sham-equations can then be written as:

$$\left[ -\frac{\hbar^2}{2m_e} \nabla^2 + V_{\text{eff}}^s(r) \right] \Psi_s(r) = E_s \Psi_s(r) \quad (3.8)$$

with  $s=\pm 1$ .

### 3.3 The exchange functional

As mentioned before the exchange-correlation functional is the remaining unknown term of the Kohn-Sham-equation (equation 3.2). A separation into exchange and correlation parts is not well defined. Nevertheless, in practice it is divided into 2 parts, the exchange-functional and the correlation-functional:

$$E_{\text{XC}}[\rho] = E_X[\rho] + E_C[\rho] \quad (3.9)$$

The exchange functional is in principle exactly known for a homogeneous electron gas, but involves the calculation of computationally expensive integrals. However, in contrast, there exists no analogous expression for the correlation functional in terms of accuracy. Since the accuracy is determined by the least accurate term the exchange and the correlation functional have to be matched in terms of accuracy.

The most commonly used exchange-correlation functionals can be divided

into 2 groups: the local density approximation (LDA)- and the general gradient approximation (GGA)-functionals. The LDA-functionals (equation 3.10) are based on the assumption that a general inhomogeneous electron system is locally homogeneous. The energy of the whole system is calculated by integrating the locally homogeneous densities multiplied with the energy density  $\epsilon_{\text{XC}}^{\text{LDA}}[\rho(r)]$  over the whole volume.

$$E_{\text{XC}}^{\text{LDA}}[\rho] = \int \rho(r) \epsilon_{\text{XC}}^{\text{LDA}}[\rho(r)] dr \quad (3.10)$$

The GGA-functional is one of the results obtained from a variety of different attempts to improve the predictive capabilities of the LDA-functional. The fundamental basis for the GGA-functionals is the so-called gradient expansion, which is essentially an expansion of the exchange-correlation energy functional as a series in terms of the density and its gradients (equation 3.11). In this manner inhomogeneities of the density are included. [75]

$$E_{\text{XC}}^{\text{GGA}}[\rho] = \int \rho(r) \epsilon_{\text{XC}}[\rho(r)] F_{\text{XC}}[\rho(r), \nabla\rho(r), \nabla^2\rho(r), \dots] dr \quad (3.11)$$

A variety of different parametrizations for the functionals exist among which most are adapted to reproduce experimental data for specific systems.

## 3.4 Treating strongly correlated systems within DFT

DFT is known to yield reasonable results for metals since the behaviour of electrons in metals resembling a free electron gas is treated well within the classic exchange functionals as LDA and GGA. However, for materials containing transition metals the prediction of properties usually fails within the classical GGA approximation. This is due to the fact that transition metals contain d-electrons which are much more localised than the electrons in a metallic system whereas the LDA- and GGA-functionals represent one-electron delocalized exchange functionals (as is based on the simplifications of the DFT). Consequently, within LDA or GGA exchange functionals the d-bands are modelled as being partially filled with-non-localized electrons hereby incorporating the physical behaviour of a metal. Often this results in the prediction of metallic properties for compounds which are actually insulators or semiconductors [76]. To account for the more localised nature of the electrons in the d-shell a common approach is to add a Coulomb repulsion term on the d-orbitals so as to decrease the tendency of these electrons to delocalise to the other d-orbitals. This is called the on-site Coulomb repulsion  $U$ . Figure 3.2 illustrates this concept. This idea is condensed in the so-called Hubbard-U model (equation 3.12).

$$\hat{H} = -t \sum_{i\sigma} \left( c_{i\sigma}^\dagger c_{i+1\sigma} + c_{i+1\sigma}^\dagger c_{i\sigma} \right) + U \sum_i n_{i\downarrow} n_{i\uparrow} \quad (3.12)$$

$t$  is the kinetic term (also designated transfer integral) which describes the electronic motion between atomic sites and is usually restricted to nearest neighbouring sites.  $n$  is the ratio between the number of electrons  $N$  and the number of sites  $N_\alpha$  ( $n = \frac{N}{N_\alpha}$ ).  $c_{i\sigma}^\dagger$  and  $c_{i\sigma}$  are the creation and annihilation operators of an electron of spin  $\sigma$  at site  $i$ . In the case of  $U=0$  the Hamiltonian corresponds to a system of  $N$  non-interacting electrons moving in a band of

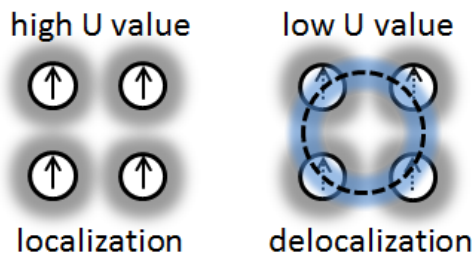


Figure 3.2: Effect of the Hubbard  $U$  parameter on the electron behaviour: a low  $U$  value decreases the Coulomb repulsion between electrons in the same orbital. Consequently, the electrons can delocalize, which resembles a metallic behaviour. A high  $U$  value has the opposite effect.

width  $W = 2zt$  with  $z$  the coordination number. On the other hand when  $U \gg t$  the electronic motion becomes increasingly suppressed due to the penalization of the energy of doubly occupied sites. In the simple case of  $n = 1$  this would translate into singly occupied sites with anti-ferromagnetic ordering of the electronic spins [77]. This suggests that halfway between these 2 cases there is a metal-insulator transition.

The drawback of this model is that the  $U$ -value is unknown and needs to be optimized to reproduce the experimental properties. The  $U$ -value may vary even among compounds within the same family of structures. What is more, in many cases a specific  $U$ -value can reproduce one property but not a second property at the same time. Therefore, if applying this approach great care has to be taken with respect to the problem to be investigated.

### 3.5 The pseudopotential and PAW method

According to Blochs' theorem (section 2.3.1 equation 2.9) electrons in a periodic solid can be conveniently described in terms of plane waves. A complete basis set for the construction of the electron wave functions can be obtained by developing a Fourier series with which the electron wave functions are expanded into a series of plane waves.

$$\Psi_{i,k}(r) = \sum_{|G| < G_{\max}} c_{ik,G} e^{i(k+G)\cdot r} \quad (3.13)$$

with  $c_{ik,G}$  the Fourier coefficients,  $G$  denoting the reciprocal lattice vectors and  $k$  an arbitrary vector in reciprocal space. The formalism is exact in the limit of an infinite number of plane waves. However, in practice the infinite sum is not necessary. The kinetic term of the Hamiltonian is proportional to the square of the wave vector, hence, states with high  $|G + k|$  have a high kinetic energy. Above a specific limit depending on the chemical species present in the structure  $|G + k|$  will be so high that the Fourier coefficients are negligible and the series can be truncated. The standard truncation criterion

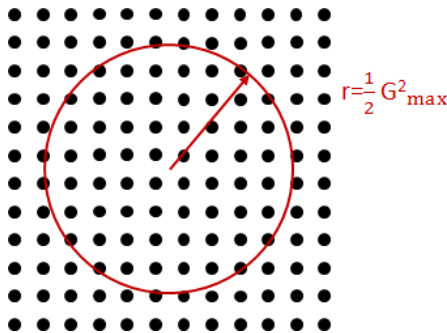


Figure 3.3: Schematic representation of the energy cutoff in the reciprocal lattice

is:  $E_{\text{cut}} = \frac{1}{2}G_{\max}^2$ . This corresponds to a sphere in reciprocal space with the

radius  $r = E_{\text{cut}}$  as shown in figure 3.3. However, DFT calculations with basis sets solely based on plane waves are highly inefficient. The main reason is attributed to the nature of the atomic core charge inducing a deep Coulomb potential, which causes the electron wave function to oscillate rapidly close to the atomic core. To represent the electron wave function in terms of plane waves this would necessitate plane waves up to very high kinetic energies. This requires large computational resources and cannot be carried out in a feasible manner. Therefore this imposes an obstacle for the implementation of calculation algorithms for DFT-codes. However, if the expansion series were to be truncated at a certain energy level (energy cutoff) the problem would be tractable. In order to be able to take advantage of the truncation the atomic

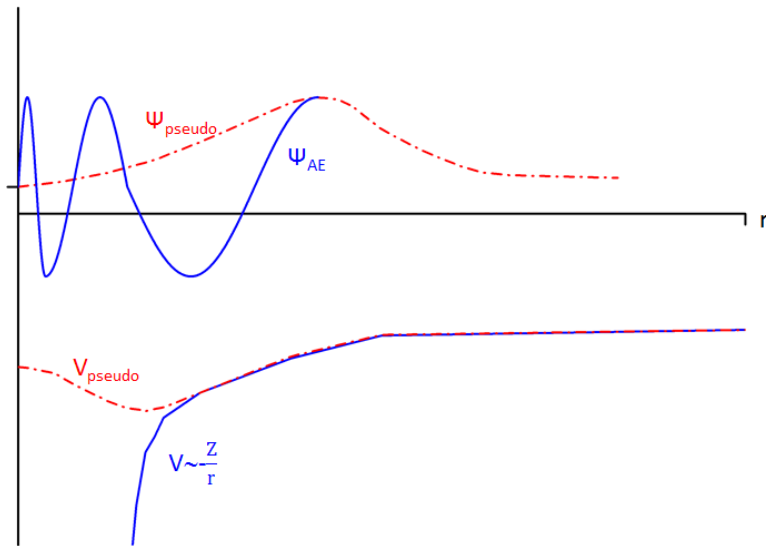


Figure 3.4: Illustration of the pseudopotential and the pseudo-electron wave function

core potential has to be modified to avoid the high kinetic energy of the electrons in the vicinity of the atomic core. [78] This is done by introducing pseudo-potentials, which basically replace the atomic core potential. That is

in many cases a legit approach since the electrons at the core levels usually do not take part in chemical bonding and reactions. Since the exact atomic potential is only replaced by a pseudo-potential at the core the description of the valence electrons remains accurate and the system is solved for only the valence electrons, which require less plane waves. This is illustrated in figure 3.4.

However some properties which do depend on the core electrons may not be reproduced in this fashion. Moreover for transition metals the 3d electrons cannot be treated as part of the core without losing their specific properties. But these are very local orbitals and therefore need a very large basis set to converge. Consequently other methods had to be developed resulting in the projector-augmented wave (PAW) method, which extends the idea of the original pseudopotentials. Space is partitioned into 2 regions: a spherical one surrounding the atom and an interstitial one. The wave functions in the spherical region and the interstitial regions are expanded separately in order to be able to reproduce the nodes within the spherical region without having to use the same basis set in the interstitial region. This way the all-electron information is retained without losing the computational efficiency of the pseudopotential. [79, 80] The PAW method is implemented in VASP.

## 3.6 Brillouin zone integration

To calculate the Kohn-Sham eigenvalues of a DFT structure or the electron density an integration of the observables in the Brillouin zone (BZ) is necessary.

$$E_{\text{tot}} = \frac{1}{V_{BZ}} \int_{1.BZ} E(k) d^3k \quad (3.14)$$
$$\text{with } n(r) = \frac{1}{V_{BZ}} n_k(r) d^3k$$

However, in numerical practice these integrals have to be converted into sums over discrete k-points in reciprocal space. As for all numerical methods the issue of convergence is of vital importance. In this specific case that is the convergence of the calculated sums with respect to the number of k points. The established way of choosing k-points is to generate a uniform grid of k-points in the irreducible BZ according to Monkhorst and Pack. To do so properly the crystal shape has to be considered since the dimensions of the lattice parameters determines the reciprocal lattice parameters, hence the three dimensions of the irreducible BZ. If the BZ has a larger dimension in one direction this has to be accounted for by placing more k points along that direction to maintain the same k-point density in all locations of the irreducible BZ. Before running data production jobs on a larger scale it has to be ensured that the total energies of the calculations have converged with respect to the number of k-points. [78]

## 3.7 Phonon calculations

The total energies obtained via a DFT code are always with respect to 0 K since the atoms are motionless. In order to be able to obtain the energies for finite temperatures it is necessary to incorporate the quantized lattice vibrations, also called phonons. These are ultimately the atomistic cause for the material property "heat capacity". The basic approach to calculate the lattice dynamics within the DFT framework is to calculate the force constants, i.e. the first derivative of the forces with respect to atomic displacements away from their equilibrium positions, that draw them back to the energetically local or global minimum. Within the model of treating atoms as oscillators the calculated force constants (derivative of the forces with respect to displacement) allow to yield the eigenfrequencies of each particular atomic oscillator in all their respective possible modes (k-vectors). The equation that relates the eigenfrequencies and the force constants to each other was shown in section 2.4.1 (equation 2.16). In principle, when holding the complete frequency spectrum it is possible to compute thermal properties as average values from the so-called phonon partition function, a statistical representation of the excited phonons in dependence of the temperature.

Basically, one distinguishes between two methods which are both described since both are employed in this work:

1. Finite difference method
2. Linear response method

### 3.7.1 Finite difference method

The finite difference method is an approach in which the force constants are computed by calculating the forces of systematically generated structures with distinct atomic displacements and computing the ratio between the force differences and the absolute displacements. This is formalized in equation 3.15

$$k = \frac{\partial^2 E_{\text{pot}}(R)}{\partial u^2} \cong -\frac{F(R + \Delta u) - F(R)}{\Delta u} \quad (3.15)$$

$F$  is the force,  $R$  the equilibrium coordinates,  $\Delta u$  the displacement  $E_{\text{pot}}$  the energy and  $k$  the force constant. In the limit of infinitesimal small displacements the fraction attains the mathematical expression of the 2nd derivative of the energy (Hessian) with respect to the displacement and represents a numerical approximation for calculating the force constant.

The major advantage of this approach that it is easy to implement since it is only necessary to pre-process the equilibrium structure to generate displaced structures and post-process the obtained data. Codes can be and are developed modularly to accommodate the demands. One major drawback is that the supercell has to be chosen sufficiently large in order to reach convergence with respect to the supercell size which is due to interactions with atoms/ions from the neighbouring cell originating from the periodic boundary conditions. Moreover, it is not possible to evaluate the Born charges on the longitudinal optical modes near gamma point, which can have significant effects on the thermal properties. Born charges refer to the phenomenon of induced dipoles in ionic compounds caused by displacements of the ions from their equilibrium positions. Since these exert an additional force, the resulting force constants can be affected.

### 3.7.2 Linear response method

The linear response method, a method based on the density functional perturbation theory, evaluates the Hessian in response to an external ionic perturbation in a self-consistent way. This is made possible since density functional perturbation theory states an analytical method to calculate this:

$$\begin{aligned} \frac{\partial^2 E(R)}{\partial R_I \partial R_J} &= -\frac{\partial F_I}{\partial R_J} \\ &= \int \frac{\partial n_R(r)}{\partial R_I} \frac{\partial V_R(r)}{\partial R_J} \partial r + \int n_R(r) \frac{\partial^2 V_R(r)}{\partial R_I \partial R_J} \partial r + \frac{\partial^2 E_N(R)}{\partial R_I \partial R_J} \end{aligned} \quad (3.16)$$

$R_{I/J}$  is the coordinate of the Ith/Jth nucleus,  $V_R(r)$  is the electron-nucleus interaction and  $E_N(R)$  is the electrostatic interaction between different nuclei.

In essence the force constants are obtained directly by using the ground state electron charge density and calculating its linear response to a perturbation of the nuclear geometry.

The major advantage of this approach is that Born-charge effects can be easily dealt with and that basically it is not necessary to use supercells to run the calculations. However, in the VASP code only Gamma point calculations are implemented for the linear response method, which in return does necessitate the use of supercells to obtain accurate results. Another drawback of this method in VASP is the fact that the linear response calculations cannot be started with the wave functions of the precedent relaxation. This can be problematic in case of spin-polarized calculations because the optimization of the wave functions before the starting of the linear response can converge to a different spin-state and ultimately leads to errors in the force constants.

### 3.7.3 Harmonic phonon calculations

The phonon number is proportional to the temperature and is given by equation 3.17:

$$n = \frac{1}{\exp(\hbar\omega(q\nu)/k_B T) - 1} \quad (3.17)$$

The harmonic phonon free energy is calculated via the product of the phonon number and the energy of a quantum oscillator as shown in equation 3.18. It can be seen from the factor The addition term  $\frac{1}{2}$  additionally takes the zero point energy into account.

$$E = \sum_{q\nu} \hbar\omega(q\nu) \left[ \frac{1}{2} + \frac{1}{\exp(\hbar\omega(q\nu)/k_B T) - 1} \right] \quad (3.18)$$

Then the heat capacity at constant volume is derived by deriving equation 3.18 with respect to temperature T. To be exact, it would have to be the internal energy U to be derived with respect to T since the phonon free energy is only the major fraction of the internal energy as already shown in chapter 2.4.3. But when specifically calculating the lattice dynamics (phonons) the remaining fractions are simply not accounted for within this formalism. Therefore the phonon free energy is taken as the internal energy and  $C_V$  arises exclusively from the phonon energy intake:

$$C_V = \left( \frac{\partial E}{\partial T} \right)_V = \sum_{q\nu} k_B \left( \frac{\hbar(q\nu)}{k_B T} \right)^2 \frac{\exp(\hbar\omega(q\nu)/k_B T)}{[\exp(\hbar\omega(q\nu)/k_B T) - 1]^2} \quad (3.19)$$

The Helmholtz free energy F and the vibrational entropy are derived from the phonon partition function Z:

$$Z = \exp(-\phi/k_B T) \prod_{q\nu} \frac{\exp(-\hbar\omega(q\nu)/2k_B T)}{1 - \exp(-\hbar\omega(q\nu)/k_B T)} \quad (3.20)$$

$$\begin{aligned}
F &= -k_B T \ln Z \\
&= \phi + \frac{1}{2} \sum_{q\nu} \hbar\omega(q\nu) + k_B T \sum_{q\nu} \ln [1 - \exp(-\hbar\omega(q\nu)/k_B T)] \quad (3.21)
\end{aligned}$$

$$S = \frac{dZ}{dT} = \frac{1}{2T} \sum_{q\nu} \hbar\omega(q\nu) \coth(\hbar\omega(q\nu)/2k_B T) \quad (3.22)$$

$$- k_B \sum_{q\nu} \ln [2 \sinh(\hbar\omega(q\nu)/2k_B T)] \quad (3.23)$$

### 3.7.4 The quasi-harmonic approximation

The quasi-harmonic approximation (QHA) is a method to include the thermal expansion into the calculations, which are otherwise completely neglected since the calculations are exclusively calculated at constant volume. The harmonic approximation is only accurate for low temperatures where the atoms are only displaced slightly from their equilibrium position. Moreover, in the harmonic approximation one always obtains the constant volume thermal properties, which is rather inconvenient if to compare with experimental values. These are usually obtained at constant pressure. By calculating the harmonic vibrational spectrum in an iterative procedure (see figure A2.2 in chapter A) at different fixed volumes of the compound to both sides of the equilibrium volume a mapping of the vibrational free energy onto the volume can be done and the Helmholtz Free energy is obtained as a function of volume at specified temperatures. For each temperature an equation of state is fitted in  $F$  vs  $V$  with their own respective minima. The type of equation of state can vary depending on the implementation in different code packages or might be specified, but some of the most important ones were shown in section 2.2. From the curves interconnecting the minima the equilibrium volume for each temperature can be derived and the thermal expansion coefficient can be calculated. The bulk modulus is the second derivative of the free energy with respect to the volume (section 2.1). These two physical properties

are then incorporated into a correction term adding to the heat capacity at constant volume and resulting in the constant pressure heat capacity.

$$c_{p,m} - c_{v,m} = V_m(T)T \frac{\alpha(T)^2}{\beta_T(T)} = V_{f.u.} \cdot N_A \cdot T \frac{\alpha(T)^2}{\beta_T(T)} \quad (3.24)$$

The model is called "quasi"-harmonic since it is still solely based on the harmonic model but includes the thermal expansion in the explained manner. It neglects anharmonic effects of higher order, e.g. phonon-phonon coupling and electron-phonon coupling. Formally this is contained in the truncated Taylor expansion series of the total energy with respect to displacements  $u$ , which is valid for small  $|u|$  (equation 3.25). The second-order term is the one which is being calculated by evaluating the force constants, which are then related to the eigenfrequency of a harmonic oscillator as shown in equation 2.16. The first-order term vanishes due to the condition of a fully relaxed structure, for which all forces have diminished to zero.

$$E_{\text{tot}}(R_l u_l) = \sum_{I\alpha} \frac{p_{I\alpha}^2}{2M_I} + \sum_{I\alpha} \frac{\partial E_{\text{tot}}}{\partial u_{I\alpha}} u_{I\alpha} + \frac{1}{2} \sum_{I\alpha, J\beta} \frac{\partial^2 E_{\text{pot}}}{\partial u_{I\alpha} \partial u_{J\beta}} u_{I\alpha} u_{J\beta} \dots \quad (3.25)$$

These effects are responsible for the finite lifetime of the phonon excitations. Since they are not part of the QHA the calculated phonons have an infinite lifetime and the derived thermal properties may differ from the experimental values. However, these effects become significant in the limit of high temperatures meaning that for room-temperature applications the calculated results should be reliable in this respect. Discrepancies may still arise from the fact that the calculations are for a perfect ideal mono-crystalline compound with no defects.

## 3.8 Cluster expansion

When it comes to the modelling of systems in which two or more atomic species occupy the same lattice sites (substitutional solid solutions) one is faced with a combinatorial problem of a vast amount of possible atomic arrangements and the main question to answer is which of the atomic arrangements represent the ground state configuration with the lowest energy possible. In essence, when looking at a solid with  $N$  atomic sites which can be occupied by either the element A or B (whereas B can also be a vacancy) then the number of possible atomic arrangements is  $2^N$ . It would be a futile task to calculate the energies for all of these configurations. The so-called cluster expansion is a method to alleviate this problem by providing a formalism (equation 3.26) for enabling the prediction of the energies of an arbitrary configuration based on the knowledge of a finite set of configurations (structures). The formalism is based on a series expansion constructed from specific arrangements of two to four specific atoms in a range of crystal structures. These arrangements or figures within the crystal structures are called clusters. So the clusters can be doublets, triplets and quadruplets etc. They can be constituted of next neighbour atoms or of atoms separated by medium to longer distances (as exemplified in figure 3.5) depending on the size of the crystal structures which are successively generated in the process of this prediction algorithm. So depending on the structure at hand certain symmetry rules apply and the specific clusters have multiple equivalents within the structure. These multiplicities are counted and are an integral part of the expansion series. The last part of the expansion series are the occupation variables  $\sigma_i$ . They essentially represent how the lattice sites are occupied, whether site  $i$  is occupied by atom A or B. In the convention of an Ising model spin values of -1 and 1 are assigned to the sites occupied by A-atoms and B-atoms respectively as shown in figure 3.6. Each  $\sigma_i$  represents one lattice site  $i$  and therefore to describe the configuration of clusters one needs as many  $\sigma_i$ -values as there are lattice sites in the cluster. This

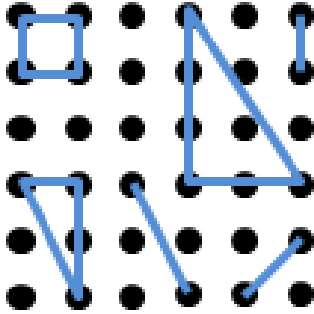


Figure 3.5: Some possible clusters on a 2-dimensional square lattice

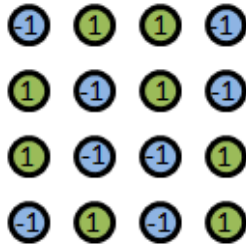


Figure 3.6: Binary alloy representation in the Cluster expansion formalism

is condensed in the product of  $\sigma_i$ -values, also called correlation functions, within the expansion series. If the cluster has symmetry equivalents then the products of the  $\sigma_i$  of all equivalent clusters are averaged as indicated by the angle brackets in equation 3.26.

$$E(\sigma) = \sum_{\alpha} m_{\alpha} J_{\alpha} \langle \prod_{i \in \alpha'} \sigma_i \rangle \quad (3.26)$$

### 3.8.1 The correlation function

The correlation functions are supposed to span the space of all possible configurations. To be able to represent the energy of all possible configurations with the Cluster expansion these correlation functions therefore need to form a complete basis set. It is possible to span the whole configurational space with different basis sets. The correlation functions are defined by the product of the occupation variables of the sites within a considered cluster. The correlation functions themselves are distinguished into point-, pair- and triple- etc. correlation functions to map the occupational state of figures with essentially arbitrary sizes. The point-correlation function would simply reflect the occupational state of a single site within a cluster. This is shown exemplarily for a binary A-B-alloy in equation 3.27.

$$f_A = \sigma_{iA} = \begin{cases} 1 & \text{if site is occupied by atom A} \\ 0 & \text{if site is occupied by atom B} \end{cases} \quad (3.27)$$

Whatever definition to distinguish the occupations can be applied without altering the outcome and accuracy of the cluster expansion as long as the selected basis set is complete. A pair-correlation function would be described as follows:

$$f_{AA} = \sigma_{iA}\sigma_{jA} = \begin{cases} 1 & \text{for alike neighbours} \\ 0 & \text{for unlike neighbours} \end{cases} \quad (3.28)$$

### 3.8.2 The Collony-Williams inversion

Given a binary A-B-alloy the expansion of the total energy for a sample of 3 structures (pure A, pure B and A:B=1:1) would conceptionally be looking as follows when taking point-correlation and pair-correlation functions into account:

$$\begin{aligned}
E_{\text{compound}} &= E_0 + f_A \cdot J_A + f_{AA} \cdot J_{AA}, & (3.29) \\
E_A &= E_0 + 1 \cdot J_A + 1 \cdot J_{AA}, \\
E_B &= E_0 + 0 \cdot J_A + 0 \cdot J_{AA}, \\
E_{AB} &= E_0 + \frac{1}{2} \cdot J_A + 0 \cdot J_{AA},
\end{aligned}$$

with the first line corresponding to the general form of the expansion for an arbitrary binary compound. In this context,  $E_0$  is the empty cluster term (an energy offset),  $J_A$  the point energy and  $J_{AA}$  the pair energy. In a pure B compound there would be no energy associated with sites occupied with A-type atoms, hence  $f_A = 0$ . The same can be said about a cluster of two sites ( $f_{AA} = 0$ ). For an A-B compound with equivalent amounts of A and B the next neighbours are never of the same atom type (assuming a NaCl-structure for this case). That is why  $f_{AA} = 0$ . The above system of linear equations is equivalent to the following matrix equation:

$$\begin{pmatrix} E_A \\ E_B \\ E_{AB} \end{pmatrix} = \begin{pmatrix} 1 & 1 & 1 \\ 1 & 0 & 0 \\ 1 & \frac{1}{2} & 0 \end{pmatrix} \begin{pmatrix} E_0 \\ J_A \\ J_{AA} \end{pmatrix} \quad (3.30)$$

The 3x3 matrix is the Sanchez-Connolly-Williams matrix (scwm). The effective cluster interaction parameters are therefore obtained by inverting the matrix with the correlation functions:

$$I = [\text{scwm}]^{-1} \cdot \bar{E} \quad (3.31)$$

More cluster interaction parameters can only be included in the expansion formalism if more structures are calculated to provide additional equations keeping the system of linear equations determined.

### 3.8.3 The quality of a cluster expansion

The quality of the fit by the expansion series is evaluated by means of the predictive power of the cluster expansion. A very common way to do so is to apply the so-called 'leave-one-out-cross-validation' (LOOCV). In this procedure the calculated energy of one single structure is excluded from the cluster expansion to evaluate the expansion-predicted energy of this specific structure compared to the calculated energy value. This is repeated for all other structures. If there are  $N$  calculated structures then  $\Delta E_i$  with  $i \in [1;N]$  are obtained which are then aligned according to the following formula:

$$\text{LOOCV} = \sqrt{\frac{1}{N} \sum^N \Delta E^2} \quad (3.32)$$

To sum up: the Cluster expansion formalism provides a method to express the energy of an alloy as an expansion series over symmetry distinct clusters and is exact when all possible atomic clusters are included. In practice, one makes use of the intuitive fact that with increasing distance between the atoms of the clusters the effective cluster interactions decrease to a negligible value. This allows the truncation of the expansion series after including only relatively small clusters and is the real power of the Cluster expansion formalism. However it still strongly depends on the system at hand how many structures are necessary to get converged expansion series.

# Chapter 4

## Modelling

### 4.1 Computational details

#### 4.1.1 The Metal-to-insulator transition

The projector-augmented wave potentials in the generalized gradient approximation as parametrized by Perdew-Burke-Enzerhof (GGA-PBE) are used [81] to run full-structure relaxations. A plane-wave energy cutoff of 520 eV is employed and the k-mesh has been varied to obtain convergence of 5 meV/atom for  $\text{LiCoO}_2$ . To explore different vacancy concentrations a 2x2x1 supercell of the rhombohedrally centered structure is used as a parent lattice whereas successive removal of lithium ions yields sufficient lithium sites to model the dilute stoichiometries. Configurations of clustered (close arrangements of vacancies) and distributed vacancies are probed. In order to account for both unoxidized  $\text{Co}^{3+}$  and oxidized  $\text{Co}^{4+}$  species two potential files of cobalt are supplied and are treated with disparate electronic spins by setting the MAGMOM-tag respectively. From the electron orbital configuration it can be expected that the  $\text{Co}^{3+}$  exhibits a low-spin state close to zero since all electrons are paired whereas  $\text{Co}^{4+}$  should exhibit a higher spin-state due to one unpaired electron. To be able to converge to different possible electron

configuration the electron spins are initialized in varying fashions. The obtained total energies are used to calculate the average intercalation voltage of  $\text{Li}_x\text{CoO}_2$  versus pure lithium. For the computation of the average intercalation voltage it is common to calculate the voltage with respect to lithium since its chemical potential remains constant over the whole reaction process independent of the amount of transferred lithium. Accordingly the change in free energy can be expressed as:

$$-\Delta G_r = - \int_{x_1}^{x_2} [\mu_{\text{Li}}^{\text{compound}}(x) - \mu_{\text{Li}}^0] dx_{\text{Li}} \quad (4.1)$$

$$= - [G_{\text{compound}}(x_2) - G_{\text{compound}}(x_1) - (x_2 - x_1) G_{\text{Li}}]. \quad (4.2)$$

For solid state reactions it can be assumed that volume changes  $\Delta V$  and entropy changes  $\Delta S$  are negligible so that

$$\Delta G = \Delta E + p\Delta V - T\Delta S = \Delta E. \quad (4.3)$$

Combining with equation 1.1 from section 1.3 the average intercalation voltage is obtained as follows:

$$\bar{V} = \frac{- [E_{\text{tot}}(\text{Li}_{x_2}\text{CoO}_2) - E_{\text{tot}}(\text{Li}_{x_1}\text{CoO}_2) - (x_2 - x_1) E_{\text{tot}}(\text{Li})]}{(x_2 - x_1) F}. \quad (4.4)$$

### 4.1.2 Calculating heat capacities for $\text{Li}_x\text{CoO}_2$

The same plane-wave energy cutoff and k-mesh as in the above section is employed. Due to the hexagonal symmetry of the lattice a Gamma centered k-mesh is employed. The resulting k-meshes are  $5 \times 5 \times 2$  for the supercell calculations. Full structure relaxation is carried out on the structures with forces converged to  $10^{-5}$  eV/Å with the exchange functional parametrized by Perdew-Burke-Ernzerhof GGA-PBE [81] and spin polarization is allowed to account for magnetism on cobalt. Both the impact of a Hubbard U term and Born-charge on the outcome is checked. In general, the finite difference method is applied to obtain the Hessian due to its lower computational cost. However, the Born effective charge tensors are not calculated within this algorithm in VASP. Consequently, to be able to investigate the Born-charge effects the linear response theory is employed as implemented in VASP. The Hubbard U term in the rotationally invariant form introduced by Dudarev et al. [82] is added on the Co d orbitals to account for the electron self-interaction. A value of 5.6 eV is assigned as has been calculated self-consistently by Juhin and de Groot [83]. In total, three discrete stoichiometries of the O3- $\text{Li}_x\text{CoO}_2$  are investigated:  $\text{LiCoO}_2$ ,  $\text{Li}_{0.67}\text{CoO}_2$  and  $\text{Li}_{0.5}\text{CoO}_2$ . In case of  $\text{Li}_{0.5}\text{CoO}_2$  two different vacancy arrangements are investigated, one for which a vacancy configuration is adopted which is analogous to the experimentally detected, monoclinically distorted structure but maintaining the O3-structure. The other structure (also O3- $\text{LiCoO}_2$ ) is constructed with an alternative vacancy arrangement. Both configurations are shown in the appendix B1. In all cases in this thesis the quasi-harmonic fit is done by employing the third order Birch-Murnaghan-EOS (equation 2.6) to get the parametrized  $E(V)$ -functions.

### 4.1.3 Cluster expansions on $\text{Li}_x\text{Mg}_2\text{Si}$

In the `lat.in` file the  $\text{Li}_x\text{Mg}_2\text{Si}$  crystal structure is provided in the primitive setting. The data is included in the appendix B2. The projector-augmented wave potentials in the generalized gradient approximation as parametrized by Perdew-Burke-Enzerhof are used [81]. A plane-wave energy cutoff of 320 eV is employed and the k-mesh was varied again to reach convergence of 5 meV/atom for the structures with the most extreme compositions of the respective cluster expansions. Whenever required by the crystal symmetry of the generated structures the k-mesh is set to a grid centred around the  $\Gamma$  (Gamma) point. The full structure relaxations are carried out with forces converged to  $10^{-2}$  eV/Å. About 170 structures in the concentration range of  $x \in [0;1]$  are calculated to get a sufficiently accurate parametrization of the energies for cell sizes up to 44 atoms. The total energies of a set of compositions are used to calculate the average intercalation voltage of the compounds versus pure lithium in the same manner as for the  $\text{Li}_x\text{CoO}_2$  system. Combining with equation 1.1 from section 1.3 the average intercalation voltage is obtained as follows:

$$\bar{V} = \frac{-[E_{\text{tot}}(\text{Li}_{x_2}\text{Mg}_2\text{Si}) - E_{\text{tot}}(\text{Li}_{x_1}\text{Mg}_2\text{Si}) - (x_2 - x_1) E_{\text{tot}}(\text{Li})]}{(x_2 - x_1) F}. \quad (4.5)$$

## 4.2 Results & discussion

### 4.2.1 Mapping the metal-to-insulator two-phase region

#### Aim

Due to deficiencies of the DFT method the two-phase equilibrium between the semiconducting and the metallic phase in the  $\text{Li}_x\text{CoO}_2$  solid solution has not been modelled yet. A multi-phase equilibrium manifests itself in a voltage plateau as dictated by the Gibbs phase rule. Thus, the ability to model such a transition would be beneficial for further investigations, e.g. in the direction of dopant effects on this two-phase equilibrium. In this section the results on the attempt to model the two-phase region between the semiconducting and the metallic phase in the  $\text{Li}_x\text{CoO}_2$  solid solution are discussed. To be able to capture the electronic properties related to the d orbitals of cobalt the Hubbard U model is employed accounting for the localized nature of its d electrons. To distinguish between Co(III) and Co(IV) two cobalt potentials were provided in the POTCAR file whereas the number of Co(IV) ions has to match the number of lithium vacancies in the respective supercells due to charge balancing. The aim is to converge to both metallic and semiconducting states by measures of the electronic DOS in a range of  $x \in [0.5; 1]$  and, subsequently, cross-referencing with the associated total energies in order to evaluate the energy devolution of both states.

#### Discussion

First, the sensitivity of the resulting band gap with respect to the chosen U-value is investigated by evaluating the resulting electron DOS for calculations with  $U=3.3, 4.9, 5.6$  and  $7$  eV. The increase of the U parameter from  $3.3$  eV to  $7$  eV causes an increase of the band gap by around  $1$  eV. Since the effect of the U parameter on the band gap is not that significant the U value of  $3.3$  eV is selected for all calculations. This specific value is adopted from the

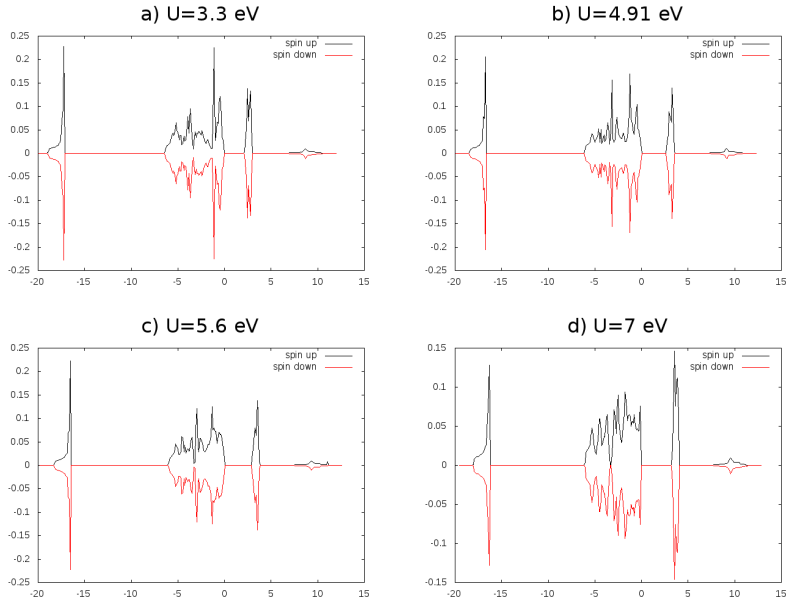


Figure 4.1: Electronic density of states in dependence of  $U$ -value obtained from spin-polarized calculations: band gaps range from 2.1 eV for  $U=3.3$  eV to 3.2 eV for  $U=7$  eV.

Materials project [84, 85], within which the  $U$  values have been optimized for the purpose of matching experimental enthalpies of formation.

In all cases the configurations with distributed vacancies led to lower energies. Regarding the transition from semiconductor to metal it can be observed that the electronic band gap decreases when lithium atoms are successively removed from the structure and eventually closes below a lithium content of  $x=0.77$  (see figure 4.2).

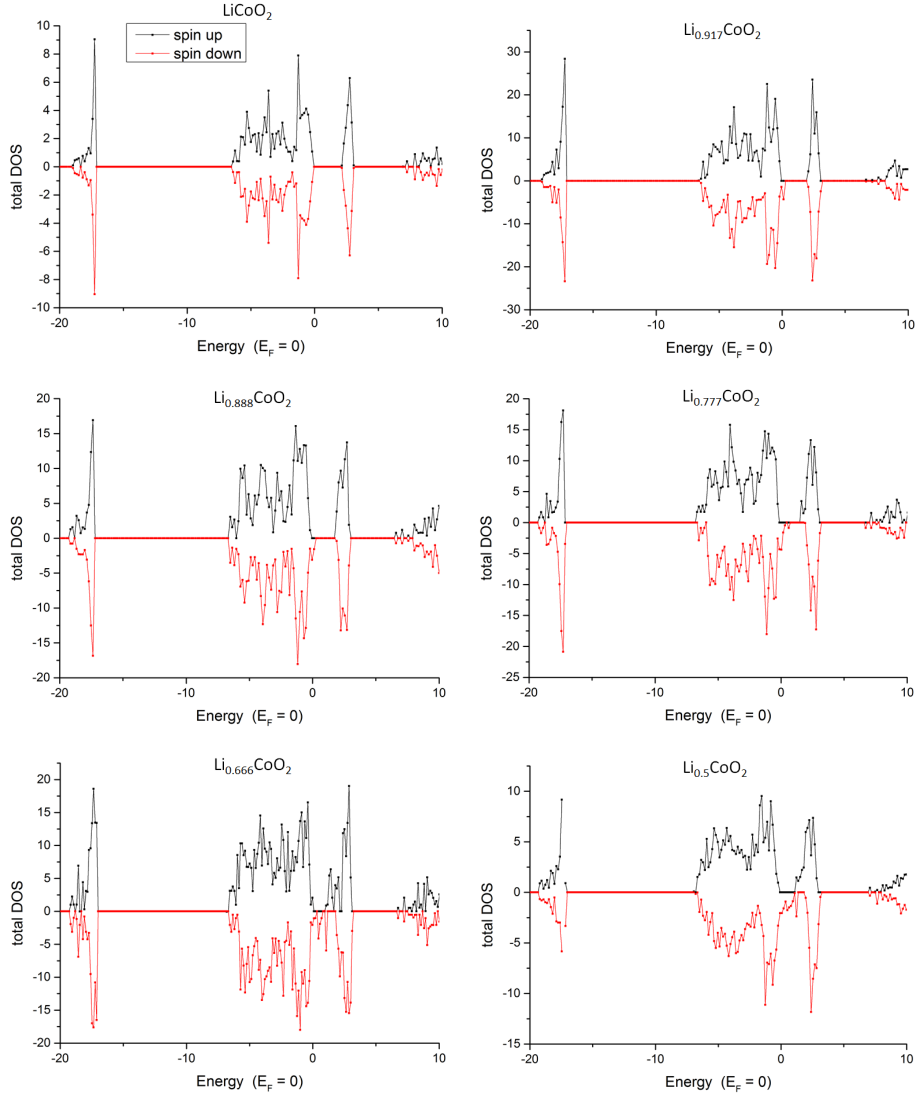


Figure 4.2: Electronic DOS in dependence of lithium content: tail states on top of the valence band and at the bottom of the conduction band can be observed when lithium is removed. The tail states merge below  $x=0.777$  leading to the metallic phase.

In particular, the merging of the conduction band and the valence band can indeed be interpreted in terms of the formation of an impurity band (see subsection 1.7.2 for explanation) visible as band tails on the valence and the conduction band in concordance with prior observations on very dilute concentrations by Marianetti et al. with the LDA-functional [53]. Ultimately, the merging of both bands occurs when reaching a stoichiometry of  $\text{Li}_{0.66}\text{CoO}_2$ . Judging these results, anything below  $x=0.77$  resembles a metallic state agreeing with what has been determined experimentally [49, 50]. The band gap value corresponding to the pristine, fully lithiated structure compares well to experimental data as can be seen in figure 4.3. Evaluating the crystal structure data reveals a similar trend compared to experimental data as can be observed in figure 4.4. Removing lithium ions successively

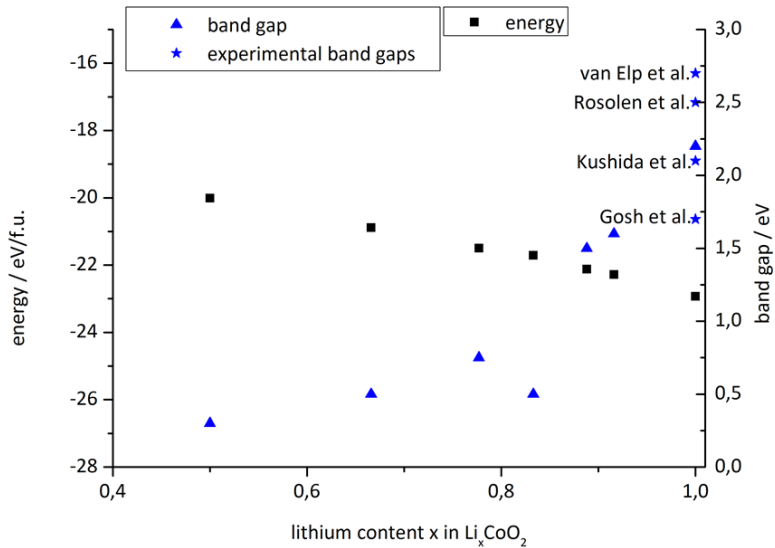


Figure 4.3: Calculated band gaps plotted in dependence of lithium content and comparison to experimental data: computed and experimental data at  $x=1$  show good agreement.

leads to an expansion of the c-axis parameter resulting from the increased

Coulomb repulsion between the layers. It is also possible to converge to both

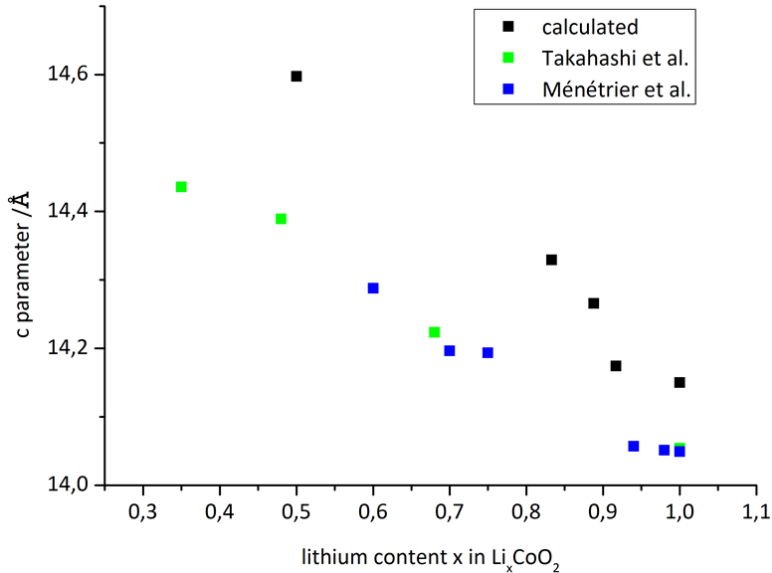


Figure 4.4: c lattice parameter in dependence of lithium content in  $\text{Li}_x\text{CoO}_2$ : comparison with experimental data of Ménétrier et al. [50] and Takahashi et al. [22] reveals good overall agreement.

metallic and insulating states for the same stoichiometry over a lithium content between  $x \in [0.5; 0.917]$  depending on the Li/Vac arrangement. Hence, it does indicate the phase coexistence of the metallic and the semiconducting phase. However, in general it is difficult to control the magnetic moments. Initializing with high spins on specific cobalt atoms does not necessarily lead to high spins on the respective cobalt atoms after the calculations. After analysing all results with respect to electronic DOS and total energy the energies are plotted both for the metallic and the insulating state in dependence of lithium content as shown in figure 4.5.

As can be seen, it is not possible to define a two-phase region by using the common tangent approach since the evolution of the energies for both states

are clearly non-parabolic. It might be necessary to model additional vacancy arrangements within the range of  $x \in [0.5;1]$  to obtain the true ground state configurations which might not yet be represented by the calculated crystal structures. Aside from this aspect the lack of the parabolic behaviour could

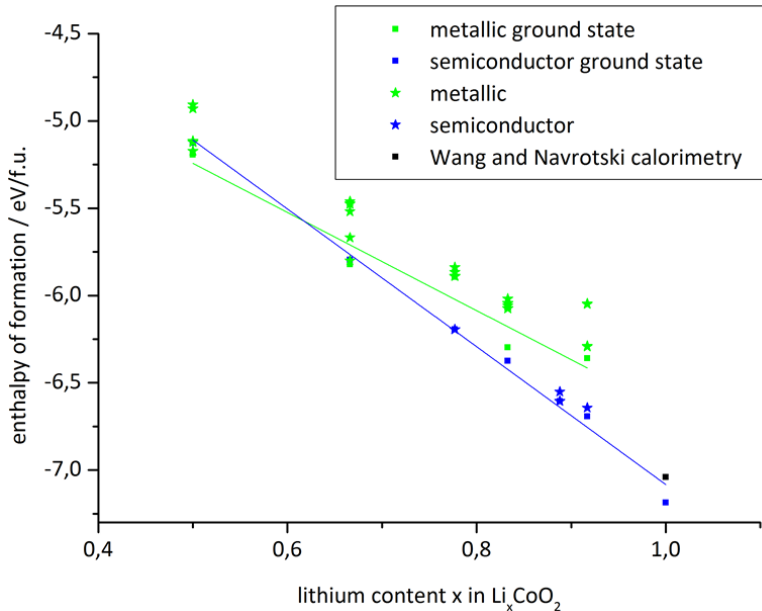


Figure 4.5: Enthalpies of formation versus the constituting elements for metallic and insulating states vs lithium content: good agreement in comparison to Wang and Navrotsky [86]. It is clearly observable that the semiconducting phase is more stable at high lithium contents. At  $x=0.5$  it is not possible any more to converge to a semiconducting phase.

also be related to the neglect of the contributions made by the entropy of mixing  $S_m$  to the Gibbs free energy which have significant effects in the limit of dilute concentrations according to the following equation for the Gibbs

free energy of mixing [87]:

$$\begin{aligned}
 G_m &= H_m - TS_m & (4.6) \\
 &= 1/2Nz \cdot [(1-x)H_{AA} + xH_{BB} + 2x(1-x)H_0] \\
 &\quad + NkT \cdot [x \ln x + (1-x) \ln(1-x)]
 \end{aligned}$$

, whereas A and B denote two different atomic species, N the number of atoms, z the coordination number  $H_0$  the exchange enthalpy,  $H_{AA}$  and  $H_{BB}$  the enthalpy of bonding between A or B atoms. In the limit of dilute concentrations the logarithm function converges to zero, i.e.  $\lim_{c \rightarrow 0} -TS_m \rightarrow 0$  and  $\lim_{(1-c) \rightarrow 0} -TS_m \rightarrow 0$ , whereas a finite absolute value is being subtracted for intermediate concentrations. Therefore this can alter the enthalpy of mixing to much lower values when moving away from dilute concentrations introducing local minima. To elucidate this aspect, the influence of the entropic term of equation 4.6 is checked assuming N to be the number of atoms in the cell. The analysis shows that the impact of that term is just marginal around room temperature. Only when going to high temperatures of 10000 K the effect is perceivable.

In conclusion, this hypothesis may be excluded as the cause for the lack of the parabolic behaviour. The remaining other hypothesis, as mentioned before, is that not the true ground states are obtained with the calculated structures. In this respect, constructing a cluster expansion with lithium and vacancies on one sublattice and cobalt(III) and cobalt(IV) on their respective sublattice can provide further insights by more thoroughly exploring the configurational space. This approach has been taken by Aykol et al. [private communication]. The authors applied different potentials for  $\text{Co}^{3+}$  and  $\text{Co}^{4+}$  respectively to account for the different number of electrons. Moreover, they assigned different Hubbard-U values to  $\text{Co}^{3+}$  and  $\text{Co}^{4+}$ , respectively, as they found evidence that the U value depends strongly on the oxidation state of the transition metal ion [88]. The results of this approach indeed display the

two-phase region whereas the authors are still uncertain about the specific cause for the correct mapping of this behaviour. They suggest the explicit treatment of cobalt(III) and cobalt(IV) as separate species as the reason for this behaviour but cannot confirm this hypothesis until proven. To investigate this, a separate cluster expansion should be carried out with identical  $U$  values on both  $\text{Co}^{3+}$  and  $\text{Co}^{4+}$  in order to be able to compare the changes with respect to the former approach. Despite the fact that the metal-to-insulator phase transition cannot not be modelled with the approach of this work the obtained total energies are used to calculate the average intercalation voltage in  $x \in [0.5; 1]$  according to equation 4.4. The results, as displayed in figure 4.6, show an essentially flat profile with values between 3.5 V and 4 V.

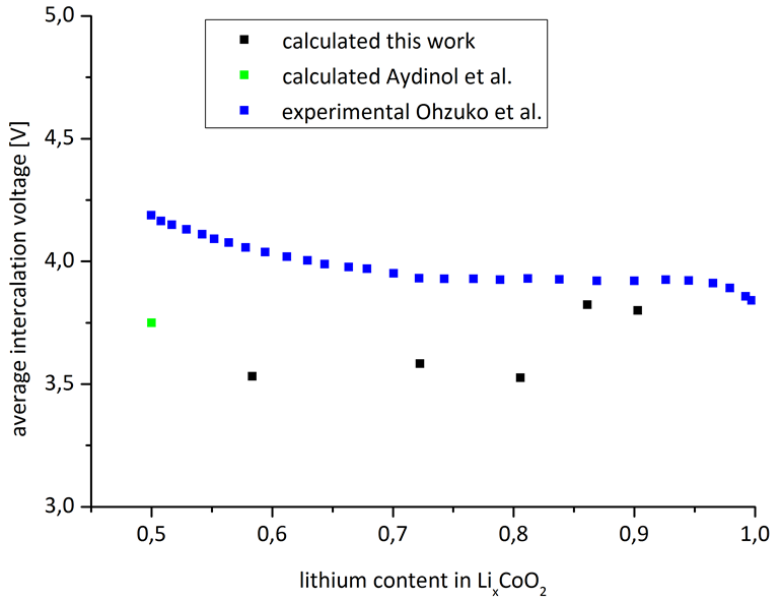


Figure 4.6: Computed average intercalation voltage of  $\text{Li}_x\text{CoO}_2$  compared to ab initio result of Aydinol et al. [89] and experimental voltage profile of Ohzuko et al. [16]

This is in good agreement with prior ab initio predictions of Aydinol et al., who computed one value as the average in the range of [0.5; 1] to be 3.75 V [89]. The discrepancy to experimentally obtained voltages (between 4 and 4.4 V [16]) is therefore in the same order of magnitude. Generally speaking, the calculated average intercalation voltage gives a rough estimate on the true intercalation voltage of the compound. However, the adopted approach is not sufficient to map the two-phase region accordingly.

### Conclusion

With the applied approach it was possible to converge to both metallic and semiconducting states over a lithium concentration range of  $x \in [0.5; 1]$ . The electronic DOS reveals the formation of band tails in the course of removing lithium from the pristine structure which broaden and ultimately merge below a lithium content of  $x=0.777$  with an associated total energy lower than for the semiconducting state. However, the devolution of the energies closely resembles a linear behaviour making it impossible to use the common tangent approach for deriving the two phase region. Still, at least the approach does confirm the metallic state to be more stable at lower lithium contents. The effects of the entropy of mixing are determined to be negligible around room temperature and do not even out the missing curvature of the total energy devolution. The computed average intercalation voltage is in agreement with the experimental profile and prior DFT calculations.

## 4.2.2 Heat capacities within the QHA

### Aim

$\text{Li}_x\text{CoO}_2$  is prone to have serious thermal issues under abuse conditions. Therefore, thermal modelling may contribute to an increase in safety of the battery design. For this purpose, data on heat capacities of the constituting battery components are relevant. In this section the advantage of the DFT method in obtaining heat capacities on delithiated stoichiometries of  $\text{LiCoO}_2$  is exploited. Isobaric heat capacities are calculated within the QHA for  $\text{LiCoO}_2$ ,  $\text{Li}_{0.67}\text{CoO}_2$ ,  $\text{Li}_{0.5}\text{CoO}_2$  and  $\text{LiCo}_{11/12}\text{B}_{1/12}\text{O}_2$ .

### Discussion

The lattice parameters obtained from the GGA+U approach are shown in the previous section. Here, the lattice parameters from GGA-PBE calculations are compiled in Table 1 and show that the pristine structure is in good agreement with experimental data. Both the results obtained from GGA-PBE and GGA+U are close to the experimental values. While the c-lattice parameter of the pristine structure is overestimated within GGA+U (as already seen in the previous section in dependence of different lithium concentrations in figure 4.4) it is only slightly underestimated within GGA-PBE in case of the pristine structure. However, the delithiated structures show significant deviation. In both  $\text{Li}_{0.67}\text{CoO}_2$  and  $\text{Li}_{0.5}\text{CoO}_2$  the c-lattice parameter is overestimated. This is likely due to increased contribution from van der Waals interactions that are not being considered with the applied exchange functionals [90]. It should be noted here that the calculated c-lattice parameter also depends on the lithium vacancy configuration of the chosen supercell. Another aspect to look at is the space group of the calculated structures, which deviate from the experimental ones in case of  $\text{Li}_{0.67}\text{CoO}_2$  and  $\text{Li}_{0.5}\text{CoO}_2$ .

Table 4.1: The calculated lattice parameters for different stoichiometries of  $\text{Li}_x\text{CoO}_2$  and experimental lattice parameters by Takahashi et al. [22] and Hertz et al. [30]

Compound	a [Å]	b [Å]	c [Å]
$\text{LiCoO}_2$ R-3m (166) U=5.6eV	2.838(1)	2.838(1)	14.144(5)
$\text{LiCoO}_2$ R-3m (166) GGA-PBE	2.856(2)	2.856(2)	14.014(9)
$\text{Li}_{0.67}\text{CoO}_2$ Cm (8) GGA-PBE	2.844(9)	2.844(9)	15.104(2)
$\text{Li}_{0.5}\text{CoO}_2$ P2/c (13)GGA-PBE	2.813(7)	2.813(7)	15.012(1)
$\text{Li}_{0.5}\text{CoO}_2$ P12/m1 (10) GGA-PBE	4.884(2)	2.838(2)	14.474(6)
$\text{LiCoO}_2$ R-3m (166) exp. [22]	2.8156(6)	2.8156(6)	14.0542(6)
$\text{Li}_{0.68}\text{CoO}_2$ R-3m (166) exp. [22]	2.8107(5)	2.8107(5)	14.2235(6)
$\text{Li}_{0.67}\text{CoO}_2$ R-3m (166) exp. [30]	2.81172(3)	2.81172(3)	14.2863(4)
$\text{Li}_{0.51}\text{CoO}_2$ C12/m1 (12) exp. [30]	4.8645(1)	2.80964(7)	5.0551(1)
$\text{Li}_{0.5}\text{CoO}_2$ P12/m1 (10) exp. [23]	4.865(3)	2.809(3)	5.063(3)
$\text{Li}_{0.48}\text{CoO}_2$ R-3m (166) exp. [22]	2.8090(15)	2.8090(15)	14.3890(17)

For  $\text{Li}_{0.67}\text{CoO}_2$  this is caused by a slight distortion of the structure and can be found to be described with space group  $C12/m1$  (12) when lowering the tolerance for finding the underlying symmetry. For  $\text{Li}_{0.5}\text{CoO}_2$  the discrepancy can be explained by the fact that all the modelled structures are based on the O3-polytype unit cell. Therefore, in spite of the full structure relaxations, the host structure is maintained and does not transform into the monoclinically distorted structure as determined by Takahashi et al. [22] of which the unit cell size is a third of the O3-polytype unit cell.

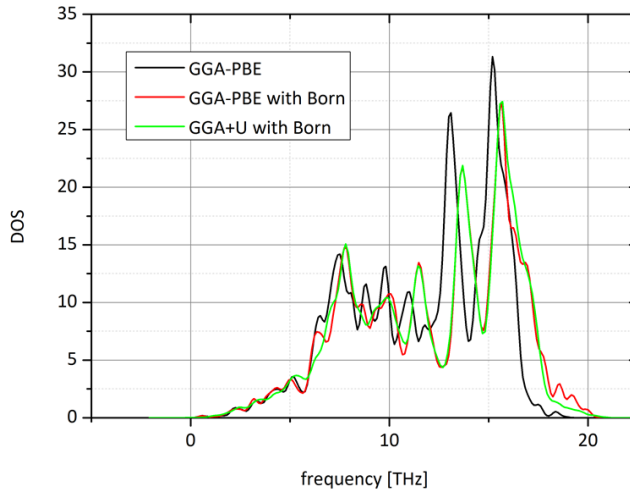


Figure 4.7: Phonon DOS of  $\text{LiCoO}_2$  calculated by the linear response method with 3 different parameters: GGA-PBE accounting for Born-charge, GGA-PBE without Born-charge and GGA+U accounting for Born charge. Phonon frequencies  $\nu > 0$  indicate that calculations are well converged and structures are stable.

The linear response calculations of the Hessian enabled the evaluation of Born charge effects on the phonon derived properties. The results on  $\text{LiCoO}_2$  yielded no phonon frequencies  $\nu < 0$  and therefore indicate convergence to a stable geometry irrespective of the employed functional and the inclusion of Born charge effects. The inclusion of Born-charges in the calculations revealed no significant impact on the isochoric heat capacity curves as can be seen in figure 4.8. Since the induced polarizations only affect the long wavelength longitudinal frequencies this might be an explanation for its vanishing impact.

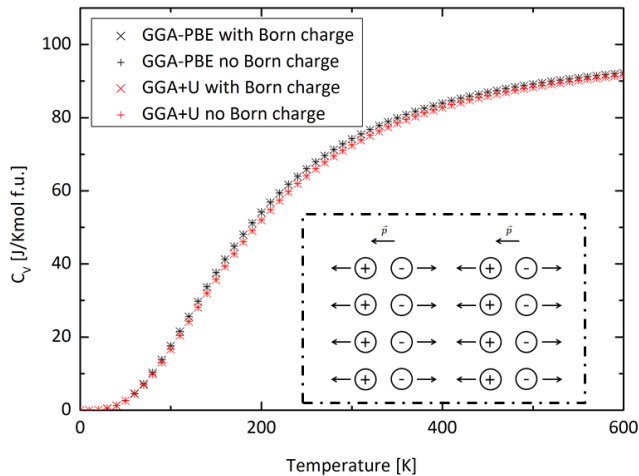


Figure 4.8: Demonstration of Born charge effects on the heat capacity of the pristine  $\text{LiCoO}_2$ : no significant impact on the resulting heat capacities can be observed. The inset displays the basic mechanism behind the Born effective charges, which are induced in the limit of long wave lengths of longitudinal modes. Dipoles induce an additional contribution  $\vec{p}$  to the restoring force.

The quasi-harmonic results with the GGA+U functional on  $\text{LiCoO}_2$  show that there is no significant influence either (figure 4.9). Comparing the phonon DOS of the calculations with a Hubbard U value to the calculations without a Hubbard U value shows that they do not display significant differences. The phonon DOS obtained from the Hubbard U calculation features slightly higher frequencies but lower DOS at frequencies in the vicinity of 15 THz. The presence of higher frequencies may explain the larger heat capacity values above 600 K. The phonon DOS of all three stoichiometries (figures

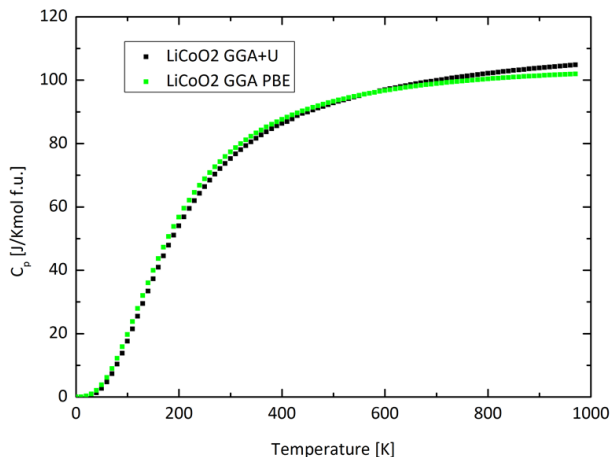


Figure 4.9: The impact of a Hubbard U value of 3.3 eV on the isobaric heat capacity of  $\text{LiCoO}_2$ : the results show only negligible effects.

4.7 and 4.10) revealed no imaginary frequencies indicating stable structures and well converged geometry except for the  $\text{Li}_{0.5}\text{CoO}_2$  P12/m1 (10) structure. In this case residual imaginary frequencies are still present even after careful re-relaxation and by modulating along the imaginary modes. Since the  $\text{Li}_{0.5}\text{CoO}_2$  P2/c (13) structure does not show any imaginary frequencies this particular structure is used to calculate the heat capacities.

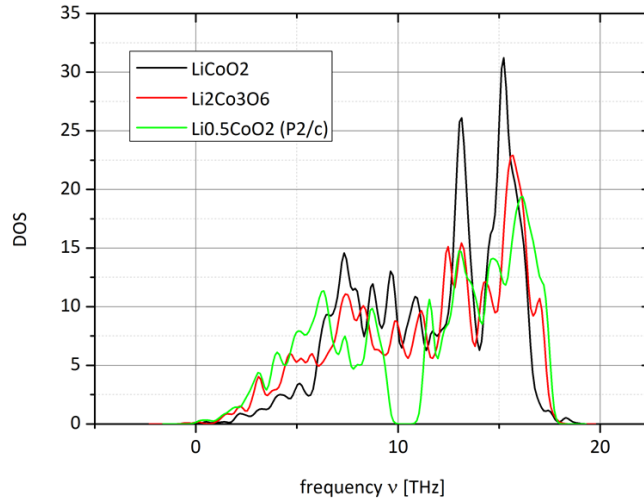


Figure 4.10: Phonon DOS of  $\text{LiCoO}_2$ ,  $\text{Li}_{0.67}\text{CoO}_2$  and  $\text{Li}_{0.5}\text{CoO}_2$  calculated by the finite difference method.  $\nu > 0$  indicates stable structures.

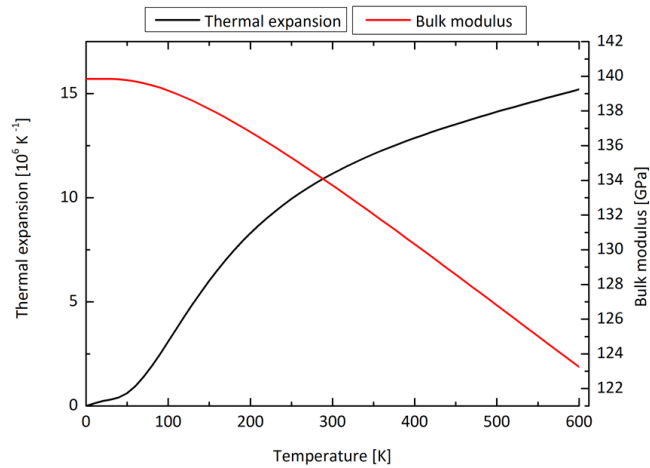


Figure 4.11: Bulk modulus and thermal expansion coefficient: obtained from the EOS fit on  $\text{LiCoO}_2$  and used to compute  $C_p$  by utilizing equation 3.24.

It can be assumed that there is no major difference in the derived heat capacities due to the fact that the heat capacity is obtained as a sum over all frequencies in the phonon DOS (equation 3.19). Small changes in the distribution of the DOS would not affect the heat capacity as an integral property. Due to the negligible impact the rest of the calculations are carried out with the exchange functional GGA-PBE and without taking Born-charges into account.

The quasi-harmonic fit for pristine, fully lithiated structure is shown exemplarily in figure 4.12 from which the thermal expansion and the bulk modulus is derived according to the equations in section 2.1.

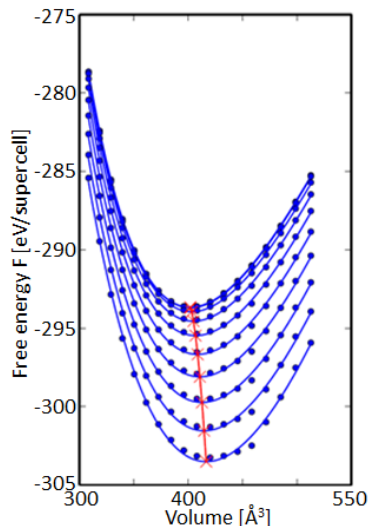


Figure 4.12: Quasi-harmonic fit of  $\text{LiCoO}_2$  over a series of volumes using the Birch-Murnaghan-EOS. The red line interconnects the minima at each temperature respectively, highlighting the thermal expansion.

These are shown in figure 4.11. What is also obtained from the fitting procedure is the Gibbs free energy by Legendre transformation of the Helmholtz free energy as illustrated in figure 4.13. The remaining plots of the other

structures are summarized in appendix B1.

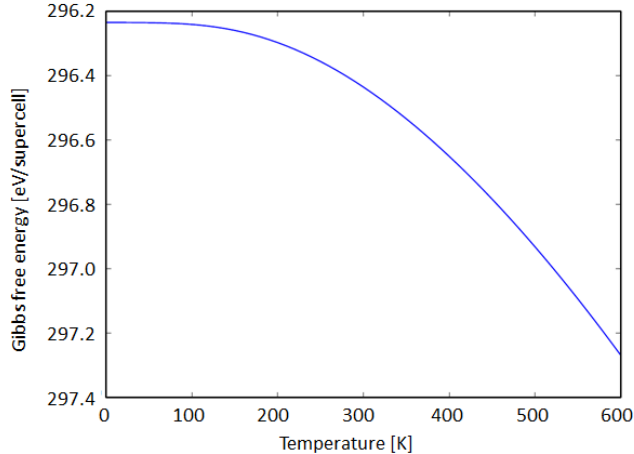


Figure 4.13: Gibbs free energy of the pristine  $\text{LiCoO}_2$  obtained by Legendre-transformation of the Helmholtz free energy

The obtained isobaric heat capacities are compiled in figure 4.14. As can be seen from the heat capacity curves the overall trend is modelled correctly although there is a deviation of the calculated results from the experimental ones. For the pristine structure the deviation between the calculated and the experimental heat capacity at  $T=298$  K amounts to  $\approx 6.8$  %. In general, deviations are to be expected due to the idealization of the crystal structure model. The results are obtained for a single crystalline compound with no grain boundaries and point defects apart from those introduced by the lithium vacancies. The even larger discrepancy for  $\text{Li}_{0.5}\text{CoO}_2$  can be explained by inaccuracies of the experiment since the experimental data of  $\text{Li}_{0.5}\text{CoO}_2$  is not based on a pure phase sample.

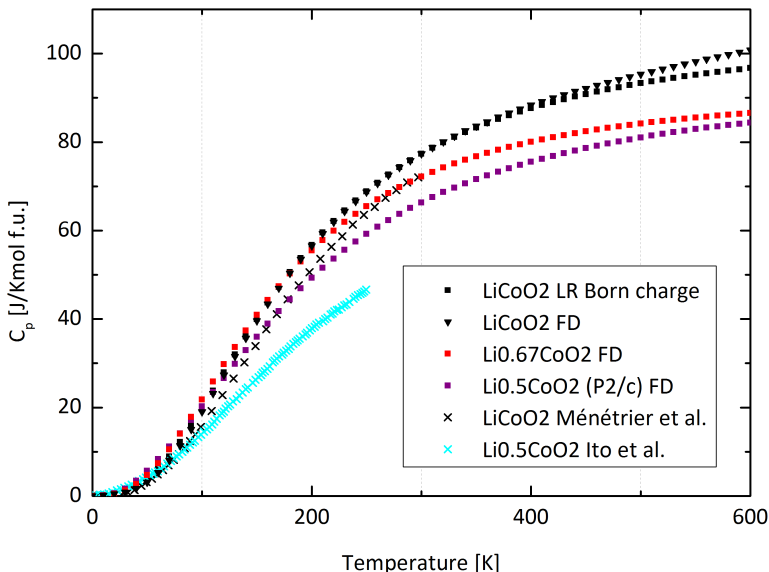


Figure 4.14: Calculated heat capacities at constant pressure for  $\text{LiCoO}_2$ ,  $\text{Li}_{0.67}\text{CoO}_2$  and  $\text{Li}_{0.5}\text{CoO}_2$  compared to available literature data.

The authors stated that their sample contained graphite and binder due to the experimental process of obtaining the sample. Based on the specified weight ratios of  $\text{LiCoO}_2$ , Graphite and PVDF-binder (see data sheet in appendix B1) the heat capacity for a hypothetically pure  $\text{Li}_{0.5}\text{CoO}_2$  compound is estimated for a temperature of 298 K to be  $C_p(\text{Li}_{0.5}\text{CoO}_2)=70.98$  J/molK which would be roughly 7 % larger than the calculated  $C_p(\text{calculated Li}_{0.5}\text{CoO}_2)=66.31$  J/molK. [31] This correction is shown in figure 4.15. Consequently, it displays agreement with the experimental data of Ito et al. The lack of experimental shortcomings, which usually introduce insecurities to experimental results, stresses the power of DFT calculations for obtaining properties of isolated materials (pure), which are otherwise difficult to access by experiment and principally underpins the usefulness of the calculated results. What is more, the experimental data by Ito et al. on  $\text{Li}_{0.5}\text{CoO}_2$  is only

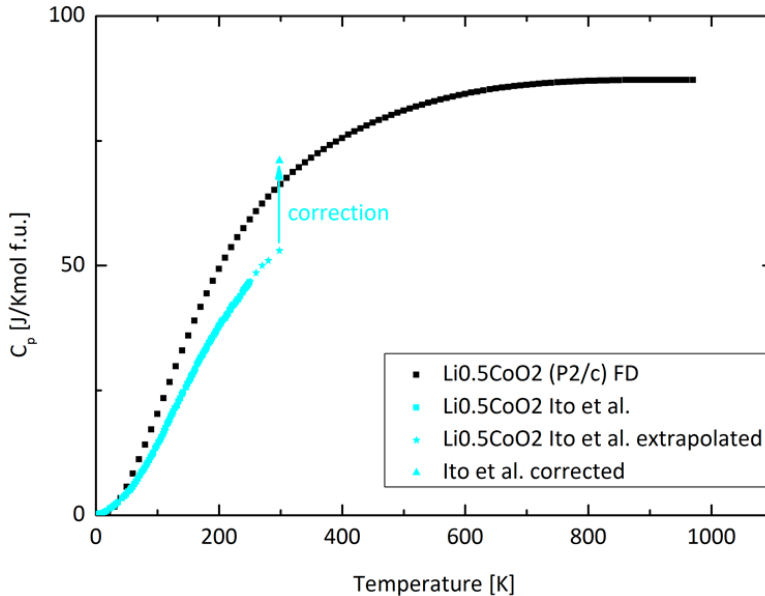


Figure 4.15: Heat capacity of  $\text{Li}_{0.5}\text{CoO}_2$  by Ito et al. with correction by accounting for the heat capacities of PVDF [91] and graphite [92] impurities in the sample.

obtained up to around 250 K (see 4.14) and does not cover the operational range with respect to temperature of a typical LIB. When calculating phonon properties within the DFT framework the temperature poses no big issue in terms of obtaining the target property and stresses its strength once again. The comparison of the pristine, fully lithiated structure indicates that these results give a reasonable estimate of the heat capacities at different stoichiometries and can complement the data set on physical properties to improve thermal modelling attempts in batteries. As of today, the models only apply the heat capacity data for fully lithiated compounds as part of the applied equations, thereby ignoring the composition dependency of the heat capacity. As mentioned by Wu et al. [93], one of the major shortcomings in the thermal modelling of battery cells is indeed the neglect of the com-

positional influence on thermal parameters. One of his findings is that the maximum temperature during operation is very sensitive to the exact heat capacity value. This strengthens the importance of the obtained data set in this work for adequately designing battery cells with improved thermal safety. A refined model for computational fluid dynamics (CFD) simulations, as done by Ponchaut et al. [94], taking the stoichiometry dependence of the heat capacities into account could yield more accurate results. The general trend in the calculated results of decreasing heat capacity with decreasing lithium content is physically plausible since the delithiated structures contain fewer atoms per formula unit to absorb the heat in the form of phonon vibrations. Therefore, a similar trend is also to be expected for other materials.

Doping with boron leads to a slight decrease in heat capacity which is noticeable at temperatures above 300 K (see figure 4.16). The relative decrease of the heat capacity values is in agreement with theoretical considerations which would predict a lower heat capacity due to the smaller atomic weight of the substituent boron. The smaller atomic weight requires less energy (heat) to excite phonons of similar order of magnitude. For possible utilization in the calculation of phase diagrams (CALPHAD) community the results are fitted by an empirical polynomial in a temperature range of  $T \in [250; 600]$  K using the adjusted  $R^2$  as the measure of the goodness of fit. It is designed to penalize a fit function with more parameters than necessary. A  $R^2$  is therefore a good measure for a good fit function with as few terms as possible. The adjusted  $R^2$  is defined by:

$$\bar{R}^2 = R^2 - (1 - R^2) \cdot \frac{p}{n - p - 1} \quad (4.7)$$

with  $\bar{R}^2$  being the adjusted  $R^2$ ,  $p$  the number of independent variables (in this case just one), and  $n$  the sample size, i.e. the number of data points.  $R^2$

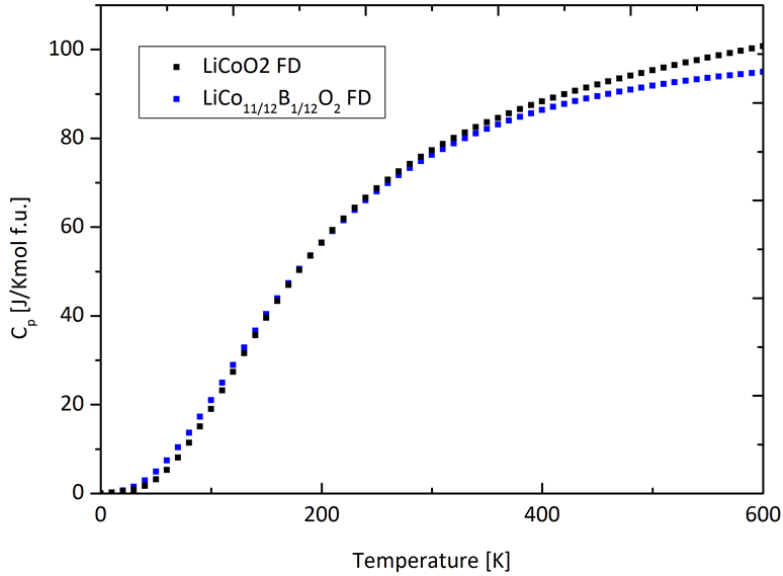


Figure 4.16: Influence of boron-doping on heat capacity: substitution of cobalt with boron leads to a decrease of the isobaric heat capacity as a result of the smaller weight of boron.

itself is the coefficient of determination defined by:

$$R^2 = 1 - \frac{\sum_i (y_i - f_i)^2}{\sum_i (y_i - \bar{y})^2} \quad (4.8)$$

where the numerator is the square sum of residuals and the denominator is the error sum of squares (SSE). The following polynomial was employed and yielded good fits:

$$C_p = a_1 + a_2 \cdot T + a_3 \cdot T^{-2}. \quad (4.9)$$

The fits are shown in figure 4.17. The fitting coefficients along with the adjusted  $R^2$  values are listed in table 4.2.

Table 4.2: Coefficients for the heat capacity polynomials

compound	$\bar{R}^2$	$a_1 / \frac{\text{J}}{\text{mol}\cdot\text{K}}$	$a_2 / 10^{-4} \frac{\text{J}}{\text{mol}\cdot\text{K}^2}$	$a_3 / 10^6 \frac{\text{J}\cdot\text{K}}{\text{mol}}$
$\text{LiCoO}_2$	0.99993	$82.4 \pm 0.219$	$374 \pm 3.589$	$-1.46 \pm 0.010$
$\text{Li}_{0.67}\text{CoO}_2$	0.9996	$84.7 \pm 0.350$	$98 \pm 5.736$	$-1.37 \pm 0.016$
$\text{Li}_{0.5}\text{CoO}_2$ (P2/c)	0.9993	$75.1 \pm 0.564$	$224 \pm 9.225$	$-1.37 \pm 0.0263$
$\text{LiCo}_{11/12}\text{B}_{1/12}\text{O}_2$	0.99929	$90.5 \pm 0.605$	$157 \pm 9.903$	$-1.69 \pm 0.028$

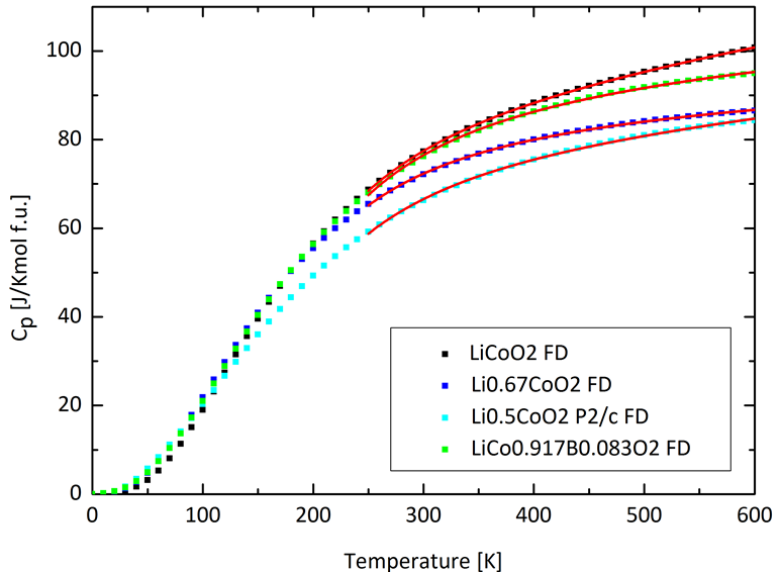


Figure 4.17: CALPHAD-type fitting curves (red lines) from 250 K to 600 K by employing the empirical polynomial of equation 4.9 on  $\text{LiCoO}_2$ ,  $\text{Li}_{0.67}\text{CoO}_2$ ,  $\text{Li}_{0.5}\text{CoO}_2$  and  $\text{LiCo}_{11/12}\text{B}_{1/12}\text{O}_2$ .

## Conclusion

Born-charge effects and the impact of a Hubbard  $U$  term have been determined to be negligible with regard to the computed heat capacities. The calculated isobaric heat capacities are in good agreement with available experimental data and therefore demonstrate that the QHA is a robust method to yield the data particularly for delithiated  $\text{LiCoO}_2$  which is only difficult to obtain via an experimental approach. The obtained data for the delithiated stoichiometries could be used to enhance CFD models for a more accurate evaluation of the heat distribution in cells in pursuit of the identification of hot spots.

### 4.2.3 Cluster expansion of $\text{Li}_x\text{Mg}_2\text{Si}$

#### Aim

In the recent years the  $\text{Li}_x\text{Mg}_2\text{Si}$  compound has been studied as a potential candidate for the anode of a LIB. Its advantages are the abundance of silicon and magnesium as well as their non-toxicity. In the following section the average intercalation voltage of the compound is derived from the total energies obtained from the cluster expansion method as implemented in ATAT. This method is used in order to probe different configurations more thoroughly. In this context, the effect of lithium insertion on the host lattice is evaluated as well.

#### Discussion

Total energies of over 150 structures are obtained in the concentration range  $x \in [0;1]$  by running the cluster expansion code ATAT. These are displayed in the plot of figure 4.18. As it can be observed the cluster expansion still pre-

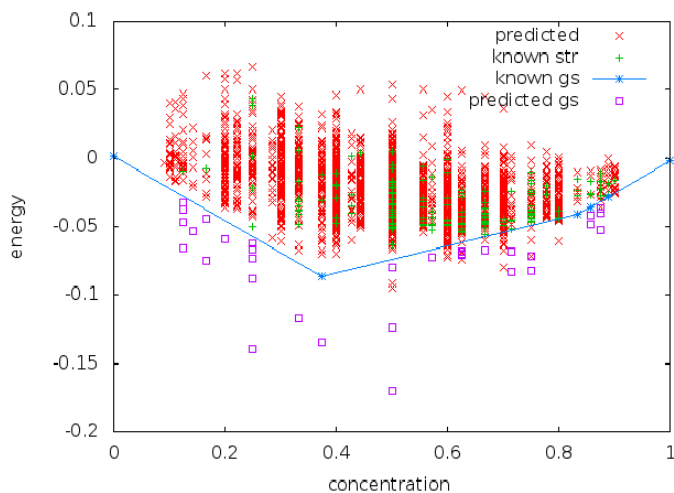


Figure 4.18: Cluster expansion of  $\text{Li}_x\text{Mg}_2\text{Si}$

dicts structures with lower energies. Consequently, further structures have to be calculated via DFT. Structures, which show significant non-isotropic relaxation, are excluded from the cluster expansion since the inclusion leads to large errors in the parametrization of the energy for the cluster expansion. One can observe (figure 4.19) that the relaxations show systematic deviations at higher lithium concentrations  $> 0.5$  (vacancy concentrations  $< 0.5$ ) due to the increased lithium incorporation in the parent lattice. This is a potential drawback of this compound if chosen as the electrode material since the alternating volume changes would induce mechanical stress and quickly lead to cracks in the bulk material and the disintegration thereof promoting capacity fade as has been observed in many other intercalation compounds before [95–102].

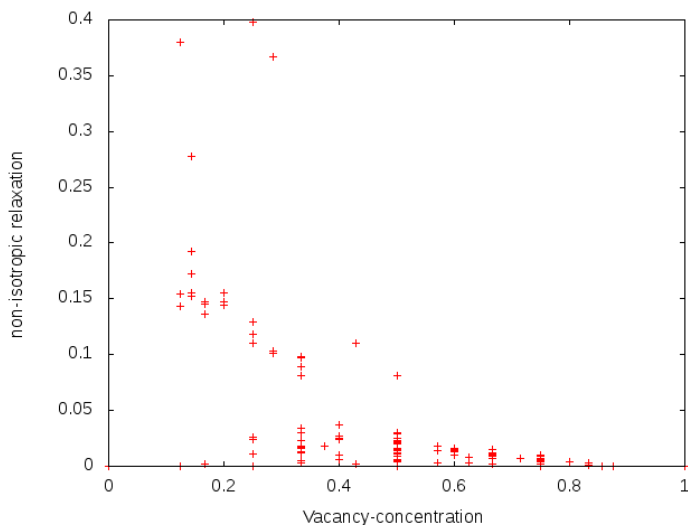


Figure 4.19: Non-isotropic relaxation of calculated structure on  $\text{Li}_x\text{Mg}_2\text{Si}$ . As can be observed the relaxations at lower vacancy concentrations the relaxations increase significantly due to lattice distortions upon lithium intake.

The effective cluster interactions (ECIs) are shown in figure 4.20 and reveal

that there is no clear decay of the ECIs in dependence of the atoms distance. This explains the slow convergence of the cluster expansion. With the effec-

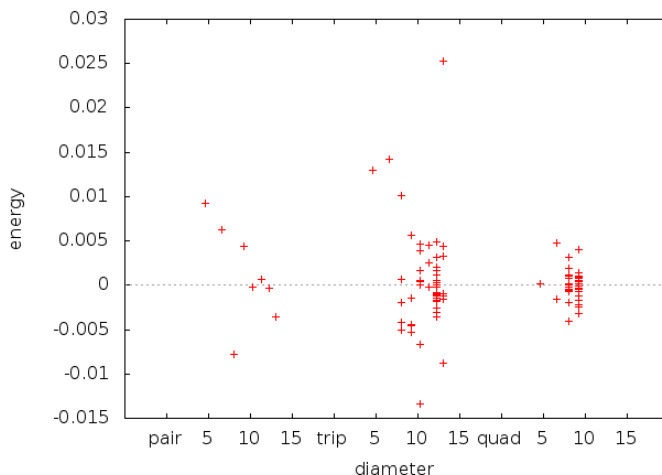


Figure 4.20: ECIs obtained from the cluster expansion: no clear decay can be observed with growing size of the clusters from pairs to triplets to quadruplets.

tive cluster interactions so far the predictions made by the cluster expansion are reasonably well as shown in figure 4.21. We used the obtained total energies of a selected set of compositions to compute the average intercalation voltage according to equation 4.5. These results are shown in figure 4.22. Comparing the calculated voltage profile with experimental data by Kim et al. has to take into account that the experimental profile extends up to a 3.9 mol (1370 mAh/g) of lithium insertion [103] which exceeds the range that is computed. The computed range is equivalent to the reaction of 1 mol of lithium which translates into 351 mAh/g. As can be seen from figure 4.22 the computed average intercalation voltage is well within the range as obtained experimentally although it is underestimated by about 0.4 V. Due to the underestimation the computed results suggest a negative potential versus

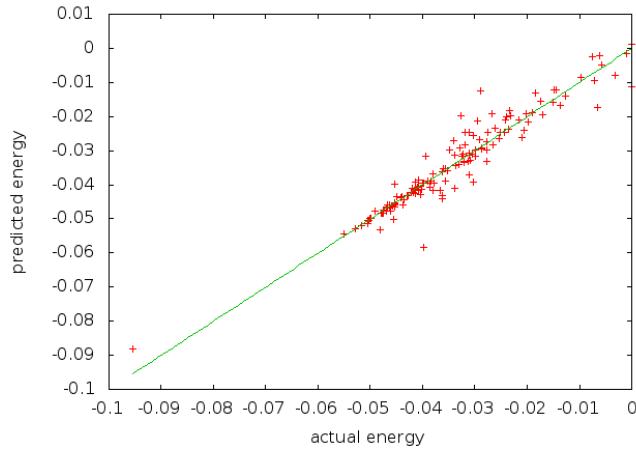


Figure 4.21: Predicted energies by the LOOCV method plotted versus the calculated energies show good agreement.

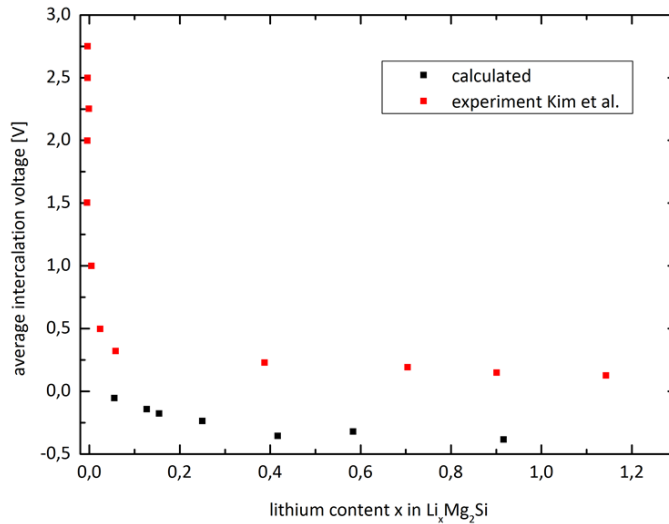


Figure 4.22: The calculated average intercalation voltage of  $\text{Li}_x\text{Mg}_2\text{Si}$  compared to the first electrochemical cycle of an experiment by Kim et al. [103]

pure lithium whereas experimentally the potential takes an average value of 0.07 V. The singular behaviour of the experimental profile at dilute concentrations ( $x \rightarrow 0$ ) is not captured in the computed profile since no structures with  $x < 0.111$  are computed which would require very large supercells. But the larger part of the profile with the slightly sloping feature in the range above  $x = 0.111$  is reproduced. In general, when computing the average intercalation voltage for several segments, there is a high degree of freedom in choosing the set of structures from which to derive the average intercalation voltages due to the large number of computed structures. Depending on the specific choice, the derived voltage profile can differ and contains steps in the devolution. Also, using the structures assigned as ground states does not imply a closer resemblance to experimentally obtained voltage profiles since the compounds do not fully reach thermodynamic equilibrium at the applied cycling rates and temperature. But this approach can be conveniently used as a screening method to check the intercalation voltage of different electrode compounds relative to each other.

### Conclusion

The cluster expansion approach has been employed to explore configurational space with regard to the total energy more thoroughly for the solid solution compound  $\text{Li}_x\text{Mg}_2\text{Si}$ . The analysis of the structure relaxations indicates a progressing lattice distortion of the host lattice with increasing lithium content and may point out a possible deterioration cause of the material by means of destabilization of the lattice in combination with material fatigue due to alternating mechanical strain during cycling. This reaffirms the importance of morphological design for the reduction of intercalation-induced stresses [27,100]. The computed average intercalation voltage underestimates the experimental profile by around 0.4 V resulting in a slightly negative profile versus lithium. Nevertheless, the slightly sloping trend at  $x > 0.1$  is captured accordingly.

# Chapter 5

## Summary and outlook

In this thesis the methodological approach of calculating equilibrium properties of intercalation compounds for LIBs by means of DFT calculations has been established within the institute. This included the choice of the proper ab initio code, in which case the code of choice was VASP, which uses projector-augmented waves to efficiently model solid state compounds with high accuracy. Moreover, the writing of project proposals for computing time on the supercomputing cluster JUROPA and JURECA was a part of the work.

Investigations were carried out on the intercalation compounds  $\text{Li}_x\text{CoO}_2$  and  $\text{Li}_x\text{Mg}_2\text{Si}$ . Since there is no published DFT-based work on the metal-to-insulator transition on the  $\text{Li}_x\text{CoO}_2$  compound it was attempted to map this transition in terms of the two phase region by calculating the enthalpy of formation with respect to the constituting elements. The applied approach with a single Hubbard U parameter of  $U=3.3$  eV for all cobalt ions and varying spin polarizations did not prove to be sufficient to capture the two phase equilibrium properly although it was possible to converge to metallic and semiconducting states with the metallic state being energetically more stable at lower lithium contents. In this respect, the transition from the semiconducting to the metallic state can be observed by means of the elec-

tronic DOS. Band tails at the upper edge of the valence band and the lower edge of the conduction band can be observed as a result of the formation of impurity bands when removing lithium from the structure ultimately leading to the merging of valence and conduction band. The two-phase equilibrium could not be defined due to the absence of local minima in the energetic deconvolution of the phases. However, due to renewed evidence, a more promising approach is to use two U parameters to account for the different oxidation states of the cobalt ions in order to facilitate hole localization at predefined sites. Nevertheless, the computed average intercalation voltage based on the obtained total energies of a set of compositions gives a good estimate on the true intercalation voltage. Discrepancies in the range of  $x \in [0.5; 1]$  amount to an average intercalation voltage 0.5 V lower in comparison to experimental data.

Motivated by existing safety hazards related to thermal abuse conditions of LIBs containing  $\text{LiCoO}_2$  as cathode the DFT guided derivation of relevant data (such as heat capacities) for an improved design of such batteries was sought to be imperative. In this respect, modelling isobaric heat capacities in the quasi-harmonic approximation on three different stoichiometries of  $\text{Li}_x\text{CoO}_2$  revealed good agreement with experimental data. Particularly for delithiated states, the calculations provide a powerful approach to obtain heat capacities on pure compounds whereas experiments can only yield data on contaminated samples caused by the experimental conditions. Predictions made on doped material are reasonable. Therefore this shows that heat capacities obtained by DFT can provide a superior method to yield data relevant for the thermal design and modelling (CFD modelling) of battery cells with  $\text{LiCoO}_2$  which are prone to have thermal issues. The isobaric heat capacities were fit in the range of  $T \in [250; 600]$  K by polynomials for potential usage in CALPHAD-type modelling.

Lastly, the cluster expansion method was utilized to get a detailed mapping of the total energy surface of the intercalation compound  $\text{Li}_x\text{Mg}_2\text{Si}$  in the

range of  $x \in [0; 1]$  to calculate the average intercalation voltage. The data displayed a shift of roughly 0.4 V less compared to the experimental voltage profile resulting in a negative voltage versus lithium. The significant volume changes occurring in the course of increasing lithium incorporation display potential drawbacks of this intercalation compound similar to  $\text{LiCoO}_2$  or  $\text{LiMn}_2\text{O}_4$ . In this respect, the importance of adequate morphological design for intercalation electrode materials to accommodate the volume changes, e.g. by combining with an elastic matrix to form composite electrode architectures, is emphasized once again.

In conclusion, computing the voltage profile in dependence of lithium content is a feasible task. The undetermined aspect lies in the choice of structures (lithium/vacancy configuration) since there is basically an infinite amount of possible configurations and can introduce variations in the computed profiles. Regarding the remodelling of the three phase region between the  $\text{Li}_x\text{Mg}_2\text{Si}$  solid solution,  $\text{Li}_2\text{MgSi}$  and the magnesium-rich solid solution ( $\text{Mg}_x\text{Li}_{1-x}$ ) it would be worthwhile to continue with the cluster expansion approach in combination with lattice Monte Carlo calculations as implemented in ATAT. This allows the computation of the free energy of these phases in their stoichiometry ranges whereas the Monte Carlo code extends the size of the DFT based structures to cover a larger configurational space than possible with sole DFT calculations. The strength of this approach in comparison to the CALPHAD approach using just the calculated enthalpy of formation on the end members ( $\text{Mg}_2\text{Si}$ ,  $\text{Mg}_x\text{Li}_{1-x}$  and  $\text{Li}_2\text{MgSi}$ ) lies in the additional parametrization of the energy surface by explicitly providing data between the end members. Hence, there is less degrees of freedom for the interpolation within the CALPHAD method allowing for a more accurate modelling of the phase diagram.



# Bibliography

- [1] H. Budde-Meiwes, J. Drillkens, B. Lunz, J. Muennix, S. Rothgang, J. Kowal, and D. U. Sauer, “A review of current automotive battery technology and future prospects,” *Proceedings of the Institution of Mechanical Engineers, Part D: Journal of Automobile Engineering*, vol. 227, no. 5, pp. 761–776, 2013.
- [2] H. D. Yoo, E. Markevich, G. Salitra, D. Sharon, and D. Aurbach, “On the challenge of developing advanced technologies for electrochemical energy storage and conversion,” *Materials Today*, vol. 17, no. 3, pp. 110–121, 2014.
- [3] T. Moriga, K. Watanabe, D. Tsuji, S. Massaki, and I. Nakabayashi, “Reaction mechanism of metal silicide  $\text{mg}_2\text{si}$  for li insertion,” *Journal of Solid State Chemistry*, vol. 153, no. 2, pp. 386–390, 2000.
- [4] L. Xiao, Y. Cao, J. Xiao, W. Wang, L. Kovarik, Z. Nie, and J. Liu, “High capacity, reversible alloying reactions in  $\text{sn}/\text{sb}/\text{c}$  nanocomposites for na-ion battery applications,” *Chemical Communications*, vol. 48, no. 27, pp. 3321–3323, 2012.
- [5] F. Wang, R. Robert, N. A. Chernova, N. Pereira, F. Omenya, F. Badway, X. Hua, M. Ruotolo, R. Zhang, L. Wu, *et al.*, “Conversion reaction mechanisms in lithium ion batteries: study of the binary metal fluo-

- ride electrodes,” *Journal of the American Chemical Society*, vol. 133, no. 46, pp. 18828–18836, 2011.
- [6] C. Menictas, M. Skyllas-Kazacos, and T. Lim, *Advances in Batteries for Medium and Large-Scale Energy Storage: Types and Applications*. Woodhead Publishing Series in Energy, Elsevier Science, 2014.
- [7] X. Yuan, H. Liu, and J. Zhang, *Lithium-Ion Batteries: Advanced Materials and Technologies*. Green Chemistry and Chemical Engineering, Taylor & Francis, 2011.
- [8] J. Park, *Principles and Applications of Lithium Secondary Batteries*. EngineeringPro collection, Wiley, 2012.
- [9] K. Xu, “Electrolytes and interphases in li-ion batteries and beyond,” *Chemical reviews*, vol. 114, no. 23, pp. 11503–11618, 2014.
- [10] P. Verma, P. Maire, and P. Novák, “A review of the features and analyses of the solid electrolyte interphase in li-ion batteries,” *Electrochimica Acta*, vol. 55, no. 22, pp. 6332–6341, 2010.
- [11] R. Korthauer, *Handbuch Lithium-Ionen-Batterien*. Springer, 2013.
- [12] A. Mendiboure, C. Delmas, and P. Hagemuller, “New layered structure obtained by electrochemical deintercalation of the metastable  $\text{LiCoO}_2$  (o2) variety,” *Materials research bulletin*, vol. 19, no. 10, pp. 1383–1392, 1984.
- [13] R. Berthelot, D. Carlier, M. Pollet, J.-P. Doumerc, and C. Delmas, “Synthesis and investigations on an  $\text{o}_4\text{-LiCoO}_2$  polytype,” *Electrochemical and Solid-State Letters*, vol. 12, no. 11, pp. A207–A210, 2009.
- [14] R. Huggins, *Advanced Batteries: Materials Science Aspects*. Springer-Link: Springer e-Books, Springer, 2008.

- [15] S. Santhanagopalan, K. Smith, J. Neubauer, G. Kim, A. Pesaran, and M. Keyser, *Design and Analysis of Large Lithium-Ion Battery Systems*. Artech House Publishers, 2014.
- [16] T. Ohzuku and A. Ueda, "Solid-state redox reactions of  $\text{LiCoO}_2$  (r-3m) for 4 volt secondary lithium cells," *Journal of The Electrochemical Society*, vol. 141, no. 11, pp. 2972–2977, 1994.
- [17] Y.-I. Jang, N. J. Dudney, D. A. Blom, and L. F. Allard, "High-voltage cycling behavior of thin-film  $\text{LiCoO}_2$  cathodes," *Journal of The Electrochemical Society*, vol. 149, no. 11, pp. A1442–A1447, 2002.
- [18] N. S. Ergang, J. C. Lytle, H. Yan, and A. Stein, "Effect of a macropore structure on cycling rates of  $\text{LiCoO}_2$ ," *Journal of The Electrochemical Society*, vol. 152, no. 10, pp. A1989–A1995, 2005.
- [19] C.-N. Li, J.-M. Yang, V. Krasnov, J. Arias, and K.-W. Nieh, "Microstructural stability of nanocrystalline  $\text{LiCoO}_2$  in lithium thin-film batteries under high-voltage cycling," *Applied physics letters*, vol. 90, no. 26, p. 3102, 2007.
- [20] H.-W. Lu, L. Yu, W. Zeng, Y.-S. Li, and Z.-W. Fu, "Fabrication and electrochemical properties of three-dimensional structure of  $\text{LiCoO}_2$  fibers," *Electrochemical and Solid-State Letters*, vol. 11, no. 8, pp. A140–A144, 2008.
- [21] R. F. B. Gabrisch, H.; Yazami, "Hexagonal to cubic spinel transformation in lithiated cobalt oxide," *J. Electrochem. Soc.*, vol. 151, pp. A891–, 2004.
- [22] Y. Takahashi, N. Kijima, K. Dokko, M. Nishizawa, I. Uchida, and J. Akimoto, "Structure and electron density analysis of electrochemically and chemically delithiated  $\text{LiCoO}_2$  single crystals," *J. Solid State Chem.*, vol. 180, pp. 313–321–, 2007.

- [23] Y. Takahashi, N. Kijima, K. Tokiwa, T. Watanabe, and J. Akimoto, "Single-crystal synthesis, structure refinement and electrical properties of  $\text{Li}_0.5\text{CoO}_2$ ," *Journal of Physics: Condensed Matter*, vol. 19, no. 43, p. 436202, 2007.
- [24] J. Bates, N. Dudney, B. Neudecker, F. Hart, H. Jun, and S. Hackney, "Preferred orientation of polycrystalline  $\text{LiCoO}_2$  films," *Journal of The Electrochemical Society*, vol. 147, no. 1, pp. 59–70, 2000.
- [25] Z. Wang, L. Liu, L. Chen, and X. Huang, "Structural and electrochemical characterizations of surface-modified  $\text{LiCoO}_2$  cathode materials for li-ion batteries," *Solid State Ionics*, vol. 148, no. 3, pp. 335–342, 2002.
- [26] M. Jo, Y.-S. Hong, J. Choo, and J. Cho, "Effect of  $\text{LiCoO}_2$  cathode nanoparticle size on high rate performance for li-ion batteries," *Journal of The electrochemical society*, vol. 156, no. 6, pp. A430–A434, 2009.
- [27] S. Luo, K. Wang, J. Wang, K. Jiang, Q. Li, and S. Fan, "Binder-free  $\text{LiCoO}_2$ /carbon nanotube cathodes for high-performance lithium ion batteries," *Advanced Materials*, vol. 24, no. 17, pp. 2294–2298, 2012.
- [28] J. Van Elp, J. Wieland, H. Eskes, P. Kuiper, G. Sawatzky, F. De Groot, and T. Turner, "Electronic structure of  $\text{CoO}$ ,  $\text{Li-doped CoO}$ , and  $\text{LiCoO}_2$ ," *Physical Review B*, vol. 44, no. 12, p. 6090, 1991.
- [29] R. Radwanski and Z. Ropka, "Magnetic properties and the electronic structure of  $\text{LiCoO}_2$ ," *arXiv preprint cond-mat/0610611*, 2006.
- [30] J. Hertz, Q. Huang, T. McQueen, T. Klimczuk, J. Bos, L. Viciu, and R. Cava, "Magnetism and structure of  $\text{Li}_x\text{CoO}_2$  and comparison to  $\text{Na}_x\text{CoO}_2$ ," *Physical Review B*, vol. 77, no. 7, p. 075119, 2008.
- [31] K. K. H. A. T. A. . H. Y. Ito, A.; Tanaka, "Magnetic phase transition of  $\text{Li}_{0.75}\text{CoO}_2$  compared with  $\text{LiCoO}_2$  and  $\text{Li}_{0.5}\text{CoO}_2$ ," *J. Therm. Analysis and Cal.*, vol. 92, pp. 399–401–, 2008.

- [32] . A. Van der Ven, M. Aydinol, G. Ceder, G. Kresse, and J. Hafner, "First-principles investigation of phase stability in  $\text{Li}_x\text{CoO}_2$ ," *Physical Review B*, vol. 58, no. 6, p. 2975, 1998.
- [33] S. Choi and A. Manthiram, "Factors influencing the layered to spinel-like phase transition in layered oxide cathodes," *J. Electrochem. Soc.*, vol. 149, pp. A1157–, 2002.
- [34] Z. Chen, Z. Lu, and J. Dahn, "Staging phase transitions in  $\text{Li}_x\text{CoO}_2$ ," *Journal of The Electrochemical Society*, vol. 149, no. 12, pp. A1604–A1609, 2002.
- [35] V. Subramanian, C. Chen, H. Chou, and G. Fey, "Microwave-assisted solid-state synthesis of  $\text{LiCoO}_2$  and its electrochemical properties as a cathode material for lithium batteries," *J. Mater. Chem.*, vol. 11, no. 12, pp. 3348–3353, 2001.
- [36] G. A. Nazri, A. Rougier, and K. F. Kia, "Synthesis, characterization, and electrochemical performances of substituted layered transition metal oxides.  $\text{Li}_{1-y}\text{M}'_y\text{O}_2$ . ( $\text{M}=\text{Ni}$  and  $\text{Co}$ .  $\text{M}'=\text{B}$  and  $\text{Al}$ )," in *Symposium R – Solid State Chemistry of Inorganic Materials*, vol. 453 of *MRS Online Proceedings Library*, 1996.
- [37] G. Amatucci, J. Tarascon, D. Larcher, and L. Klein, "Synthesis of electrochemically active  $\text{LiCoO}_2$  and  $\text{LiNiO}_2$  at  $100^\circ\text{C}$ ," *Solid State Ionics*, vol. 84, pp. 169–180, 1996.
- [38] Y.-M. Chiang, Y.-I. Jang, H. Wang, B. Huang, D. R. Sadoway, and P. Ye, "Synthesis of  $\text{LiCoO}_2$  by decomposition and intercalation of hydroxides," *Journal of the Electrochemical Society*, vol. 145, no. 3, pp. 887–891, 1998.

- [39] C. Chen, E. Kelder, and J. Schoonman, "Effect of layer morphology on the lithium-ion diffusion in thin  $\text{Li}_x\text{CoO}_2$  films," *Journal of materials science letters*, vol. 16, no. 24, pp. 1967–1969, 1997.
- [40] Y. Gu, D. Chen, and X. Jiao, "Synthesis and electrochemical properties of nanostructured  $\text{LiCoO}_2$  fibers as cathode materials for lithium-ion batteries," *The Journal of Physical Chemistry B*, vol. 109, no. 38, pp. 17901–17906, 2005.
- [41] D. Kramer and G. Ceder, "Tailoring the morphology of  $\text{LiCoO}_2$ : a first principles study," *Chemistry of Materials*, vol. 21, no. 16, pp. 3799–3809, 2009.
- [42] D. Wang, X. Ma, Y. Wang, L. Wang, Z. Wang, W. Zheng, X. He, J. Li, Q. Peng, and Y. Li, "Shape control of  $\text{CoO}$  and  $\text{LiCoO}_2$  nanocrystals," *Nano Research*, vol. 3, no. 1, pp. 1–7, 2010.
- [43] T. Motohashi, T. Ono, Y. Sugimoto, Y. Masubuchi, S. Kikkawa, R. Kanno, M. Karppinen, and H. Yamauchi, "Electronic phase diagram of the layered cobalt oxide system  $\text{Li}_x\text{CoO}_2$  ( $0.0 \leq x \leq 1.0$ )," *Physical Review B*, vol. 80, no. 16, p. 165114, 2009.
- [44] K. Chang, B. Hallstedt, D. Music, J. Fischer, C. Ziebert, S. Ulrich, and H. J. Seifert, "Thermodynamic description of the layered  $\text{O}_3$  and  $\text{O}_2$  structural  $\text{LiCoO}_2$ - $\text{CoO}_2$  pseudo-binary systems," *Calphad*, vol. 41, pp. 6–15, 2013.
- [45] J. Reimers, J. Dahn, and U. Von Sacken, "Effects of impurities on the electrochemical properties of  $\text{LiCoO}_2$ ," *Journal of The Electrochemical Society*, vol. 140, no. 10, pp. 2752–2754, 1993.
- [46] G. Ceder and A. Van der Ven, "Phase diagrams of lithium transition metal oxides: investigations from first principles," *Electrochimica Acta*, vol. 45, no. 1, pp. 131–150, 1999.

- [47] R. Thirunakaran, N. Kalaiselvi, P. Periasamy, and N. Renganathan, "Mg substituted  $\text{LiCoO}_2$  for reversible lithium intercalation," *Ionics*, vol. 9, no. 5-6, pp. 388–394, 2003.
- [48] S. Gopukumar, C. Nithya, P. H. Maheshwari, R. Ravikumar, R. Thirunakaran, A. Sivashanmugam, S. K. Dhawan, and R. B. Mathur, "Solar powered lithium-ion battery incorporating high performing electrode materials," *RSC Adv.*, vol. 2, pp. 11574–11577, 2012.
- [49] J. N. Reimers and J. Dahn, "Electrochemical and in situ x-ray diffraction studies of lithium intercalation in  $\text{Li}_x\text{CoO}_2$ ," *Journal of the Electrochemical Society*, vol. 139, no. 8, pp. 2091–2097, 1992.
- [50] M. e. a. Ménétrier, "The insulator-metal transition upon lithium deintercalation from  $\text{LiCoO}_2$ : electronic properties and  $\text{Li}$  NMR study," *J. Mater. Chem.*, vol. 9, pp. 1135–1140, 1999.
- [51] S. Venkatraman and A. Manthiram, "Synthesis and characterization of  $\text{p}3$ -type  $\text{CoO}_{2-\delta}$ ," *Chemistry of materials*, vol. 14, no. 9, pp. 3907–3912, 2002.
- [52] L. Montoro, M. Abbate, and J. Rosolen, "Changes in the electronic structure of chemically deintercalated  $\text{LiCoO}_2$ ," *Electrochemical and Solid-State Letters*, vol. 3, no. 9, pp. 410–412, 2000.
- [53] C. A. Marianetti, G. Kotliar, and G. Ceder, "A first-order Mott transition in  $\text{Li}_x\text{CoO}_2$ ," *Nat. Mater.*, vol. 3, pp. 627–31, 2004.
- [54] M. Grundmann, *The Physics of Semiconductors: An Introduction Including Nanophysics and Applications*. Graduate Texts in Physics, Springer Berlin Heidelberg, 2010.
- [55] M. Balkanski and R. Wallis, *Semiconductor Physics and Applications*. Semiconductor Physics and Applications, OUP Oxford, 2000.

- [56] E. Schubert, *Doping in III-V Semiconductors*. E. Fred Schubert, 2015.
- [57] G. M. Ehrlich, *Lithium-ion batteries*. McGraw Hill Books New York, 2002.
- [58] J. Dahn, E. Fuller, M. Obrovac, and U. Von Sacken, “Thermal stability of  $\text{Li}_x\text{CoO}_2$ ,  $\text{Li}_x\text{NiO}_2$  and  $\lambda\text{-MnO}_2$  and consequences for the safety of li-ion cells,” *Solid State Ionics*, vol. 69, no. 3, pp. 265–270, 1994.
- [59] A. Veluchamy, C.-H. Doh, D.-H. Kim, J.-H. Lee, H.-M. Shin, B.-S. Jin, H.-S. Kim, and S.-I. Moon, “Thermal analysis of  $\text{LiCoO}_2$  cathode material of lithium ion battery,” *Journal of Power Sources*, vol. 189, no. 1, pp. 855 – 858, 2009. Selected Papers presented at the 14th {INTERNATIONAL} {MEETING} {ON} {LITHIUM} {BATTERIES} (IMLB-2008).
- [60] J. Spotnitz, R.; Franklin, “Abuse behavior of high-power, lithium-ion cells,” *J. Power Sources*, vol. 113, pp. –, 2003.
- [61] S. Al Hallaj, H. Maleki, J.-S. Hong, and J. R. Selman, “Thermal modeling and design considerations of lithium-ion batteries,” *Journal of power sources*, vol. 83, no. 1, pp. 1–8, 1999.
- [62] D. Ma, Z. Cao, and A. Hu, “Si-based anode materials for li-ion batteries: A mini review,” *Nano-Micro Letters*, vol. 6, no. 4, pp. 347–358, 2014.
- [63] C.-M. Park, J.-H. Kim, H. Kim, and H.-J. Sohn, “Li-alloy based anode materials for li secondary batteries,” *Chem. Soc. Rev.*, vol. 39, pp. 3115–3141, 2010.
- [64] D. Kevorkov, R. Schmid-Fetzer, and F. Zhang, “Phase equilibria and thermodynamics of the mg-si-li system and remodeling of the mg-si system,” *Journal of phase equilibria and diffusion*, vol. 25, no. 2, pp. 140–151, 2004.

- [65] R. Ma, Y. Liu, Y. Yang, M. Gao, and H. Pan, "Mg<sub>2</sub>Si anode for Li-ion batteries: Linking structural change to fast capacity fading," *Applied Physics Letters*, vol. 105, no. 21, p. 213901, 2014.
- [66] H. Liu, C. Hu, and S. Wu, "Ab initio study on the lithiation mechanism of Mg<sub>2</sub>Si electrode," in *Materials for Renewable Energy & Environment (ICMREE), 2011 International Conference on*, vol. 1, pp. 683–685, IEEE, 2011.
- [67] Y. Imai and A. Watanabe, "Energetics of compounds related to Mg<sub>2</sub>Si as an anode material for lithium-ion batteries using first principle calculations," *Journal of Alloys and Compounds*, vol. 509, no. 30, pp. 7877–7880, 2011.
- [68] N. Nitta, F. Wu, J. T. Lee, and G. Yushin, "Li-ion battery materials: present and future," *Materials Today*, vol. 18, no. 5, pp. 252–264, 2015.
- [69] J. B. Goodenough and K.-S. Park, "The Li-ion rechargeable battery: a perspective," *Journal of the American Chemical Society*, vol. 135, no. 4, pp. 1167–1176, 2013.
- [70] L. Kanevskii and V. Dubasova, "Degradation of lithium-ion batteries and how to fight it: A review," *Russian Journal of Electrochemistry*, vol. 41, no. 1, pp. 1–16, 2005.
- [71] L. Yang, T. Markmaitree, and B. L. Lucht, "Inorganic additives for passivation of high voltage cathode materials," *Journal of Power Sources*, vol. 196, no. 4, pp. 2251–2254, 2011.
- [72] I. of Geophysics and U. Planetary Physics Orson Anderson Professor of Geophysics, *Equations of State for Solids in Geophysics and Ceramic Science*. Oxford University Press, USA, 1994.
- [73] J. Poirier, *Introduction to the Physics of the Earth's Interior*. Cambridge University Press, 2000.

- [74] I. Torrens, *Interatomic Potentials*. Elsevier Science, 2012.
- [75] J. Kohanoff, *Electronic Structure Calculations for Solids and Molecules: Theory and Computational Methods*. Cambridge University Press, 2006.
- [76] P. J. Hasnip, K. Refson, M. I. Probert, J. R. Yates, S. J. Clark, and C. J. Pickard, “Density functional theory in the solid state,” *Philosophical Transactions of the Royal Society of London A: Mathematical, Physical and Engineering Sciences*, vol. 372, no. 2011, p. 20130270, 2014.
- [77] A. Montorsi, *The Hubbard Model: A Reprint Volume*. World Scientific, 1992.
- [78] J. Thijssen, *Computational Physics*. Cambridge University Press, 2007.
- [79] P. E. Blöchl, “Projector augmented-wave method,” *Physical Review B*, vol. 50, no. 24, p. 17953, 1994.
- [80] P. Blöchl, J. Kästner, and C. Först, “Electronic structure methods: Augmented waves, pseudopotentials and the projector augmented wave method,” in *Handbook of Materials Modeling* (S. Yip, ed.), pp. 93–119, Springer Netherlands, 2005.
- [81] J. P. Perdew, K. Burke, and M. Ernzerhof, “Generalized gradient approximation made simple,” *Physical review letters*, vol. 77, no. 18, p. 3865, 1996.
- [82] S. Dudarev, G. Botton, S. Savrasov, C. Humphreys, and A. Sutton, “Electron-energy-loss spectra and the structural stability of nickel oxide: An lsd+ u study,” *Physical Review B*, vol. 57, no. 3, p. 1505, 1998.
- [83] A. Juhin, F. De Groot, G. Vankó, M. Calandra, and C. Brouder, “Angular dependence of core hole screening in licoo 2: A dft+ u calculation

- of the oxygen and cobalt k-edge x-ray absorption spectra,” *Physical Review B*, vol. 81, no. 11, p. 115115, 2010.
- [84] A. Jain, S. P. Ong, G. Hautier, W. Chen, W. D. Richards, S. Dacek, S. Cholia, D. Gunter, D. Skinner, G. Ceder, and K. a. Persson, “The Materials Project: A materials genome approach to accelerating materials innovation,” *APL Materials*, vol. 1, no. 1, p. 011002, 2013.
- [85] A. Jain, G. Hautier, S. P. Ong, C. J. Moore, C. C. Fischer, K. A. Persson, and G. Ceder, “Formation enthalpies by mixing gga and gga+u calculations,” *Phys. Rev. B: Condens. Matter Mater. Phys.*, vol. 84, no. 4, p. 045115, 2011.
- [86] M. Wang, “Enthalpy of formation of linio<sub>2</sub>, licoo<sub>2</sub> and their solid solution, lini<sub>1-x</sub>coxo<sub>2</sub>,” *Solid State Ionics*, vol. 166, pp. 167–173, 2004.
- [87] G. Gottstein, *Physikalische Grundlagen der Materialkunde*. Springer-Lehrbuch, Springer Berlin Heidelberg, 2013.
- [88] M. Aykol and C. Wolverton, “Local environment dependent gga+u method for accurate thermochemistry of transition metal compounds,” *Physical Review B*, vol. 90, no. 11, p. 115105, 2014.
- [89] A. F. G. K. J. Aydinol, M. K.; Kohan, “Ab initio study of lithium intercalation in metal oxides and metal dichalcogenides,” *Phys. Rev. B: Condens. Matter Mater. Phys.*, vol. 56, pp. –, 1997.
- [90] S. Kristyán and P. Pulay, “Can (semi) local density functional theory account for the london dispersion forces?,” *Chemical physics letters*, vol. 229, no. 3, pp. 175–180, 1994.
- [91] A. Gupta, P. Agarwal, S. Bee, P. Tandon, and V. Gupta, “Heat capacity and vibrational dynamics of polyvinylidene fluoride ( $\beta$ -form),” *Polymer Science Series A*, vol. 53, no. 5, pp. 375–384, 2011.

- [92] C.-m. Yin, Z. Liu, G. Wang, and C. Wu, "Determination of heat capacity of explosives and related materials by dsc," in *Proc. Int. Pyrotech. Seminar 17th*, vol. 1, pp. 515–521, 1991.
- [93] B. Wu, Z. Li, and J. Zhang, "Thermal design for the pouch-type large-format lithium-ion batteries i. thermo-electrical modeling and origins of temperature non-uniformity," *Journal of The Electrochemical Society*, vol. 162, no. 1, pp. A181–A191, 2015.
- [94] N. Ponchaut, F. Colella, V. Somandepalli, and M. Stern, "Thermal management modeling for thermal runaway avoidance in lithium-ion batteries," 2014.
- [95] M. Winter, J. O. Besenhard, M. E. Spahr, and P. Novak, "Insertion electrode materials for rechargeable lithium batteries," *Advanced materials*, vol. 10, no. 10, pp. 725–763, 1998.
- [96] S. Bourderau, T. Brousse, and D. Schleich, "Amorphous silicon as a possible anode material for li-ion batteries," *Journal of power sources*, vol. 81, pp. 233–236, 1999.
- [97] D. Wang, X. Wu, Z. Wang, and L. Chen, "Cracking causing cyclic instability of lifepo 4 cathode material," *Journal of Power Sources*, vol. 140, no. 1, pp. 125–128, 2005.
- [98] T. Maxisch and G. Ceder, "Elastic properties of olivine  $\text{Li}_x\text{FePO}_4$  from first principles," *Physical Review B*, vol. 73, no. 17, p. 174112, 2006.
- [99] J. Christensen and J. Newman, "A mathematical model of stress generation and fracture in lithium manganese oxide," *Journal of The Electrochemical Society*, vol. 153, no. 6, pp. A1019–A1030, 2006.
- [100] X. Zhang, W. Shyy, and A. M. Sastry, "Numerical simulation of intercalation-induced stress in li-ion battery electrode particles," *Jour-*

- nal of the Electrochemical Society*, vol. 154, no. 10, pp. A910–A916, 2007.
- [101] M. Ebner, F. Marone, M. Stampanoni, and V. Wood, “Visualization and quantification of electrochemical and mechanical degradation in li ion batteries,” *Science*, vol. 342, no. 6159, pp. 716–720, 2013.
- [102] R. Hausbrand, G. Cherkashinin, H. Ehrenberg, M. Gröting, K. Albe, C. Hess, and W. Jaegermann, “Fundamental degradation mechanisms of layered oxide li-ion battery cathode materials: Methodology, insights and novel approaches,” *Materials Science and Engineering: B*, vol. 192, pp. 3–25, 2015.
- [103] H. Kim, J. Choi, H.-J. Sohn, and T. Kang, “The insertion mechanism of lithium into mg<sub>2</sub>si anode material for li-ion batteries,” *Journal of the Electrochemical Society*, vol. 146, no. 12, pp. 4401–4405, 1999.
- [104] A. Togo, *phonopy manual*, 2014.
- [105] A. Togo and I. Tanaka, “First principles phonon calculations in materials science,” *Scr. Mater.*, vol. 108, pp. 1–5, Nov 2015.
- [106] A. Van de Walle, M. Asta, and G. Ceder, “The alloy theoretic automated toolkit: A user guide,” *Calphad*, vol. 26, no. 4, pp. 539–553, 2002.



# List of Tables

4.1	The calculated lattice parameters for different stoichiometries of $\text{Li}_x\text{CoO}_2$ and experimental lattice parameters by Takahashi et al. [22] and Hertz et al. [30] . . . . .	77
4.2	Coefficients for the heat capacity polynomials . . . . .	88
B1.1	Data on the derivation of $C_p$ for $\text{Li}_{0.5}\text{CoO}_2$ based on specified weight ratio of $\text{Li}_{0.5}\text{CoO}_2$ , PVDF and graphite of Ito et al. [31].	130



# List of Figures

1.1	Ragone plot of different battery chemistries comparing specific power and specific energy [1] . . . . .	2
1.2	Schematics of a typical LIB with intercalation hosts as anode and cathode . . . . .	7
1.3	The process of SEI formation: lithium-alkyl carbonates form the SEI, eventually the formed SEI layer prevents further growth.	9
1.4	The different layered polytypes of $\text{LiCoO}_2$ : starting from the left O2-, O3-, O4- and O6- $\text{LiCoO}_2$ . . . . .	11
1.5	In-plane vacancy ordering at a lithium-concentration of $x=0.5$	13
1.6	Lattice parameters in dependence of lithium content at room temperature (a),(b) and (c) as well as phase diagram by Reimer et al. in dependence of lithium content in the O3- $\text{LiCoO}_2$ (d) .	14
1.7	The phase diagram of $\text{LiCoO}_2$ at 298 K in different thermodynamic assessments as compiled in [44] . . . . .	15
1.8	The voltage profile of O3- $\text{Li}_x\text{CoO}_2$ vs lithium with the plateau in the metal-to-insulator 2-phase region: the charging starts from $x=1$ until reaching a voltage of 4.5 V, subsequently the discharge curve is displayed up to $x=0.88$ . . . . .	16

1.9	The electronic DOS of $\text{Li}_x\text{CoO}_2$ taken from Venkatraman and Manthiram [51]: overlap of the O-2p and the Co-3d orbitals leads to the oxidation of oxygen at deep lithium extraction close to $x=0.5$ prompting the formation of oxygen. This imposes a limit to the reversible capacity of $\text{Li}_x\text{CoO}_2$ . . . . .	17
1.10	The Li-Mg-Si phase diagram at $200^\circ\text{C}$ with the solid solution phase $\text{Li}_x\text{Mg}_2\text{Si}$ , (Mg) and $\tau_2$ constituting the 3 phase field, adapted from [64]. . . . .	20
1.11	The crystal structure of $\text{Li}_x\text{Mg}_2\text{Si}$ : this compound has a cubic unit cell and crystallizes in space group F-3m (225). The crystal structure data is taken from Imai et al. [67] . . . . .	21
1.12	Illustration of the operational voltage window of a LIB in an energy diagram [69]. . . . .	22
2.1	An anharmonic potential is shown with the tie lines representing energy levels corresponding to excitations due to elevated temperatures. The red dotted line indicates the shift of the average position of the atom in dependence of the successively increasing excitation and provides a conceptional description of thermal expansion. . . . .	33
3.1	The Self-consistent-field method . . . . .	43
3.2	Effect of the Hubbard U parameter on the electron behaviour: a low U value decreases the Coulomb repulsion between electrons in the same orbital. Consequently, the electrons can delocalize, which resembles a metallic behaviour. A high U value has the opposite effect. . . . .	47
3.3	Schematic representation of the energy cutoff in the reciprocal lattice . . . . .	48
3.4	Illustration of the pseudopotential and the pseudo-electron wave function . . . . .	49

3.5	Some possible clusters on a 2-dimensional square lattice . . . .	59
3.6	Binary alloy representation in the Cluster expansion formalism	59
4.1	Electronic density of states in dependence of U-value obtained from spin-polarized calculations: band gaps range from 2.1 eV for U=3.3 eV to 3.2 eV for U=7 eV. . . . .	68
4.2	Electronic DOS in dependence of lithium content: tail states on top of the valence band and at the bottom of the conduction band can be observed when lithium is removed. The tail states merge below x=0.777 leading to the metallic phase. . . . .	69
4.3	Calculated band gaps plotted in dependence of lithium content and comparison to experimental data: computed and experimental data at x=1 show good agreement. . . . .	70
4.4	c lattice parameter in dependence of lithium content in $\text{Li}_x\text{CoO}_2$ : comparison with experimental data of Ménétrier et al. [50] and Takahashi et al. [22] reveals good overall agreement. . . . .	71
4.5	Enthalpies of formation versus the constituting elements for metallic and insulating states vs lithium content: good agreement in comparison to Wang and Navrotsky [86]. It is clearly observable that the semiconducting phase is more stable at high lithium contents. At x=0.5 it is not possible any more to converge to a semiconducting phase. . . . .	72
4.6	Computed average intercalation voltage of $\text{Li}_x\text{CoO}_2$ compared to ab initio result of Aydinol et al. [89] and experimental voltage profile of Ozhuku et al. [16] . . . . .	74
4.7	Phonon DOS of $\text{LiCoO}_2$ calculated by the linear response method with 3 different parameters: GGA-PBE accounting for Born-charge, GGA-PBE without Born-charge and GGA+U accounting for Born charge. Phonon frequencies $\nu > 0$ indicate that calculations are well converged and structures are stable.	78

- 4.8 Demonstration of Born charge effects on the heat capacity of the pristine  $\text{LiCoO}_2$ : no significant impact on the resulting heat capacities can be observed. The inset displays the basic mechanism behind the Born effective charges, which are induced in the limit of long wave lengths of longitudinal modes. Dipoles induce an additional contribution  $\vec{p}$  to the restoring force. . . . . 79
- 4.9 The impact of a Hubbard  $U$  value of 3.3 eV on the isobaric heat capacity of  $\text{LiCoO}_2$ : the results show only negligible effects. 80
- 4.10 Phonon DOS of  $\text{LiCoO}_2$ ,  $\text{Li}_{0.67}\text{CoO}_2$  and  $\text{Li}_{0.5}\text{CoO}_2$  calculated by the finite difference method.  $\nu > 0$  indicates stable structures. 81
- 4.11 Bulk modulus and thermal expansion coefficient: obtained from the EOS fit on  $\text{LiCoO}_2$  and used to compute  $C_p$  by utilizing equation 3.24. . . . . 81
- 4.12 Quasi-harmonic fit of  $\text{LiCoO}_2$  over a series of volumes using the Birch-Murnaghan-EOS. The red line interconnects the minima at each temperature respectively, highlighting the thermal expansion. . . . . 82
- 4.13 Gibbs free energy of the pristine  $\text{LiCoO}_2$  obtained by Legendre-transformation of the Helmholtz free energy . . . . . 83
- 4.14 Calculated heat capacities at constant pressure for  $\text{LiCoO}_2$ ,  $\text{Li}_{0.67}\text{CoO}_2$  and  $\text{Li}_{0.67}\text{CoO}_2$  compared to available literature data. 84
- 4.15 Heat capacity of  $\text{Li}_{0.5}\text{CoO}_2$  by Ito et al. with correction by accounting for the heat capacities of PVDF [91] and graphite [92] impurities in the sample. . . . . 85
- 4.16 Influence of boron-doping on heat capacity: substitution of cobalt with boron leads to a decrease of the isobaric heat capacity as a result of the smaller weight of boron. . . . . 87

4.17	CALPHAD-type fitting curves (red lines) from 250 K to 600 K by employing the empirical polynomial of equation 4.9 on $\text{LiCoO}_2$ , $\text{Li}_{0.67}\text{CoO}_2$ , $\text{Li}_{0.5}\text{CoO}_2$ and $\text{LiCo}_{11/12}\text{B}_{1/12}\text{O}_2$ . . . . .	89
4.18	Cluster expansion of $\text{Li}_x\text{Mg}_2\text{Si}$ . . . . .	90
4.19	Non-isotropic relaxation of calculated structure on $\text{Li}_x\text{Mg}_2\text{Si}$ . As can be observed the relaxations at lower vacancy concentrations the relaxations increase significantly due to lattice distortions upon lithium intake. . . . .	91
4.20	ECIs obtained from the cluster expansion: no clear decay can be observed with growing size of the clusters from pairs to triplets to quadruplets. . . . .	92
4.21	Predicted energies by the LOOCV method plotted versus the calculated energies show good agreement. . . . .	93
4.22	The calculated average intercalation voltage of $\text{Li}_x\text{Mg}_2\text{Si}$ compared to the first electrochemical cycle of an experiment by Kim et al. [103] . . . . .	93
A2.1	Atom on an energy surface with a local minimum, starting position is at coordinate R if structure is not properly relaxed, generating a displaced structure leads to coordinate $R+\Delta$ u which is closer to the local minimum, resultant force constant is negative . . . . .	125
A2.2	The iterative process of the quasi-harmonic approximation, computational time was mainly consumed for the calculation of the frequency spectrum (2nd step) . . . . .	127
B1.3	The two vacancy arrangements of $\text{Li}_{0.5}\text{CoO}_2$ (O3-polytype) used for the calculation of $C_p$ within the QHA: P12/m1 (left, unstable) and P2/c (right, stable). . . . .	130
B1.4	Bulk modulus and thermal expansion for $\text{Li}_{0.67}\text{CoO}_2$ , $\text{Li}_{0.5}\text{CoO}_2$ and $\text{LiCo}_{0.917}\text{B}_{0.083}\text{O}_2$ derived from EOS-fit. . . . .	131
B1.5	Gibbs energy for $\text{Li}_{0.67}\text{CoO}_2$ , $\text{Li}_{0.5}\text{CoO}_2$ and $\text{LiCo}_{0.917}\text{B}_{0.083}\text{O}_2$ . . . . .	132

B2.6 LiMg<sub>2</sub>Si in the primitive unit cell as supplied as parent lattice  
for ATAT. . . . . 133

# Thank you

At the front line I would like to thank my advisor Professor Lorenz Singheiser who gave me the possibility to do my PhD at the institute IEK-2 of Forschungszentrum Jülich. In this respect I also want to express my gratitude for granting the research stay at the Materials Science and Engineering (MSE) department of UC Berkeley, California in order to deepen my methodological skills specific to the PhD research. At this point I want to thank Professor Mark Asta for hosting my stay at his research group and his scientific directions as well as Isaac Marcus for the discussions and advice he provided helping me to improve my scientific understanding. Beyond that, I am grateful for the access to the compute cluster Fenrir of the Asta research group, with which I was able to bridge the down time of the Jülich compute clusters JUROPA and JURECA, particularly during the retrofit period. Moreover, I thank the support team from the Jülich Supercomputing centre for providing IT-support to my work. In particular, I would like to acknowledge Dr. Florian Janetzko and Viorel Chihaia for helping me with any issues related to the compilation and usage of VASP on the supercomputing cluster.

Also, I owe Theodoros Stylianos Kondylis a big thank you for his expertise on Linux based operating systems and his efforts on recovering the data on the work station's defective hard drive. Additionally, I would like to extend my thanks to the non-scientific staff of the institute for their services.

Many thanks also to Professor Robert Spatschek who started just in time as our group leader to provide scientific feedback on my work before I crossed

the finish line. Of course, I want to say thank you to Nathan Lemahieu for introducing me to  $\text{\LaTeX}$  and his persistent attempts in drawing away my attention from work. Then there are, most certainly, the colleagues of my group who were all nice and supportive throughout the whole time. Thank you to Aurélie Jacob for "les crêpes et gateaux à la maison".

Lastly, I want to deeply thank my boyfriend Stefan, my mom, my dad and my sister who altogether kept their faith in me with respect to finishing my PhD.

# Appendices

## A A short guide to running the codes

### A1 The VASP input files

In VASP four input files have to be specified: INCAR, POTCAR, POSCAR and KPOINTS. INCAR contains specific information about the calculation details, i.e. whether a full structure relaxation or a constrained structure relaxation has to be performed, whether symmetry of the crystal is to be exploited to reduce the computational demand or whether electron spins should be accounted for to calculate the magnetic properties. Additionally it is possible to specify the desired accuracy which is influenced by various factors. Among these are the convergence criteria, the energy cutoff for the plane-waves and the smearing method for integrating the electron occupation function. The POTCAR file contains the atomic PAW-potentials acting on the electrons for the constituent atomic species. At the same time it provides the necessary information to construct the electron density and to derive the total energy. The POSCAR file specifies the crystal structure and atomic positions whereas the KPOINTS file is necessary to define the k-mesh for the integration in reciprocal space.

## A2 The Phonopy code

The Phonopy code is a post-processing tool on top of ab initio codes as VASP or Quantum Espresso. [104, 105] It is written to read specific data from the output of the ab initio code when calculating lattice dynamical (phonon) properties. The actual computationally demanding part lies with the ab initio calculations to obtain atomic forces on structures which are displaced from equilibrium or to directly calculate the force constants. Once this data is obtained Phonopy can be used to extract the relevant data from the `vasprun.xml` output file and process it to yield the phonon DOS, band structure and calculate the phonon harmonic free energy as well as fit a specified EOS within the framework of the QHA.

Phonopy works hand in hand with VASP. The calculation of phonon properties requires the structures to be fully relaxed to equilibrium and uses a specified supercell of the fully relaxed geometry as input to generate supercells of structures with symmetry-distinct atomic displacements and the supercell of the pristine structure. So going from here, there are two ways of proceeding with VASP/Phonopy:

- Finite-differences method

The supercells with symmetry-distinct displacements are supplied as input for the ab initio code to calculate the atomic forces as a response to those displacements. After successful termination of the calculations the `vasprun.xml` files contain the atomic response forces of each of the atoms in the supercells. These are then evaluated together with the atomic displacement vectors according to equation 3.15 yielding the atomic force constants.

- Linear response method

In the currently available version (VASP 5.3) the linear response algorithm is only implemented as  $\Gamma$  (Gamma) point calculation. This means that it also requires supercells to obtain converged results (otherwise

the k-points grid is too loose) The supercell of the pristine structure is supplied to the ab initio code and the force constants are directly calculated within linear response theory (equation 3.16) as readily implemented in VASP.

To ensure a clean calculation it is necessary to check that the structures have converged within strict convergence criteria. If the structures have not reached the global minimum yet, force constants are obtained as negative values as illustrated in figure A2.1. If the force constants are negative the

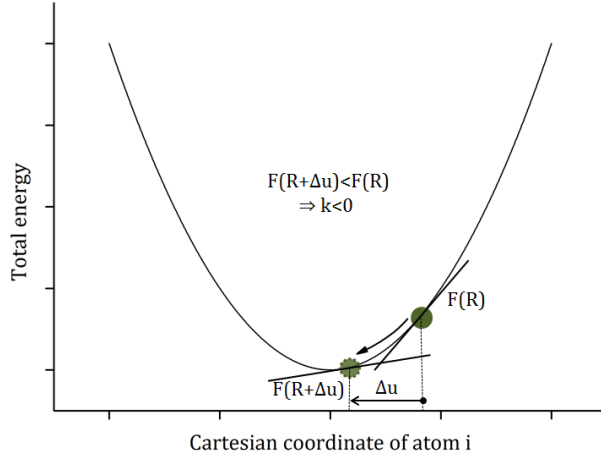


Figure A2.1: Atom on an energy surface with a local minimum, starting position is at coordinate  $R$  if structure is not properly relaxed, generating a displaced structure leads to coordinate  $R+\Delta u$  which is closer to the local minimum, resultant force constant is negative

eigenfrequencies have the form of an imaginary number (equation 2.16), but are displayed as negative numbers in the graphical output. Since the thermal properties are derived from the phonon DOS the existence of imaginary frequencies in the phonon DOS can influence the calculated properties significantly especially if these specific frequencies have a relatively high DOS.

This is due to the fact that imaginary frequencies are not taken into account for the calculation of the thermal properties. Consequently, residual imaginary frequencies with rather large contributions to the phonon DOS should be avoided and hence the structure at hand needs to be relaxed again by modulating along the k-vectors of the respective frequencies (see subsection A2).

To extract the frequency spectrum for constant volume calculations the commands 'phonopy -t' and 'phonopy -p' were issued. To obtain the quasi-harmonic results after iterating over the constant volumes the command 'phonopy-qha' includes the thermal properties of the volumes specified by the user. The whole iteration sequence is shown in figure A2.2. Usually the inclusion of 4 to 6 volumes are sufficient for an adequate fit.

### **Modulating along k-vectors of imaginary modes**

If imaginary frequencies are obtained from the calculation of the frequency spectrum the structure at hand may still not be residing in its most stable geometry. This can either signify that the full structure relaxation was not sufficient in order to reach the global minimum (this can happen if the compound exhibits a complex energy surface complicating convergence) or it may indicate that the structure is metastable and that another crystal structure is thermodynamically more stable. In any case, having large contributions of the imaginary frequencies in relation to the phonon DOS is detrimental for the reliability of the data since the phonon free energy and its derived properties like the heat capacity can only be calculated from the normal modes (positive frequencies). Because the imaginary frequencies imply that the total energy is decreasing along the vibrational direction artificially moving the respective atoms/ions in that direction should help to relax to the global minimum. The vibrational direction is the direction of the amplitude vector or the k-vector of the frequency. Using the code phonopy this process is called modulation and can be done by specifying the k-vector along which to

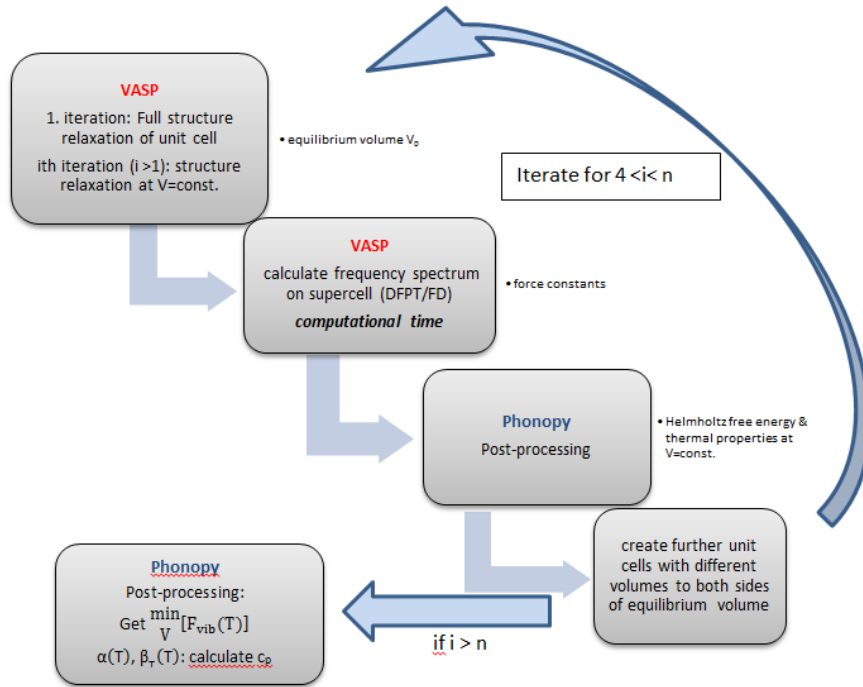


Figure A2.2: The iterative process of the quasi-harmonic approximation, computational time was mainly consumed for the calculation of the frequency spectrum (2nd step)

modulate the structure. The respective input file is 'band.conf' with which one can plot the band structure to see which k-vectors are related to the imaginary frequencies.

### A3 ATAT

ATAT is a code written by Axel van de Walle and consists essentially of a Cluster expansion code and a Monte Carlo code [106]. It is designed to derive phase diagrams purely from ab initio. ATAT can interface with a list

of different DFT codes such as VASP, Exciting and Quantum Espresso. The main part of the Cluster expansion code is the "maps"-executable. Running this executable will start a process, during which the program looks for any calculated structures matching the parameters of the parent lattice (lat.in) and attempts to expand the energy in a series of terms in the fashion of equation 3.26.

### The input files for the cluster expansion

The cluster expansion code needs two input file: lat.in and vasp.wrap. In lat.in the crystal structure on which the cluster expansion is to be carried out is specified and should be provided by the user in the setting of the primitive unit cell. This is due to the fact that supercells are generated with respect to the specified cell. So if the conventional cell is provided then there is a chance that some intermediately large supercells are missed and are not included to construct the cluster expansion. The lat.in file has the following format:

```
a b c  $\alpha$   $\beta$   $\gamma$ 
1 0 0
0 1 0
0 0 1
 $x_0$   $y_0$   $z_0$  A,B
...
 $x_i$   $y_i$   $z_i$  C
```

The first line defines the lattice parameters and the angles. The second to the fourth line specify the supercell of the unit cell and can usually be taken as in the example. The remaining lines describe the atom positions in fractional coordinates whereas at the end of the lines the atoms are specified. If the site at hand can host more than one atom type then they are separated by a comma.

In `vasp.wrap` the settings for the DFT calculations are defined. Once these files are provided the code can be initialized. Structures are generated of which the total energies are to be calculated with the DFT code. After having calculated a certain number of structures there is enough information for the code to attempt a fit with equation 3.26 and will continuously print out the quality of the fit as the calculations advance. Successively the code is able to systematically predict new ground state structures to be calculated which improve the fit.

### **The Cross-validation-score**

In the cluster expansion code of ATAT the measure of quality of the fit is the cross-validation-score as explained in section 3.8.3. It is designed such that it estimates the error made by the predicted energy of structures  $i$  when using the  $i-1$  other energies.  $E_i$  is the calculated energy of structure  $i$  whereas  $\hat{E}_i$  is the energy of structure  $i$  as predicted from the other  $i-1$  structures. During the process of the cluster expansion when successively providing increasingly more energies as input the cross-validation score is being printed and updated in the `maps.log` file.

## B Supplementary data

### B1 Heat capacities within the QHA

Table B1.1: Data on the derivation of  $C_p$  for  $\text{Li}_{0.5}\text{CoO}_2$  based on specified weight ratio of  $\text{Li}_{0.5}\text{CoO}_2$ , PVDF and graphite of Ito et al. [31].

compound	mass ratio	mol ratio	$C_p$ [J/K mol] at 298 K
PVDF	3.5	0.0366	58 [91]
graphite	5	0.279	8.23 [92]
$\text{Li}_{0.5}\text{CoO}_2$	100	0.6844	70.98

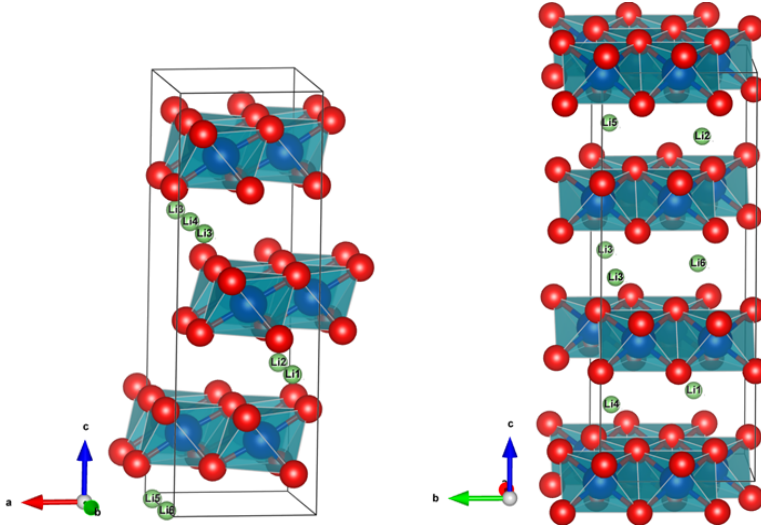


Figure B1.3: The two vacancy arrangements of  $\text{Li}_{0.5}\text{CoO}_2$  (O3-polytype) used for the calculation of  $C_p$  within the QHA: P12/m1 (left, unstable) and P2/c (right, stable).

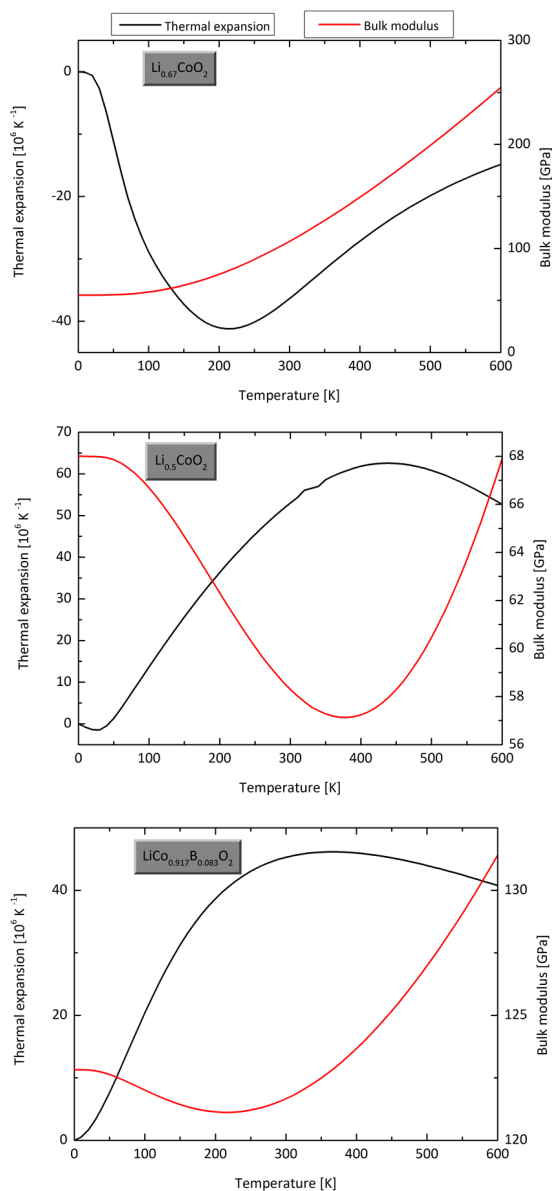


Figure B1.4: Bulk modulus and thermal expansion for  $\text{Li}_{0.67}\text{CoO}_2$ ,  $\text{Li}_{0.5}\text{CoO}_2$  and  $\text{LiCo}_{0.917}\text{B}_{0.083}\text{O}_2$  derived from EOS-fit.

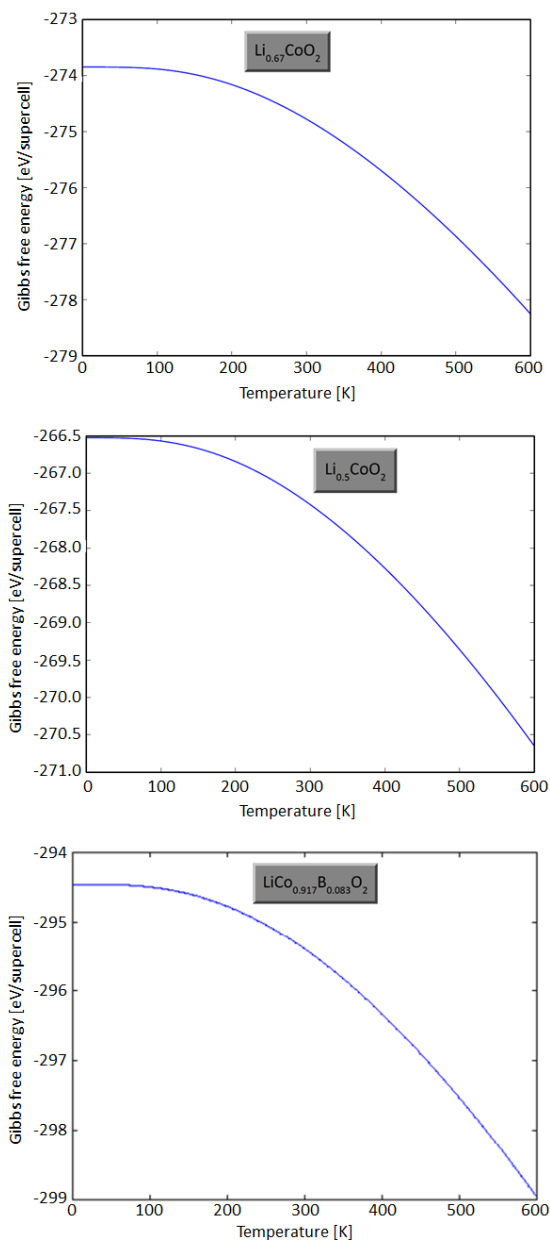


Figure B1.5: Gibbs energy for  $\text{Li}_{0.67}\text{CoO}_2$ ,  $\text{Li}_{0.5}\text{CoO}_2$  and  $\text{LiCo}_{0.917}\text{B}_{0.083}\text{O}_2$ .

## B2 The cluster expansion of $\text{Li}_x\text{Mg}_2\text{Si}$

The format of the lat.in file for the compound in the primitive setting:

```
4.617 4.6171 4.617 60 60 60
1 0 0
0 1 0
0 0 1
0.250000000 0.250000000 0.250000000 Mg
0.750000000 0.750000000 0.750000000 Mg
0.000000000 0.000000000 0.000000000 Si
0.500000000 0.500000000 0.500000000 Li,Vac
```

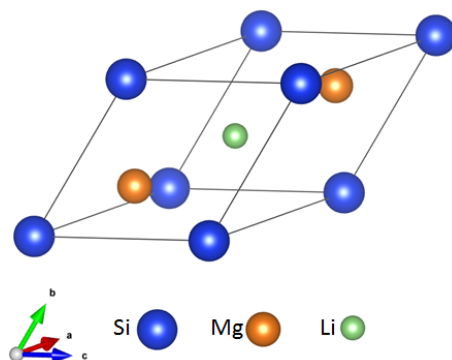


Figure B2.6:  $\text{LiMg}_2\text{Si}$  in the primitive unit cell as supplied as parent lattice for ATAT.



Band / Volume 307

**Development and Application of a Multiscale Model  
for the magnetic Fusion Edge Plasma Region**

F. Hasenbeck (2016), 190 pp

ISBN: 978-3-95806-120-0

Band / Volume 308

**Emissions of Biogenic Volatile Organic Compounds and  
Ozone Balance under Future Climate Conditions**

C. Wu (2016), VI, 105 pp

ISBN: 978-3-95806-121-7

Band / Volume 309

**Computerunterstützte Auslegung eines Brennstoffzellen-Batterie-  
Hybridsystems für die Bordstromversorgung**

C. Krupp (2016), iii, 207 pp

ISBN: 978-3-95806-124-8

Band / Volume 310

**Influence of H<sub>2</sub>O, HCl and H<sub>2</sub>S on the Release and  
Condensation of Trace Metals in Gasification**

M. Benito Abascal (2016), XIX, 172 pp

ISBN: 978-3-95806-125-5

Band / Volume 311

**Mechanical and Thermochemical Properties of Nano-structured  
Membranes for Gas Separation in Fossil-fired Power Plants**

J. Zhang (2016), II, 134 pp

ISBN: 978-3-95806-126-2

Band / Volume 312

**Development of Embedded Thermocouple Sensors for Thermal  
Barrier Coatings (TBCs) by a Laser Cladding Process**

Y. Zhang (2016), II, 108 pp

ISBN: 978-3-95806-129-3

Band / Volume 313

**Streamwater transit time distributions at the catchment scale:  
constraining uncertainties through identification of spatio-temporal  
controls**

M. Stockinger (2016), XIX, 161 pp

ISBN: 978-3-95806-131-6

Band / Volume 314

**Entwicklung eines metallbasierten Substratkonzepts für energieeffiziente Gastrennmembranen**

J. A. Kot (2016), xi, 201 pp  
ISBN: 978-3-95806-134-7

Band / Volume 315

**Langzeitbeobachtung der Dosisbelastung der Bevölkerung in radioaktiv kontaminierten Gebieten Weißrusslands – Korma-Studie II (1998 – 2015)**

P. Zoriy, H. Dederichs, J. Pillath, B. Heuel-Fabianek, P. Hill, R. Lennartz (2016), ca 104 pp  
ISBN: 978-3-95806-137-8

Band / Volume 316

**Oxidation Mechanisms of Metallic Carrier Materials for Gas Separation Membranes**

M. Schiek (2016), 148 pp  
ISBN: 978-3-95806-138-5

Band / Volume 317

**Thermoschockverhalten und temperaturabhängige Eigenschaften kohlenstoffarmer und -freier Feuerfestwerkstoffe**

A. Böhm (2016), VI, 153 pp  
ISBN: 978-3-95806-139-2

Band / Volume 318

**Theoretical and experimental studies of runaway electrons in the TEXTOR tokamak**

S.S. Abdullaev, K.H. Finken, K. Wongrach, O. Willi (2016), X, 109 pp  
ISBN: 978-3-95806-140-8

Band / Volume 319

**Modelling Thermodynamic Properties of Intercalation Compounds for Lithium Ion Batteries**

S. O. Dang (2016), x, 133 pp  
ISBN: 978-3-95806-141-5

Weitere **Schriften des Verlags im Forschungszentrum Jülich** unter  
<http://www.zb1.fz-juelich.de/verlagextern1/index.asp>



**Energie & Umwelt /  
Energy & Environment  
Band / Volume 319  
ISBN 978-3-95806-141-5**

